Modeling and Fabrication of Piezoelectric Nanomaterial Devices for Sensing and Energy Harvesting

A DISSERTATION SUBMITTED TO THE FACULTY OF THE
UNIVERSITY OF MINNESOTA

BY

Kory Jenkins

IN PARTIAL FULFILLMENT OF THE REQUIREMENTS
FOR THE DEGREE OF
DOCTOR OF PHILOSOPHY

Prof. Rusen Yang, Prof. Jürgen Konczak

May 2018

Acknowledgement

I would like to express my deepest gratitude to my advisor, Prof. Rusen Yang, for his guidance and support throughout my graduate studies, and for introducing me to the exciting world of nanomaterials. He taught me how to approach and solve challenging problems, through his ever-present commitment to the success of his students. Although I still have much to learn, Prof. Yang has given me the tools to pursue this knowledge, wherever it may lead.

I also extend my great appreciation to my co-advisors, Prof. Jürgen Konczak and Prof. Martha Flanders. Their support has enabled me to explore rewarding and meaningful work in haptics and prosthetics. I am grateful to my committee members, Prof. Victor Barocas and Prof. Rajesh Rajamani, for graciously welcoming me into their wonderful lab groups during my research rotations. Their advice has been invaluable to this work.

Many thanks must be given to my fellow NSTL lab members, especially Dr. Vu Nguyen, Dr. Ren Zhu, and Wengui Zhang. Their mentoring, collaboration, and friendship have been invaluable. I also want to thank NSTL undergraduate members Kayla Bohlke, Steve Kelly, Alex Jurcoi, Brandon Maas, and Kenny Ostyn Harsono for their many contributions and collaboration. I am grateful for my collaborations with visiting scholars Dr. Huimin Hao, Dr. Haiwu Zheng, Dr. Xiaowen Huang, and Dr. Jianlin Chen.

I sincerely thank the faculty, staff, and students in the Mechanical Engineering department for their support and collaboration. I also thank the NSF IGERT fellowship program faculty, staff, and students, in particular director Prof. Bin He and program coordinator Rachel Jorgenson. The IGERT program has broadened my horizons and given me a sense of community that I will always treasure. This work could not have been completed without support from faculty and staff in the Minnesota Nano Center, the U of M Characterization Facility, and the Minnesota Supercomputing Institute.

Last, but certainly not least, thank you to my amazing wife Alyssa, for her constant support, encouragement, and love over the last five years. And thank you to my family for their love and encouragement.

Dedication

To

My wife, Alyssa

My mother, Maureen, My father, Mark, and my brother, Kyle

Abstract

Piezoelectric nanomaterials are the basis for many devices including nanogenerators, force sensors, and strain sensors. Barriers to the continued development of these devices include a limited understanding of piezoelectric behavior in emerging nanomaterials, and the limitations of nanomaterial fabrication techniques. This thesis explores emerging piezoelectric nanomaterial behavior through finite element modeling, expands a nanomaterial fabrication technique to new substrates, and demonstrates new piezoelectric nanomaterial devices enabled by these findings.

Diphenylalanine (FF) peptide is an emerging bio-inspired piezoelectric material with remarkable electromechanical properties. First principles analysis and finite element models have explored the mechanical properties of FF peptide. However, limited information is available to predict the piezoelectric performance of FF peptide compared to conventional piezoelectric nanomaterials. Device fabrication is high risk, requiring significant investments in infrastructure, funding, and time. Therefore, finite element models of piezoelectric potential are needed to inform the design of devices based on FF peptide and other piezoelectric nanomaterials.

In addition to piezoelectricity, nanomaterials such as zinc oxide (ZnO) may have semiconducting properties, making them suitable for highly sensitive devices enabled by the piezotronic effect. Chemical vapor deposition (CVD) can produce ultra-long nanowires, but the high-temperature process is incompatible with flexible polymers and other low-temperature substrates, limiting device design. Synthesis of emerging 2D piezoelectric nanomaterials such as molybdenum disulfide (MoS_2) can also benefit from low-temperature substrates. These challenges highlight the need to expand chemical vapor deposition to low-temperature substrate materials.

First, a finite element model of a single nanowire was used to compare the piezoelectric potential in FF peptide and conventional piezoelectric materials. A 2D model of a flexible nanogenerator based on FF peptide microrods was created to predict the device performance. A flexible FF peptide nanogenerator was fabricated for mechanical energy harvesting, and the power generation was characterized.

Next, a finite element model was created to investigate a piezotronic force sensor design for haptics and prosthetics applications. The design, based on beam theory, consisted of two vertical arrays of ultra-long ZnO nanowires in a polymer matrix. Contact forces were applied to the model, and the piezopotential in the nanowires was calculated. The use of ultra-long ZnO nanowires grown by CVD was expanded to a soft polymer substrate by a mechanical transfer process. A stretchable piezotronic strain sensor was fabricated, and characterized.

Lastly, an apparatus for using low-temperature growth substrates inside of a high-temperature CVD furnace was designed and fabricated. The cooling assembly delivered chilled water to provide localized cooling for substrates inside the furnace. The cooling assembly was used to synthesize molybdenum disulfide (MoS_2) on a low-temperature iron pyrite (FeS_2) substrate in a CVD furnace.

In summary, finite element models predicted that FF peptide could generate significantly higher voltages than conventional piezoelectric nanomaterials for a given force. The first flexible piezoelectric FF peptide nanogenerator was fabricated and characterized, validating the model. A finite element model of a piezotronic force sensor predicted that the sensor could detect both shear and normal force components, and could exceed the force sensitivity of human mechanoreceptors. A stretchable piezotronic strain sensor was fabricated using a mechanical transfer process to expand CVD grown ZnO nanowires to a soft polymer substrate. The gauge factor of the piezotronic strain sensor exceeded that of conventional metal strain gauges. An apparatus for cooling substrates inside a high-temperature CVD furnace was demonstrated for the synthesis of MoS_2 on a low-temperature substrate. The results show that finite element models can successfully predict piezoelectric behavior in emerging nanomaterials, and inform the design of new piezoelectric nanomaterial devices. Expanding the high-temperature CVD process to low-temperature substrates can help to realize new device designs, and benefit the synthesis of emerging piezoelectric nanomaterials. Devices enabled by piezoelectric nanomaterials can provide solutions to challenges in sustainable energy and human health.

Table of Contents

List of Tables

List of Figures

Chapter 1. Introduction

1.1 The piezoelectric effect

The equations of mechanics describe how a material deforms when a force is applied. Consider a solid cylinder with a length of *L*, and a cross-sectional area *A*, as illustrated in figure 1.

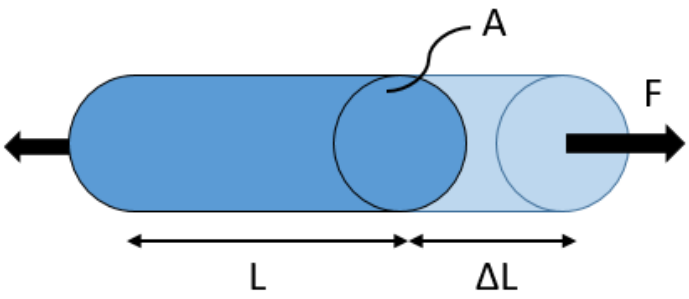

Figure 1. Uniaxial extension of a cylindrical rod.

A uniaxial force, *F* is applied along the length of the cylinder. *Stress* is defined as the force per unit area, and is given as

$$\sigma = \frac{F}{A}$$

where σ is the stress, *F* is the force, and *A* is the cross-sectional area. The force causes the cylinder to lengthen by an amount ΔL. The *strain* is a measure of this deformation and is defined as

$$\varepsilon = \frac{\Delta L}{L}$$

where ε is the strain, ΔL is the change in length, and *L* is the original length. For small strains, the relationship between stress and strain can be considered linear, and the material

is said to be *linear elastic*. For a linear elastic material, the relationship between stress and strain is given as

$$\sigma = E\varepsilon$$

where *E* is the *modulus of elasticity*, also called *Young's modulus*. The elastic modulus relates the applied stress to the deformation of the material. The equations above hold for uniaxial loading, and may be expanded upon to account for more complex loading conditions, and direction-dependent material properties.

Piezoelectricity is a property of crystalline materials with non-central symmetry. In non-centrosymmetric crystals, a mechanical stress or strain creates (or changes) a net displacement between the center of positive charge, and the center of negative charge. This creates an electric dipole moment, and induces charge polarization. The result is an electrical voltage in the material, as seen in figure 2. A converse piezoelectric effect also exists, in which an applied voltage induces strain in a piezoelectric material. There are 21 classes of crystals which possess non-central symmetry. The cubic class 432 is an exception, due to charge cancellation along the <111> axis. Piezoelectricity can be found in semiconductors including zinc oxide (ZnO), polymers such as poly(vinylidene fluoride-trifluoroethylene) (PVDF-TRFE), single atomic layer materials such as molybdenum disulfide (MoS_2), and in certain biological and bio-inspired materials including dry collagen, and diphenylalanine (FF) peptide microstructures (1-3). Among conventional piezoelectric materials, ceramics such as lead zirconate titanate (PZT) and barium titanate ($BaTiO_3$) are the most well-known. The inherent electromechanical coupling in

piezoelectric materials makes them well-suited for sensing, actuation, and mechanical energy harvesting.

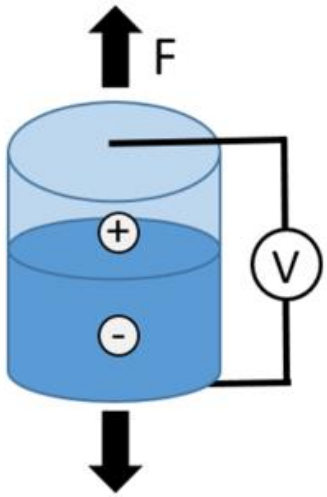

Figure 2. Electric potential in a piezoelectric material under applied displacement.

The constitutive equations for linear piezoelectricity are commonly given in either the stress charge form or the strain charge form. The stress charge form is given as

$$T = cS + e^T E$$

$$D = eS + \epsilon_0 \epsilon_r E$$

where *T* is the stress, *S* is the strain, *E* is the electric field, and *D* is the electric displacement. *c* is the stiffness matrix, *e* is the piezoelectric coupling matrix, and ϵ_o and ϵ_r are the permittivity of free space and relative permittivity, respectively. The strain charge form is similarly given as

$$S = sT + d^T E$$

$$D = dT + \epsilon_0 \epsilon_r E$$

where *s* is the compliance matrix and *d* is the piezoelectric coupling matrix.

The quantities that describe piezoelectric materials in the preceding equations are tensors with rank of either 4, 3, or 2. However there can be significant symmetries due to the physical crystal structures of piezoelectric materials.

In addition to electromechanical coupling, piezoelectric materials may also possess semiconducting properties. Semiconductors have electrical conductivity somewhere between insulators and metals, and are the basis for transistors and many electrical devices. Silicon is perhaps the most well-known among non-piezoelectric semiconductors. Examples of piezoelectric semiconductors include zinc oxide (ZnO), gallium nitride (GaN), and molybdenum disulfide (MoS_2).

1.2 Piezoelectric nanomaterials

Nanomaterials are defined as any material structure with a length scale on the order of 10^{-9} meters. Nanomaterials have many advantages over bulk materials due to their favorable scaling laws (4, 5). Nanomaterials often exist as quasi-2D or 1D structures such as monolayer materials and nanowires. Nanomaterials may have different properties from their bulk counterparts, and can play an important role in sensing and energy harvesting. Less material is required to produce nanomaterials, and material synthesis is often highly scalable (6). Nanomaterials have favorable scaling laws, and can have improved piezoelectric properties not seen in bulk materials. Certain semiconducting materials, such as MoS_2, may even switch from an indirect to direct bandgap at the nanoscale (3, 4, 7). The elastic modulus of ZnO nanowires is higher than that of bulk ZnO, and their single crystal nature is resistant to fatigue. (8, 9).

1.2.1 Zinc Oxide

Zinc oxide is a piezoelectric material which exists in 3 distinct crystal structures, zinc blende (sphalerite), rock salt, and wurtzite (10). Although all ZnO crystal structures are piezoelectric, the hexagonal wurtzite structure has been most heavily researched for sensing and energy harvesting applications (11, 12). Zinc oxide can be grown to form nanowires, which are high aspect ratio, quais-1D structures that can develop large piezopotentials. ZnO is a direct bandgap semiconductor with a wide bandgap of 3.37 eV (13). ZnO has an electron affinity of 4.2 eV, allowing it to form Schottky contacts with high work function metals such as gold and platinum. Brillson and Lu have comprehensively reviewed the formation of Schottky and Ohmic contacts with ZnO (14).

The favorable scaling properties of nanomaterials are illustrated by the enhanced mechanical properties of ZnO nanowires. Using transmission electron microscopy (TEM), Agrawal and colleagues measured the elastic modulus of ZnO nanowires (9). The elastic modulus of the ZnO nanowires increased from 140 GPa to 160 GPa as the diameter decreased from 80 nm to 20 nm. Gao et al. studied the piezopotential in a ZnO nanowire using finite element methods (15). The authors applied an axial load of 85 nN to a 1200 nm long nanowire model (figure 3a), and calculated a potential of 0.4 V along the c-axis of the nanowire as seen in figure 3b and figure 3c. When a pure torsional load was applied to the nanowire, no net potential was generated along the length of the wire, only small local potential gradients as seen in figure 3d. Tension or compression loads combined with torsion produced potentials similar to the pure axial load cases as shown in figure 3e and

figure 3f. These results suggest that the most significant piezoelectric potential is produced by strain in the c-axis, along the length of the nanowire.

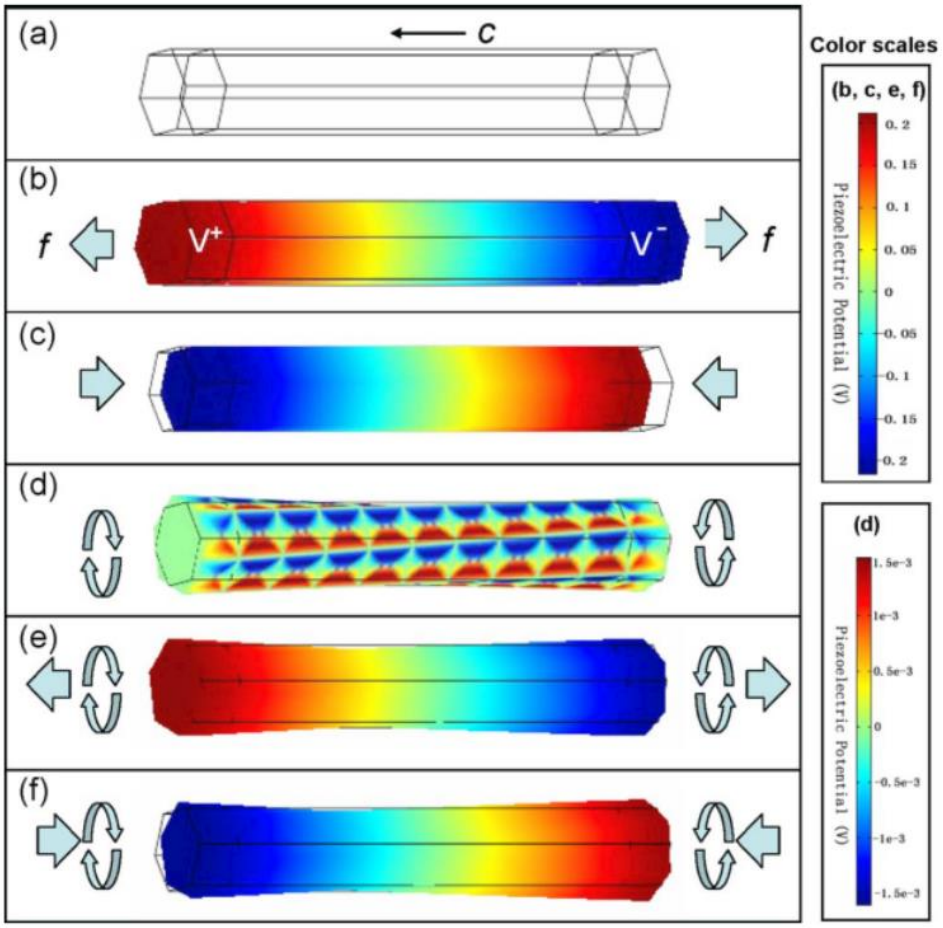

Figure 3. Electrostatic potential in ZnO nanowire under axial force. (a) Finite element model of a ZnO nanowire, length 1200 nm. Arrow indicates c-direction along the length of the wire. (b) Piezoelectric potential in the ZnO nanowire under 85 nN tensile force and (c) 85 nN compressive force. (d) Piezoelectric potential under a 60 nN twisting force pair. (e) Piezoelectric potential under simultaneous twisting and tension and (f) simultaneous twisting and compression. Reprinted from (15) with the permission of AIP publishing. Copyright 2009.

Gao and Wang similarly investigated the potential in laterally bent nanowires using finite element methods (16). The authors applied an 80 nN transverse load to the tip of the nanowire model, which resulted in a potential of about ± 0.3 volts across the diameter of the wire as seen in figure 4a and figure 4b. The analytical solution is shown in figure 4c, and is compared to the finite element model in figure 4d. ZnO nanogenerators have been developed to make use of the piezoelectric potential from both axial and transverse nanowire deflections.

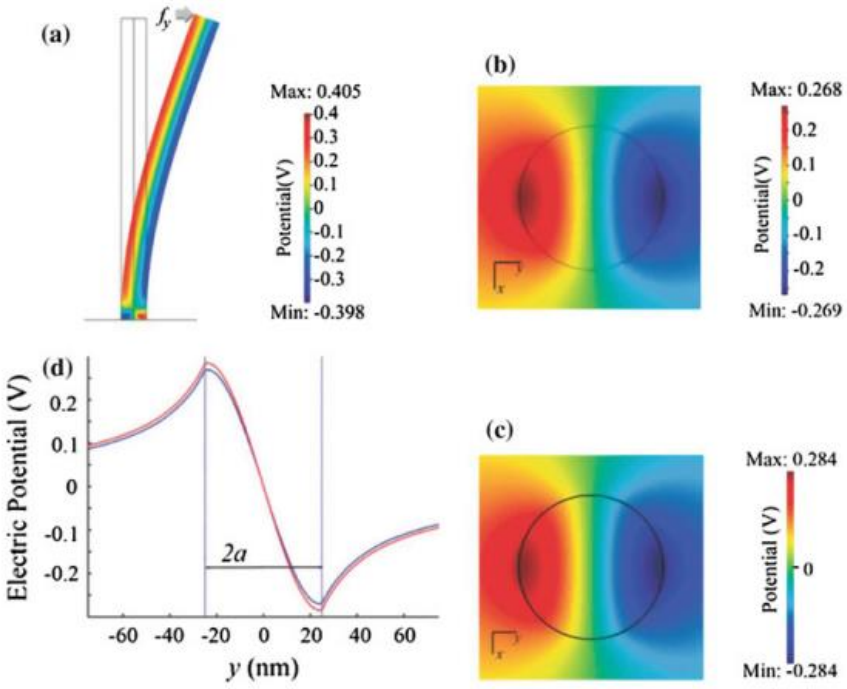

Figure 4. Electrostatic potential in a ZnO nanowire under transverse force. (a) Finite element model of piezoelectric potential in a ZnO nanowire under 80 nN transverse force. The nanowire has a length of 600 nm and a diameter of 50 nm. (b) Cross-sectional view of the nanowire in (a). (c) Analytical solution to piezoelectric potential in the cross-section of the nanowire. (d) Comparison between potential predicted by finite element model and analytical solution. Reprinted with permission from (16). Copyright 2007 American Chemical Society.

The hydrothermal method remains one of the most popular methods for synthesizing ZnO nanowires. The hydrothermal method is an aqueous solution method which produces arrays of vertical, well-aligned nanowires (6). Hydrothermal synthesis takes place at low temperatures below 100 ºC (17). The low process temperature is compatible with silicon, and also with flexible polymer substrates such as polyethylene terephthalate (PET) and polyimide (PI). Photolithography polymers can be used to pattern arrays of nanowires grown by hydrothermal synthesis.

Recipes for hydrothermal synthesis start with a solution containing a zinc salt such as zinc chloride or zinc nitrate (17). Hexamethylenetetramine (HMTA) acts as a pH buffer, producing OH^- ions, and decomposes to ammonia and formaldehyde upon heating (18-20). The ratio of zinc salt to HMTA is typically 1:1 or 2:1. The growth substrate is typically coated with a ZnO seed layer, using sputtering or sol-gel methods (12, 21). The substrate is floated face-down in a jar containing the solution, and heated. Growth times can range from hours to days.

During the reaction, zinc hydroxyl species form in the solution, which dehydrate to form zinc oxide nanowires on the seed layer (17). ZnO nucleation which forms nanowires on the seed layer is called heterogeneous nucleation. Ammonium hydroxide may also be added to the solution. Ammonia complexes with zinc ions, reducing homogeneous nucleation. Homogeneous nucleation is the unwanted formation of ZnO away from the nanowire growth substrate (22). The role of ammonia evaporation rate has been studied, and several distinct phases of nanowire growth have been identified (22).

The hydrothermal method produces nanowires with lengths from a few to tens of microns. Many techniques have been studied to increase nanowire length and reduce growth time, including microwave and laser assisted growth (22, 23). The hydrothermal method is popular due to its low temperature, low cost, and scalability. It is compatible with many substrate materials, making it well-suited for device fabrication.

1.2.2 Molybdenum disulfide

In addition to 1D structures such as nanowires, nanomaterials can also exist as a single atomic layer, or so called 2D materials. Perhaps the most famous example of 2D materials is graphene (24). The success of graphene has inspired research into other 2D materials, including molybdenum disulfide (MoS_2). MoS_2 is an inorganic compound, and like ZnO, has a hexagonal crystal structure (25). Single atomic layer MoS_2 has two distinct orthogonal crystal directions which are known as "zigzag" and "armchair" due to their appearances. Lattice constants for MoS_2 have been verified by XRD, and were found to be $a = b = 3.16$ Å, and $c = 12.29$ Å (26, 27).

Like many nanomaterials, single layer MoS_2 exhibits unique properties that are not found in the bulk material. MoS_2 is a semiconducting material, and in its bulk form has an indirect bandgap of 1.2 eV. In its 2D form, MoS_2 switches to a direct bandgap of about 1.8 eV (7, 28, 29). As a direct bandgap material, MoS_2 can be used for optoelectronics. MoS_2 can support large strains, and strain-engineering can be used to further tune the bandgap (30). Scalise and colleagues used density functional theory (DFT) to predict that MoS_2 would transition back to an indirect bandgap at approximately 2 % strain. At 8 %

strain, the material was predicted to exhibit metallic behavior. The elastic modulus of MoS_2 was calculated to be 435 GPa (31).

Monolayer MoS_2, like graphene, can be synthesized by mechanical exfoliation (7). Chemical vapor deposition can also be used to grow monolayer MoS_2, either directly from MoS_2 powder, or by sulfurization of molybdenum trioxide (MoO_3) (32, 33). Si/SiO_2 is typically used as a growth substrate. Piranha solution is often used as substrate cleanliness can affect growth (27). CVD produces single crystal, equilateral triangle shapes as seen in figure 5. The thickness of single atomic layer MoS_2 is approximately 0.7 nm (32). Nucleation of MoS_2 crystals occurs preferentially near cracks and other surface imperfections, and can be controlled by surface modification techniques. Large area growth of monolayer MoS_2 from triangular grains remains challenging. Najamei and colleagues identified two mechanisms for grain boundary formation, chemical bonding between in-plane grains, and the overlapping of adjacent grains (32).

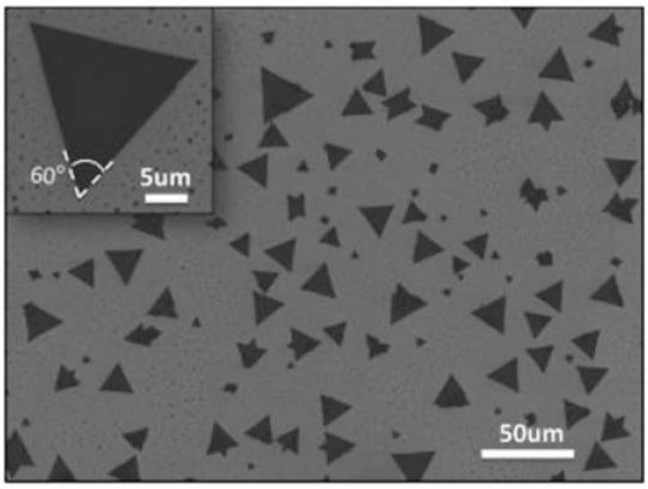

Figure 5. SEM image of monolayer molybdenum disulfide flakes. MoS_2 monolayer flakes form in a characteristic equilateral triangle morphology. Flakes were grown on Si/SiO_2 substrate. Reprinted with permission from (33). Copyright 2013 American Chemical Society.

Van der Waals (vdW) epitaxy is an approach that allows for the growth of MoS_2 on lattice-mismatched substrates. Conventional epitaxial growth relies on chemical bonds between the substrate and MoS_2 material. Van der Waals epitaxy, however, relies on the van der Waals interactions between MoS_2 and the growth substrate (34). Despite the lattice mismatch, graphene has been successfully used as a growth substrate for vdW epitaxy methods. Graphene is an ideal substrate for vdW epitaxy due to the lack of dangling bonds, which prevents the formation of strong chemical bonds between MoS_2 and the substrate. MoS_2 can be grown with two preferred orientations on graphene, shown in figures 6a-c. (35, 36). Figures 6d-f show corresponding AFM topography, and an SEM image of MoS_2 grown on sapphire is shown in figure 6g.

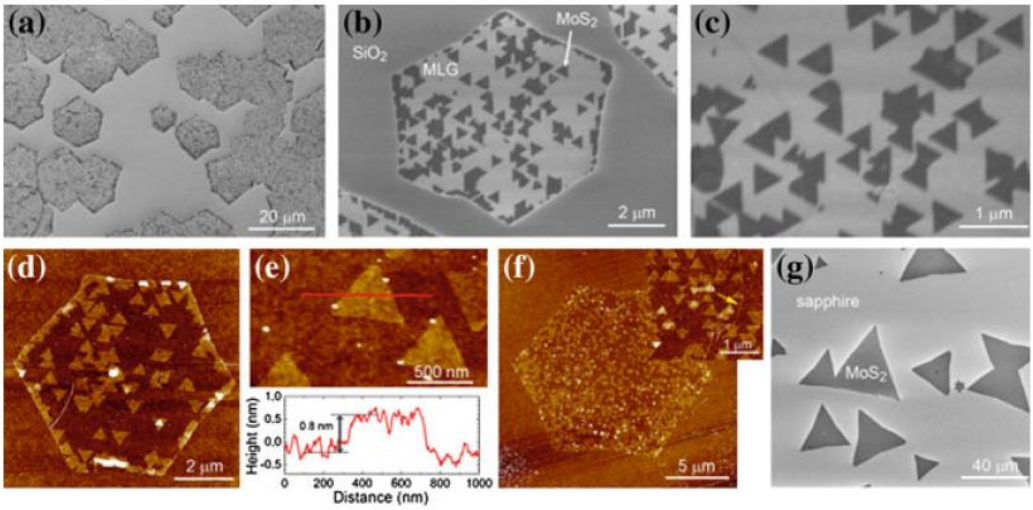

Figure 6. Van der Waals epitaxy of MoS_2 on graphene. (a-c) SEM images of MoS_2 crystals produced by van der Waals epitaxy on graphene. (d-f) AFM scans corresponding to SEM images. Inset shows topography profile for MoS_2 flake. (g) MoS_2 flakes grown on sapphire substrate. Reprinted with permission from (36). Copyright 2015 American Chemical Society.

Piezoelectricity in single and few-layer MoS_2 flakes was studied by Wu et al. for energy harvesting (3). MoS_2 flakes were exfoliated onto a PET substrate, and metal electrodes were deposited across the flakes. A periodic strain was applied in the "armchair" direction, and the output voltage was measured. Piezoelectric response was investigated for even and odd number layers of MoS_2 flakes. Piezoelectricity was only observed for odd-number layered samples, and decreased with increasing number of layers. No piezoelectricity was observed in even-number layered samples. This result is consistent with experimental results showing that only odd-number layered MoS_2 is non centro-symmetric (37). Zhu et al. used atomic force microscopy to measure a piezoelectric coefficient e_{11} = 2.9e-10 C/m (38). Since the prediction and measurement of

piezoelectricity in single layer MoS_2, there has been much work on its synthesis and characterization. MoS_2 has great potential for many piezoelectric applications such as energy harvesting.

1.2.3 Diphenylalanine peptide

One promising approach to bio-inspired piezoelectric materials are peptides. Peptides are defined as any chain of two or more amino acids. Dipeptide molecules based on diphenylalanine can self-assemble into nanotubes, hydrogels, and other structures (39-42). The nanotube structure of self-assembled FF peptide has potential applications for drug delivery (43). FF peptide is also known for its role as the core recognition motif for Alzheimer's beta amyloid fibrils, leading to growing interest in the study of its self-assembly and material properties (5).

Self-assembled FF peptide nanotubes and microrods have a hexagonal structure and demonstrate piezoelectricity, which can be improved by poling (44). Piezoelectricity is relatively rare among biomaterials, with dry collagen being a notable example (45). The properties of self-assembled FF peptide structures are impressive among biomaterials. Experimental measurements for elastic modulus range from 19-27 GPa, and the origin of this high stiffness has been explored through diffusion tensor theory (46-48). Values up to 18 pm/V have been achieved for the piezoelectric coefficient d_{33} by poling the material during growth under an electric field (49, 50).

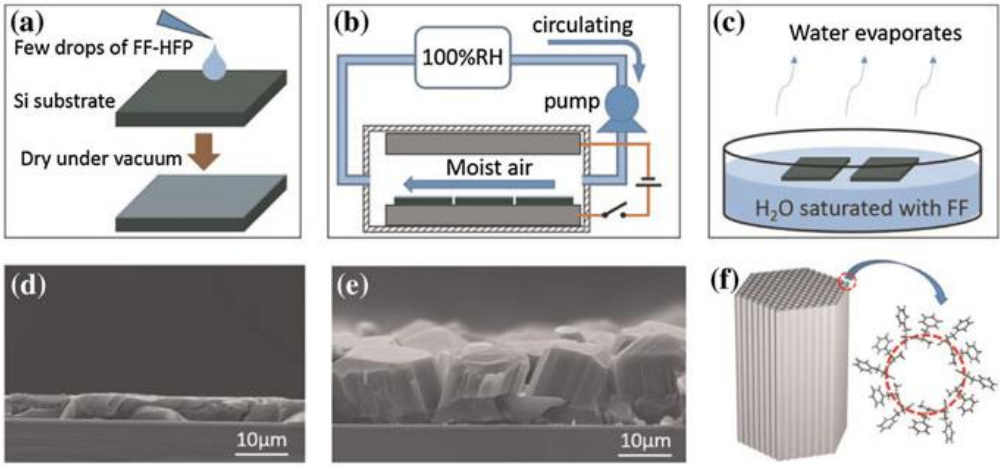

Figure 7. Synthesis of FF peptide microrods. (a) Deposition of amorphous seed layer and (b) crystallization of seed layer. (c) Growth of FF peptide microrods. (d) SEM image of FF peptide seed layer. (e) SEM image of FF peptide microrods. (f) Schematic of FF peptide microrod structure with nanochannels. Reprinted from Nano Energy, vol 17, Nguyen et al., Epitaxial growth of vertically aligned piezoelectric diphenylalanine peptide microrods with uniform polarization. 323-329. Copyright 2015, with permission from Elsevier (50).

Kol and colleagues used atomic force microscopy to measure the point stiffness of FF peptide nanotubes (46). Based on multiple measurements, the authors calculated an average stiffness of 160 N/m. The authors used this stiffness value, along with AFM topography scans, to create a finite element model of an FF peptide nanotube. Based on this model, the Young's modulus was calculated to be 19 GPa for the nanotubes.

Kholkin et al. investigated the piezoelectric effect in FF peptide nanotubes (2). Nanotubes of varying size were scanned along the long axis with piezoresponse force microscopy (PFM). The PFM response data was calibrated against a sample of $LiNbO_3$ with known piezoelectric properties. Based on these results, the authors calculated a d_{15}

piezoelectric coefficient of 60 pm/V. The piezoelectric effect in FF peptide nanotubes is temperature dependent, and was studied by Heredia et al. Piezoelectricity in FF peptide was found to decrease as the temperature increased, and was completely lost at 140 ºC, due to a crystalline phase transition (51).

Diphenylalanine peptide structures are commonly synthesized by solution-based self-assembly (52-55). Nguyen et al. developed a process for epitaxial growth of vertically aligned FF peptide microrods (50). Figure 7 details the FF peptide synthesis process including formation of the amorphous seed layer in figure 7a, seed layer crystallization in figure 7b, and growth of FF peptide microrods in figure 7c. SEM images of the crystallized seed layer and FF microrods are shown in figure 7d and figure 7e respectively, and a drawing of the hexagonal microrod structure is given in figure 7f.

1.3 The piezotronic effect

The piezotronic effect was first realized in 2006 by Z.L. Wang's group (56). The foundation of the piezotronic effect is the metal-semiconductor heterojunction, or the interface between a metal and a semiconductor. The semiconductor material is also a piezoelectric material, which develops an electric potential in response to strain. This piezoelectric potential in the semiconductor modifies the barrier height and controls conductivity at the metal-semiconductor interface. This is called the piezotronic effect.

A typical piezotronic device consists of a metal-semiconductor-metal structure. The metal layers serve as the electrodes, and a bias voltage is applied across the device, resulting in the flow of current. The metal-semiconductor interface typically uses a high work function metal such as gold, which can create a Schottky contact, resulting in

rectifying, nonlinear current-voltage (I-V) behavior (56). Figure 8 shows a comparison between a conventional MOSFET transistor in figure 8a and a piezotronic transistor in figure 8b. In the conventional transistor, an external gate voltage controls conductivity across the channel width. In a piezotronic transistor, the potential in the piezoelectric semiconductor controls conductivity at the metal-semiconductor interface. In both cases, a bias voltage drives current through the device, and the amount of current that flows is controlled by either the gate voltage or by the piezoelectric potential. Piezotronic devices may be thought of as "strain-gated" transistors, since the strain-induced piezoelectric potential is analogous to a gate voltage.

The piezotronic effect has enabled sensors for many applications including force and strain sensing, photodetectors, and chemical and biosensors (57).

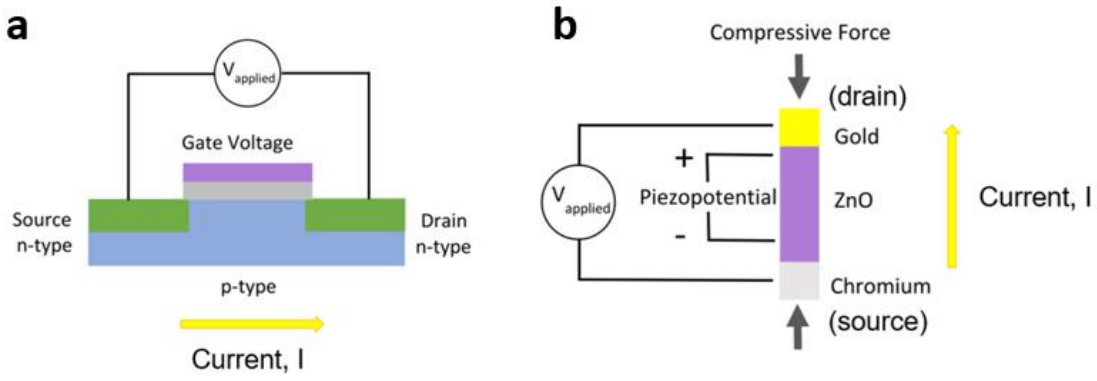

Figure 8. Conventional and piezotronic transistors. (a) Conventional transistor with conductivity modulated by external gate voltage. (b) Piezotronic transistor with conductivity modulated by piezoelectric potential.

1.4 Review of energy harvesting with piezoelectric nanomaterials

The electromechanical coupling makes piezoelectric materials especially well-suited for harvesting mechanical energy (58). Piezotronic materials such as ZnO, which

have piezoelectric and semiconducting properties, have played an important role in the development of nanoscale energy harvesting devices (59). MEMS devices and nanoscale systems present new opportunities and challenges for nanoscale power generation. Applications include wearables, implantable medical devices, remote structural health monitoring, and other self-powered systems. Nanogenerator performance has been steadily improving, and emerging materials are opening new avenues for research. Piezoelectric nanomaterials are uniquely suited to collect previously neglected sources of energy, such as biomechanical energy and low intensity vibrations in the environment (60).

1.4.1 Review of energy harvesting with zinc oxide

In 2006, Wang's group presented the first demonstration of energy harvesting with piezoelectric ZnO nanowires (60). Using an array of vertical ZnO nanowires, the authors converted mechanical energy from an atomic force microscope (AFM) into electrical energy. ZnO nanowires were grown on an Al_2O_3 substrate by a vapor-liquid-solid (VLS) method. The reaction was catalyzed with gold, resulting in a gold nanoparticle on the tip of each nanowire. Individual nanowires were scanned by AFM in contact mode, with a force of 5 nN. Silver paste formed an Ohmic contact at the bottom of the nanowire, and the platinum-coated AFM tip formed a Schottky contact with the top of the nanowire. The output voltage was measured across an external load resistance, and reached 6-9 mV. By using the AFM topography scan, the authors could estimate the deflection of individual nanowires. By comparing the elastic energy needed to deform the wires with the piezoelectric output, an efficiency of 17-30 % was calculated. The piezopotential in a laterally bent ZnO nanowire develops across the diameter of the nanowire, as seen

previously in figure 4. The nanowire develops a positive potential on the tensile side, and a negative potential on the compressed side. In cases where the gold nanoparticle remained on top of the nanowire, the piezopotential was neutralized by free carriers and no output was measured. For many nanowires, the gold nanoparticle fell off of the nanowire tip. In this case, when the AFM tip scanned across the tip of the nanowire, it formed either a forward or reversed-biased Schottky contact, depending on the potential in the nanowire. Therefore, both the piezoelectric and semiconducting properties of the nanowire contributed to the power generation. The authors calculated an output power density of 10 $pW \cdot \mu m^{-2}$, demonstrating the energy harvesting ability of ZnO nanowires.

A standalone nanogenerator was developed using arrays of 1 µm long ZnO nanowires on gallium nitride (GaN) and sapphire substrates (11). A silicon wafer was patterned with an array of triangular pyramids and coated with platinum, to form the top electrode. This top electrode was placed on top of the nanowire array, and connected with polymer strips. In effect, this created an array of ZnO nanowires, each with their own AFM tip. The resulting nanogenerator had an area of 2 mm^2. The nanogenerator was driven by ultrasonic waves at a frequency of 41 kHz. The relative motion of the platinum-coated pyramids and the ZnO nanowires caused some nanowires to deflect laterally, creating piezoelectric potential. When the pyramids contacted the tensile side of the nanowire, the reverse-biased Schottky contact caused charge buildup. As the motion between the pyramids and nanowires continued, the pyramids moved to the compressive side of the nanowires, creating a forward-biased Schottky contact and discharging. The net effect of multiple charging and discharging Schottky contacts was a mostly constant DC output

voltage. The output voltage was measured to be about 7 mV, and output currents were at the nA scale. The power output of the nanogenerator was estimated to be 10 $\mu W \cdot cm^{-2}$.

The concept of a nanogenerator based on vertical arrays of ZnO nanowires was expanded by stacking multiple devices together (12). Using silicon substrates with a sputtered ZnO seed layer, Xu and colleagues grew ZnO nanostructures on each side of the substrate. On one side, long ZnO nanowires were formed. On the other side, short, conical ZnO nanotips were grown. The nanotips were coated with a thin layer of gold, and formed a structure similar to the AFM tip or pyramids in the previous works. Like platinum, gold can also form a Schottky contact with ZnO nanowires. Multiple silicon substrates were stacked together so that the nanowires on one layer were in contact with the nanotips on the layer above as seen in figure 9. Figures 9a-f detail the nanogenerator fabrication process, and SEM images of the ZnO nanowires and nanotips are shown in figure 9g and figure 9h, respectively. The stacked nanogenerator was subjected again to ultrasonic vibrations. As with the single layer design, the Schottky contact switched from reverse-biased to forward-biased as the nanotips moved across the nanowire. The sum of contributions from all nanowire/nanotip pairs resulted in a relatively stable DC output. The stacked nanogenerator architecture produced higher outputs than a single layer nanogenerator. Output current was measured to be 10 nA and 13 nA for two individual nanogenerators, and increased to 22 nA when they were connected in parallel. An antiparallel configuration reduced the combined output to 3 nA. When connected in series, two nanogenerators produced 3.5 mV compared to 2.6 mV and 0.8 mV individually. By connecting 4 nanogenerators, the authors produced an output voltage of 62 mV and an

output current of 105 nA. The output power produced by four stacked nanogenerators was 0.11 $\mu W \cdot cm^{-2}$.

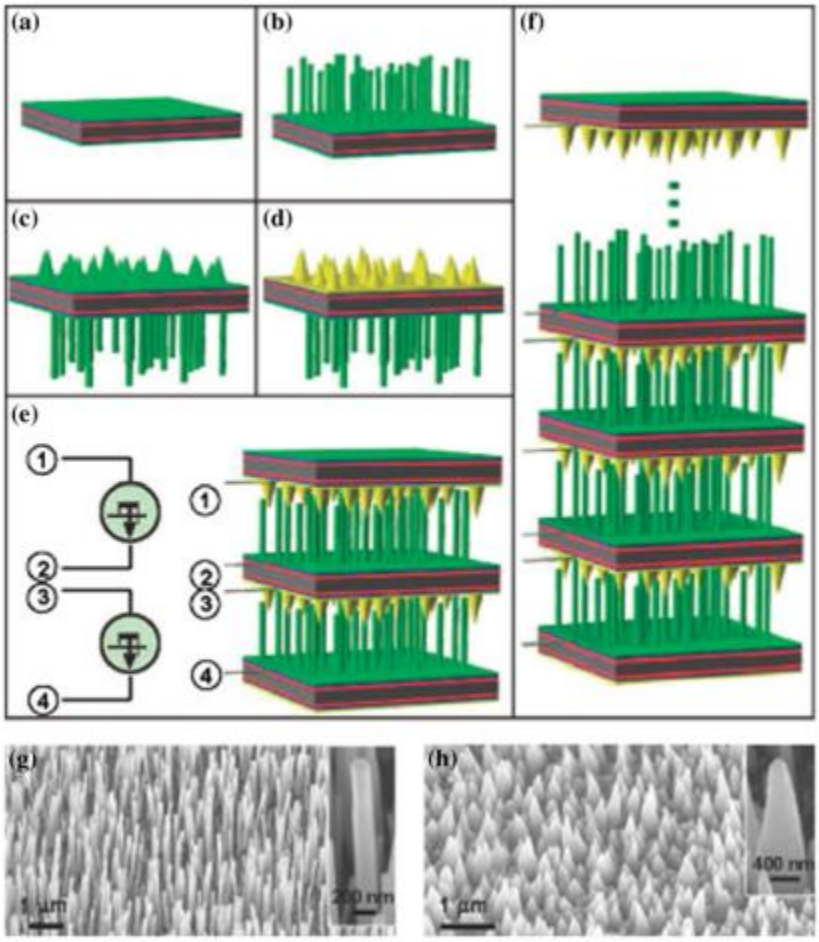

Figure 9. Multilayer nanogenerator based on vertical arrays of ZnO nanowires. (a-d) Fabrication steps of multilayer nanogenerator beginning with (a) ZnO seed layer, (b) growth of ZnO nanowires, (c) growth of ZnO nanotips on opposite side, and (d) gold deposition on nanotips. (e) Assembled 2-layer nanogenerator and circuit diagram. (f) SEM images of (g) nanowires and (h) nanotips. Reprinted with permission from (12). Copyright 2008 American Chemical Society.

Energy can also be harvested from laterally oriented ZnO nanowires. Yang et al. created a single wire generator (SWG) using a single 200-300 μm long ZnO microwire

(61). The microwire was placed flat on a 50 μm thick Kapton film, and silver paste was applied to form electrodes on both ends as presented in figure 10a. The wire was then packaged with a flexible polymer. When the flexible substrate was bent, the microwire on the outer surface experienced tension. In this example, potential developed along the length of the microwire as previously seen in figure 3, as opposed to across the diameter. Applying a periodic strain produced an alternating current. Although silver paint was used on both ends of the wire, one of the junctions formed a Schottky contact, while the other formed an Ohmic contact. The difference was due to the ZnO crystal structure, because the ends of the wire could terminate with either ZnO or oxygen. The device was tested under a periodic strain ranging from about 0.05 % to 0.1 %. The output current and voltage increased with increasing strain rate, and the device was stable over 2 hours of testing. Electrical output was measured to be 50 mV and 750 pA, with an efficiency of 6.8 %. The SWG was used to extract biomechanical energy from human movement (60). The device was attached to a human finger, and generated 25 mV and 150 pA under periodic flexing. The I-V behavior of the device is presented in figure 10b, and the voltage and current generated from biomechanical motion are shown in figure 10c and figure 10d, respectively.

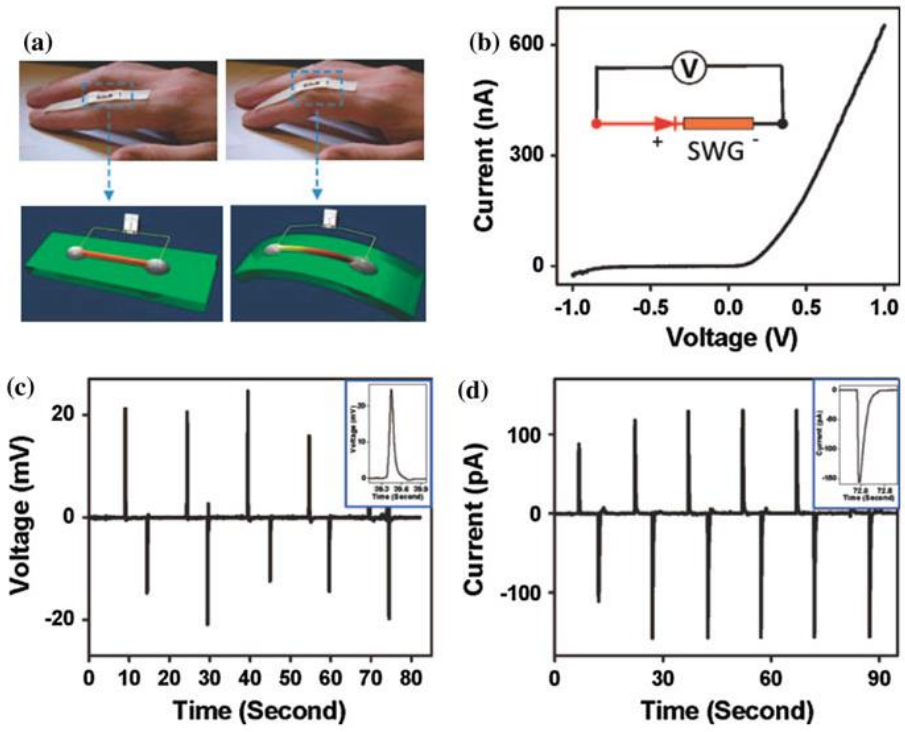

Figure 10. Lateral microwire nanogenerator for biomechanical energy harvesting. (a) Harvesting biomechanical energy from human finger. (b) Nonlinear, rectifying I-V behavior of the nanogenerator, and equivalent circuit diagram. (c) Measured voltage and (d) current associated with finger flexing. Reprinted with permission from (60). Copyright 2009 American Chemical Society.

The SWG based on a lateral ZnO microwire could also be expanded to an array of lateral nanowires. Using the hydrothermal method, the authors grew rows of horizontally aligned nanowires on a flexible substrate (62). In total 700 rows were patterned, with an estimated 20,000 nanowires per row. A gold electrode was deposited over the end of each row, creating a Schottky contact with the nanowires in that row. The device generated an output voltage of 1.26 V and a current of 288 nA. The nanogenerator was used as part of a self-powered system, and could power a nanoscale pH sensor and UV sensor.

1.4.2 Review of energy harvesting with molybdenum disulfide

Energy harvesting with piezoelectric nanomaterials has also been explored with single atomic layer, or so called 2D materials. Wu et al. investigated piezoelectricity in single-layer MoS_2 for energy harvesting (3). Single atomic layer flakes of MoS_2 were prepared by exfoliation. The flakes were triangular, with a typical size of about 5 μm x 10 μm as shown in figure 11a. Single harmonic generation (SHG) was used to identify the crystal structure orientation for each flake as seen in figure 11b. This orientation was superimposed onto optical images of the flakes, and the "armchair" and "zigzag" directions of the crystal lattice were identified. A single flake was placed on a flexible PET substrate. The SHG data was used to orient and deposit metal electrodes made from Cr/Pd/Au layers as shown in figure 11c. By orienting the electrodes, the authors could apply a strain in the "armchair" direction when the substrate was bent, as illustrated in figure 11d. The output current and voltage were measured under a periodic strain. The device produced an open circuit voltage of 18 mV at 0.64 % strain, and an output current of 27 pA as seen in figure 12a. Figure 12b shows the output voltage as a function of strain. Power generation is shown in figure 12c, and was calculated by measuring the output across an external load resistor under periodic 0.53 % strain. With an external load of 220 MΩ, the device produced 2 $mW \cdot m^{-2}$, with an efficiency of 5 %. Figure 12d shows long term stability of the device output.

The MoS_2 generator was expanded to an array of multiple connected flakes. This time, triangular MoS_2 flakes were grown by CVD and transferred to a flexible PET substrate. Differences in edge morphologies were observed to identify the "armchair"

direction on the flakes (63). As many as four MoS_2 flakes were connected together. The output current and voltage increased with the number of flakes. In addition to the number of flakes, the piezoelectric potential was also investigated as a function of the number of atomic layers in a single flake. No piezoelectricity was observed in flakes with an even number of atomic layers, and piezoelectricity decreased with an increasing odd number of layers as seen in figure 12e. This result is consistent with a theoretical study performed by Zhou et al. (64). The results also suggest that MoS_2 nanogenerators will have a significantly lower capacitance than ZnO nanogenerators, making them well-suited for high frequency energy harvesting.

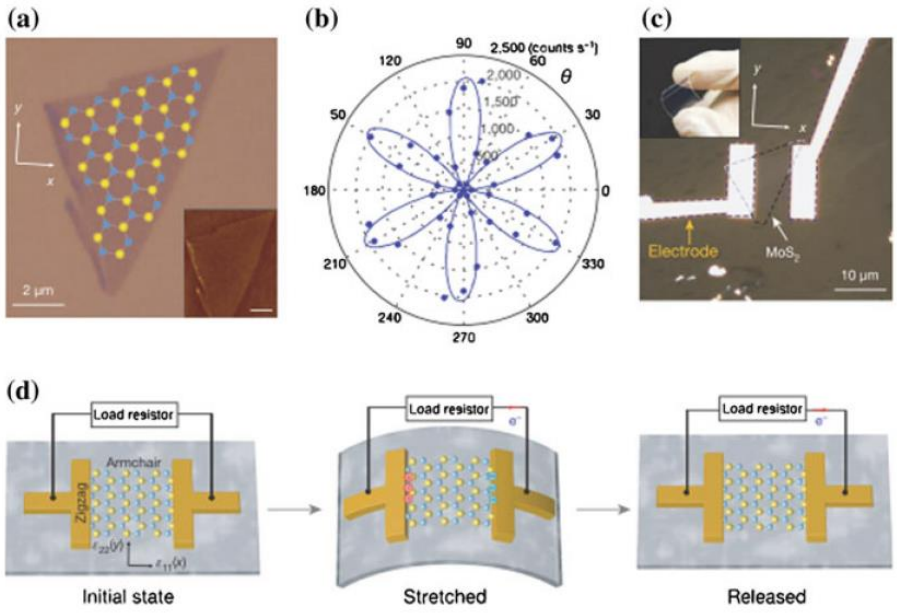

Figure 11. Monolayer MoS_2 nanogenerator. (a) Armchair and zigzag lattice directions superimposed on MoS_2 flake. (b) SHG data plotted in polar coordinates. (c) Completed energy harvesting device with electrodes oriented to measure strain in the armchair direction. (d) Schematic showing working mechanism of nanogenerator. Reprinted by permission from Macmillan Publishers Ltd: Nature, (3), Copyright 2014.

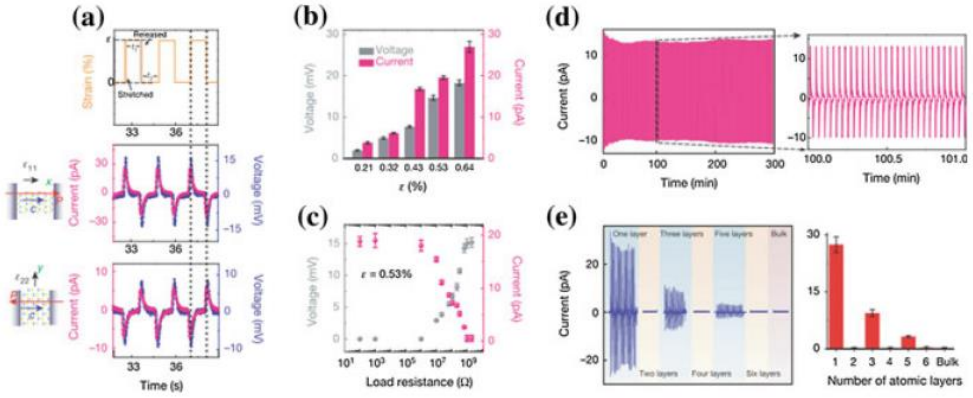

Figure 12. Energy harvesting characteristics of MoS_2. (a) Applied periodic strain (top), and current and voltage output for armchair (middle) and zigzag (bottom) directions. (b) Output voltage and current vs. strain. (c) Current and voltage as a function of external load. (d) Long-term stability of device output under periodic strain. (e) Current decreases with increasing number of MoS_2 layers. Reprinted by permission from Macmillan Publishers Ltd: Nature, (3), Copyright 2014.

1.4.3 Review of energy harvesting with diphenylalanine peptide

Much of the work on nanoscale energy harvesting has relied on piezoelectric inorganic semiconductors. Biological and Bio-inspired materials can also exhibit piezoelectricity, and have been the subject of recent interest for energy harvesting. Nguyen and colleagues demonstrated energy harvesting with vertical arrays of diphenylalanine peptide microrods (44). FF peptide microrods were grown on a silicon substrate using a low-temperature synthesis process (50). A positive or negative electric field was applied during the growth to control the polarization of the microrods. The polarization was characterized with piezo-force response microscopy (PFM), and the authors measured a piezoelectric coefficient $d_{33} = 17.9\ \text{pm}\cdot\text{V}^{-1}$. The FF peptide microrods were placed between

two gold electrodes, and a linear motor was used to apply a periodic force of 60 N to the microrod array as shown in figure 13a-b. The device produced an open-circuit voltage of 1.4 V and a short-circuit current of 39.2 nA as seen in figure 13c and figure 13d, respectively. By connecting the device to an external load resistance, the power output was measured to be 3.3 $nW \cdot cm^{-2}$ as given in figure 13e. Figure 13f shows that power output was greatly increased for FF microrods grown under an electric field, compared to microrods grown without an electric field, confirming the importance of polarization. The device performance was stable over 1,000 cycles. Three FF peptide nanogenerators were stacked together and connected to power a liquid crystal display (LCD) which read 'FF' when the nanogenerator was pressed with a human finger.

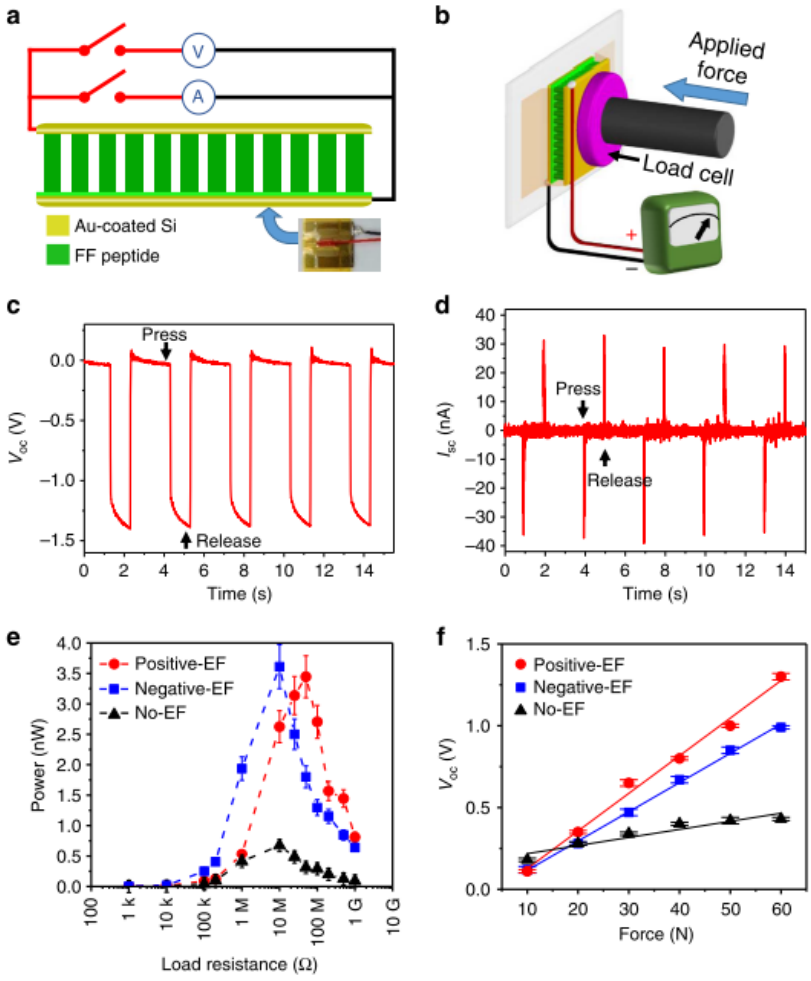

Figure 13. Energy harvesting characteristics of FF peptide. (a) Schematic of device structure. (b) Illustration of electrical measurement under applied force. (c) Open-circuit voltage under periodic applied force. (d) Short-circuit current under periodic applied force. (e) Power generation as a function of external load resistance for different polarization conditions. (f) Output voltage as a function of force for different polarization conditions. Reprinted from Nguyen, Vu, et al. "Self-assembly of diphenylalanine peptide with controlled polarization for power generation." Nature communications 7 (2016): 13566.(44), (CC BY 4.0).

1.5 Review of strain and force sensing with piezotronic nanomaterials

1.5.1 Piezotronic strain sensing

Due to the fact that strains generate electric potentials in piezoelectric materials, piezotronic devices are well-suited for strain and force sensing. It is the strain-generated piezoelectric potentials that control charge transport across the metal-semiconductor junction (56). Not surprisingly, the majority of piezotronic devices reported in the literature are strain and force sensors. While there are many unique approaches to piezotronic strain sensing, common themes emerge regarding materials, device architecture, characterization, and performance.

1.5.2 Materials and morphology for piezotronic strain sensors

Most piezotronic strain sensors are based on materials such as ZnO and GaN. These materials are most commonly synthesized as nanowires, although nanobelts and thin-film approaches have also been explored (65-74). Nanowire devices may consist of either single nanowires, or arrays of nanowires. The single nanowire approach allows for very high sensitivity, while arrays of nanowires are robust and stable due to the redundancy of multiple wires (65, 67, 70).

Flexible polymer substrates act as simple beams in bending. The outer surfaces of the beam experience the highest bending stresses, either in tension or compression. Single nanowires are commonly placed flat on the surface of such flexible substrates, and the bending stress causes strain in the wire. Although nanowires placed on the surface of a flexible substrate technically also experience bending stress, it is often reasonable to assume that the nanowire is experiencing pure tension or compression due to the relative

size and material properties (65, 68, 74). The result is a piezopotential that develops along the length of the nanowire between the source and drain electrodes. Vertically oriented nanowire arrays can also measure strain due to the Poisson effect, and have achieved higher gauge factors than single nanowire devices (67). Nanowires can be incorporated to form hybrids with other materials such as carbon fibers, demonstrating the potential for fabric-based piezotronic devices (72).

Although ZnO is most commonly used, piezotronic strain sensors have been developed from other materials including $ZnSnO_3$. Wu et al. achieved a gauge factor of 3740 for a $ZnSnO_3$ nanowire strain sensor, the second highest value reviewed here (74). $ZnSnO_3$ is promising due to its high c-axis polarization, which was calculated to exceed that of ZnO (74-76).

Single nanobelt strain sensors have been fabricated from GaN, which is reported to have better atmospheric stability and acid resistance than ZnO (66). This work also investigated the effect of c-axis orientation relative to bending direction. Liang et al. demonstrated a strain sensor using a piezoelectric tellurium microwire (71).

1.5.3 Device architecture for piezotronic strain sensors

Common design elements exist among piezotronic, nanomaterial-based strain sensors. The device is typically fabricated on a flexible substrate such as polyethylene (PET) or polystyrene (PS). Piezotronic devices require a metal-semiconductor heterojunction, with the metal forming either a Schottky or Ohmic contact with the piezoelectric, semiconducting nanostructure, depending partly on the work function of the metal (65-69, 71-74). High work function metals are typically used, especially gold, silver,

indium-tin-oxide (ITO), and platinum. The Schottky contact may be symmetric or asymmetric, and the devices are usually encapsulated in PDMS or another polymer to protect against contamination, corrosion, and physical damage.

Incorporating nanomaterials into strain sensing devices remains challenging. ZnO nanowires are commonly grown using the low temperature hydrothermal method, or by high temperature methods such as CVD (67, 69, 72). While hydrothermal synthesis is low cost, scalable, and compatible with flexible polymer substrates, achieving long nanowires remains difficult. Chemical vapor deposition readily results in long, high quality nanowires, but the high temperatures are not compatible with polymer substrates or photolithography patterning techniques (77). Thin-film piezotronics approaches are being developed and show promise (78).

1.5.4 Device characterization and performance

Piezotronic devices are commonly characterized by their nonlinear, rectifying I-V behavior, to which they owe their high sensitivity. The devices are driven by bias voltages ranging from -3 V to + 3 V, and typical output currents are on the order of a few to tens of microamps (65-69, 71-74). The metal-semiconductor-metal structure may have a Schottky contact at each interface, or one of the contacts may be Ohmic (67). If the same metal is used for both the source and drain electrode, the device will typically have a symmetric I-V curve. Devices with different source and drain metals will have asymmetric barrier heights at the metal-semiconductor junctions, resulting in rectifying behavior (67, 72). Charge transport across the barrier can be explained by the thermionic emission diffusion model (65, 74).

As a whole, piezotronic strain sensors exhibit several promising performance characteristics. Piezotronic sensors are known for their high sensitivity and resolution, fast response times, and stability. Yang et al. estimated that ZnO nanowires could achieve response times as fast as 10 ms. ZnO nanowires were used to accurately detect AFM tip vibrations from 0.11 to 0.33 Hz (68). Reported response times for piezotronic strain sensors range from 10 ms to 500 ms (65, 69).

The figure of merit for strain sensors is called the gauge factor. Gauge factor is a measure of sensitivity to strain, defined as the normalized change in current over the strain, and given as

$$Gauge\ Factor\ (GF) = \left| \frac{\Delta I / I_0}{\varepsilon} \right|$$

Where I_0 is the zero strain current, and ΔI is the change in current due to a strain ε. The highest reported gauge factor reviewed here for a piezotronic strain sensor was 4036 by Zhang et al. (69). By comparison, a review of piezoresistive strain sensors based on graphene reported gauge factors up to 300 (79). The gauge factor for a conventional metal strain gauge is approximately 2 (80). Response times are typically measured by applying periodic displacements with a linear motor or mechanical stage, and observing the dynamic response of the output current. Measurements tend to be reproducible, with the I-V curve returning to the unstrained state after unloading (65, 66). In principle, the piezotronic effect is a persistent, but the current can drop in time due to charge trapping by impurities and vacancies in the semiconductor (74). Therefore, the high quality, low defect nature of many nanomaterials makes them appealing for piezotronics. The intrinsic

electromechanical coupling, high sensitivity and fast response times make piezotronic devices ideal for strain sensing. A summary and comparison of reviewed piezotronic strain sensors is provided in Table 1.

Zinc oxide nanowires are a common material for piezotronic strain sensors, due to their semiconducting properties and enhanced piezoelectricity. Zhou et al. demonstrated a characteristic example of a piezotronic ZnO nanowire strain sensor (65). Zinc oxide nanowires were grown by thermal evaporation, with diameters between 2-6 μm and lengths from hundreds of microns to millimeters. A single ZnO nanowire was transferred to a flexible polystyrene substrate. Silver paste was used to connect each end of the nanowire to the substrate as seen in figure 14a. The silver paste formed Schottky contacts with the ZnO nanowire and served as the source and drain electrodes. PDMS was used to encapsulate the device for protection.

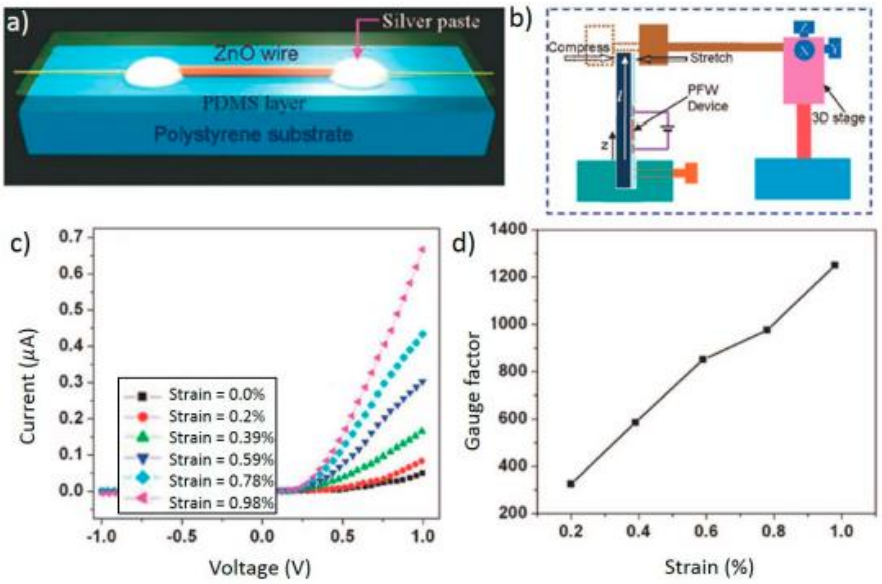

Figure 14. Single ZnO nanowire piezotronic strain sensor. (a) Strain measurement setup. (b) I-V characteristic as a function of applied strain. (c) Gauge factor as a function of strain. Adapted with permission from (65). Copyright 2008 American Chemical Society.

The strain sensor was tested by fixing one end and attaching the other end to a moveable stage as seen in figure 14b (65). The authors concluded that the nanowire experienced pure tensile or compressive strains along the c-direction of the wire, based on the geometry and mechanical properties of the device. Using a bias voltage of ± 1 V, the authors measured the I-V behavior of the device for strains up to 0.98 %, shown in figure 14c. The results confirmed the existence of a rectifying, nonlinear Schottky contact between the ZnO and silver paste. The sensitivity of the device was calculated for varying strains and is presented in figure 14d. The device achieved a gauge factor of 1250, higher than the value of 850 achieved by a piezoresistive carbon nanotube (CNT) sensor (81).

The device had a fast response time of 10 ms, and long-term performance was stable for periodic deflections.

In addition to nanowires, nanobelts are another morphology commonly used for strain sensors (69). Zhang et al. developed a ZnO nanobelt strain sensor with the source and drain electrodes on the same monopolar ZnO surface. The use of the monopolar surface greatly simplified device fabrication, and the nanobelt was doped with indium to improve the mechanical properties. The 20 μm long by 180 nm wide nanobelt was placed on a flexible polystyrene (PS) surface, and packaged with PDMS.

Device testing was accomplished by fixing one end of the sensor, and applying a lateral displacement to the free end (69). I-V characteristics were measured for a bias voltage swept over ± 3 V for strains from -0.4 % to + 0.3 %. The authors characterized the change in Schottky barrier height as a function of bias voltage and applied strain. The gauge factor was calculated for both tensile and compressive strains, with a maximum gauge factor of 4036 for compressive strains and 135 for tensile strains. The authors hypothesized that increased carrier mobility from the piezoresistive effect may have caused screening, resulting in the large gauge factor difference. The response time of the device was 120 ms.

Table 1. Comparison of strain sensing devices.

Material	Morphology	Gauge Factor	Response Time	Reference
ZnO	NW, array	1813		(67)
ZnO	NW, single		500 ms	(68)
GaN	NB, single			(66)
ZnO/Carbon Fiber	NW/fiber	81		(72)
$ZnSnO_3$	NB, single			(73)
ZnO (In doped)	NB, single	4036	120 ms	(69)
ZnO	NW, single	1250	10 ms	(65)
$ZnSnO_3$	NW, single	3740		(74)
Te	NW, single			(71)

NW, nanowire; NB, nano/micro belts/ribbons.

1.5.5 Piezotronic pressure and force sensing

Piezotronic sensors can also be used to detect force and pressure, using the same working principle as for strain sensing. The strain created by an applied force generates piezopotentials which control charge carrier transport at the metal-semiconductor interface. Device fabrication, materials, structure, and characterization are similar for force and strain sensing, and force sensors can be fabricated on rigid or flexible substrates (82, 83). ZnO nanowires are a common choice for force and pressure sensing as well. One key difference between force and strain sensing lies in the application of force. In strain sensing, the bending stress in a flexible substrate is experienced as an axial force along the c-axis of the nanowire. In force sensing applications, axial forces are applied directly along the c-axis of the nanowire (82, 84). Applications for piezotronic force sensors include handwriting recognition, pressures switches, and e-skin (83, 85). Piezotronic force sensors are especially interesting for e-skin applications, as they can achieve higher spatial density and lower force sensing thresholds than mechanoreceptors in human skin (83, 86).

Wu et al. demonstrated a classic example of piezotronic pressure sensing with an array of vertical ZnO nanowires (82). A flexible PET substrate was prepared with an ITO bottom electrode pattern made of Cr/Au/ITO. A ZnO seed layer was deposited and patterned on the electrodes, and arrays of vertical ZnO nanowires were grown on the seed layer. The ZnO nanowires were 30 μm long and patterned into 20 μm x 20 μm taxels. The nanowires were packaged in SU8, and a gold top electrode was deposited to complete the device. A Schottky contact formed between the nanowires and gold, creating an addressable array of Strain Gated Vertical Piezotronic Transistors (SGVPT). The nanowire taxels had a spatial density of 8464 taxels·cm^{-2}, compared to a spatial density of 240 cm^{-2} for mechanoreceptors in a human hand (86). The current output from a single taxel was measured for increasing pressure. The saturation pressure was 30 kPa, and the pressure sensing range of the device was comparable to that of a human finger (87). The sensitivity of the pressure sensor is indicated by the change in carrier transport due to the piezopotential, and was calculated to be 2.1 μS·kPa^{-1}. The response time of the device was measured to be 0.15 seconds. The sensor proved to be useful for handwriting detection, and the imprint of the letter "A" could be resolved by reading the outputs from different channels across the sensor. The device showed a stable output response over 1,000 bending cycles.

The piezotronic effect can also control charge carrier transport in optoelectronic devices, by what is known as the piezo-phototronic effect. Although commonly associated with light emitting diodes (LEDs) and photodetectors, the piezo-phototronic effect has found applications in pressure sensing. Pan et al. created an array of pressure sensing LEDs

by combining ZnO nanowires with GaN (84). An array of single ZnO nanowires with diameters of 1.5 µm and a 4 µm spacing was grown on p-type GaN as seen in figure 15a. A Ni/Au electrode layer was deposited on the back side of the GaN, and the nanowires were packaged with PMMA as shown in figure 15b. ITO was deposited on the exposed nanowires as the top electrode, shown in figure 15c. The device and working mechanism are illustrated in figure 15d and figure 15e, respectively. To test the pressure response of the LED array, the authors created a text stamp out of SU8 that spelled "piezo". The stamp was pressed onto the device with strains varying from -0.06 to -0.015, and the output intensity of the LEDs was measured with a CCD sensor and spectrometer. The measured LED intensity was scaled against the unstressed intensity to calculate a so called enhancement factor, as seen in figure 15f. The average enhancement factor was 2, and the response time of the sensor was 90 ms. A spatial map of the enhancement factors corresponding to the imprint of the "piezo" stamp is shown in figure 15g.

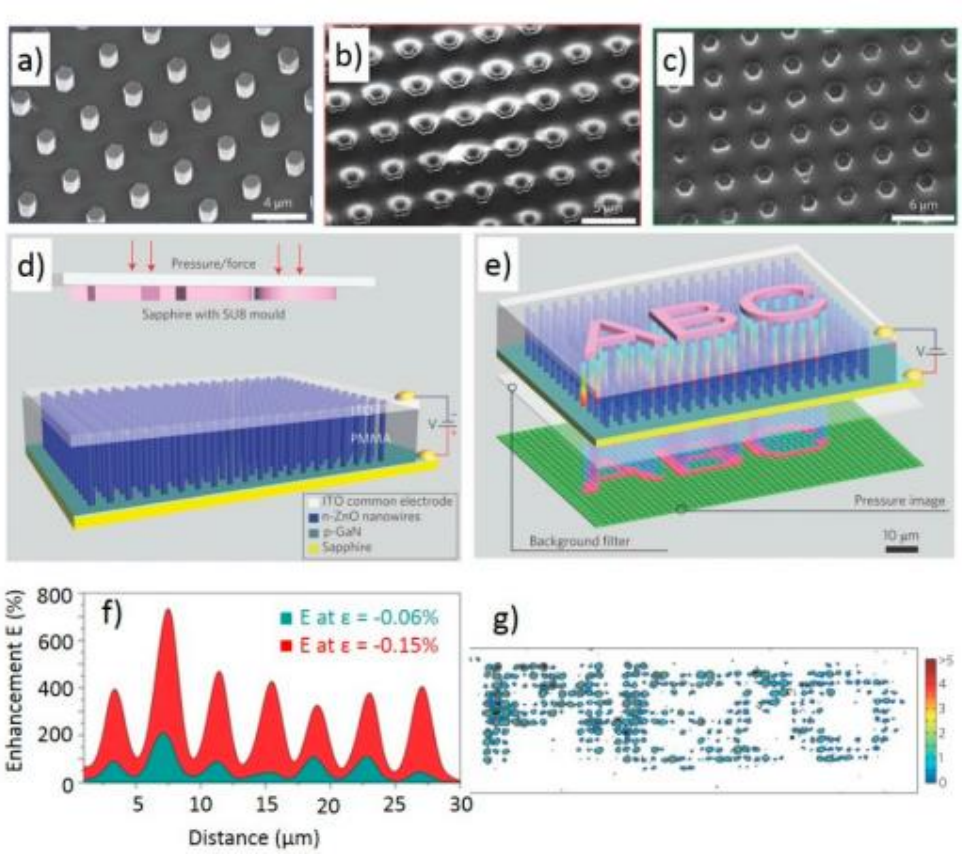

Figure 15. Piezo-phototronic force sensing with ZnO nanowires. (a) SEM images of ZnO nanowire array on GaN substrate. (b) Nanowires encapsulated in PMMA. (c) Deposited ITO electrode. (d) Device schematic and test setup. (e) Resulting image from applied pressure. (f) Enhancement factor for part of an LED row as a function of strain. (g) Spatial map of enhancement factor showing the imprint of a stamp reading "PIEZO". Adapted by permission from Macmillan Publishers Ltd: Nature Photonics (84) Copyright 2013.

GaN has also been used as a transverse force sensor. Zhou et al. used molecular beam epitaxy to create an array of GaN nanowires on a silicon substrate (83). The nanowires were 1.5 µm long and doped with n-type silicon. An AFM cantilever tip was used to apply a bending force to the tip of a single nanowire. The platinum coated AFM

tip formed a Schottky contact with the GaN nanowire, and silver paste was used as the bottom electrode, creating a second Schottky contact.

The band diagram showed how the barrier height changes due to the piezopotential (83). Forces ranging from 104 nN to 312 nN were applied to the nanowire, and the I-V response was measured. The asymmetric I-V response was due to the differences in work functions for silver and platinum, and the response was dominated by the Pt/GaN Schottky contact. The sensitivity of the devices depends on the applied force due to the nonlinear I-V curve. The sensitivity was calculated to be 0.5 pA/nN and 2.0 pA/nN for forces ranging from 16-32 nN and 64-80 nN, respectively. The sensitivity was linearized by ln(I) for simplification. The response time was measured to be less than 5 ms.

Zhou et al. developed a piezotronic trigger sensor which could detect impact forces (85). A single ZnO microwire, approximately 1 mm long, was connected to a Si/SiO_2 substrate with silver paste. The free end of the wire formed a Schottky contact with a gold-coated tungsten needle. Argon gas was blown against the microwire, causing it to vibrate against the needle, simulating an impact force. Impacts were detected by measuring the voltage generated in the nanowire. In a laterally bent microwire, the potential distribution occurs across the diameter of the wire, instead of along the length. Voltage measurements were taken on both the tension and compression sides of the wire. To measure the I-V response, a constant mechanical force was applied to the wire and the current was measured for a bias ranging over ± 2 V.

Piezotronic force sensors have achieved force sensing thresholds as low as 4 nN with a resolution of 0.5 pA/nN (83). Spatial resolutions of 2.7 μm have been demonstrated,

and fatigue resistant, single crystal nanomaterials provided stable sensing for over 1,000 cycles (82, 84). Table 2 provides a summary and comparison of piezotronic force and pressure sensors.

Table 2. Comparison of force and pressure sensing devices.

Material	Morphology	Sensitivity	Spatial Resolution	Response Time	Reference
GaN	NW, single	0.5 – 2 pA/nN		< 5 ms	(83)
ZnO	NW, array	2.1 $\mu S \cdot kPa^{-1}$	100 μm	150 ms	(82)
ZnO	NW, single			10 ms	(85)
ZnO	NW, array	12.88 GPa^{-1}	2.7 μm	90 ms	(84)

NW, nanowire.

1.6 Scope of this Thesis

In essence, piezoelectricity is the transformation of mechanical energy into electrical energy, and vice versa. Piezoelectric materials are the medium for this energy transformation, which can be controlled through the use of various nanomaterials and nanostructures. This thesis seeks to address barriers to the development of new piezoelectric nanomaterial devices for sensing and energy harvesting. Finite element models are developed to gain insight into the behavior of an emerging piezoelectric nanomaterial, and current fabrication techniques are expanded to new substrate materials to realize new device designs. Chapter 1 provides background on the theory of piezoelectricity, and a review of common piezoelectric nanomaterials. Next, the piezotronic effect is introduced, a sensing principle enabled by piezoelectric nanomaterials with semiconducting properties. Chapter 1 concludes with a review of energy harvesting with piezoelectric nanomaterials, followed by a review of piezotronic force and strain sensors.

The contributions of this thesis begin with chapter 2, which explores the piezoelectric behavior of diphenylalanine (FF) peptide, a bio-inspired piezoelectric material, through finite element modeling. A flexible FF peptide nanogenerator is fabricated, demonstrating energy harvesting and validating the predictions of the finite element models. Chapter 3 details the modeling and fabrication of piezotronic force and strain sensors, with a focus on applications for haptics and prosthetic limbs. Using mechanical transfer, CVD synthesis of ZnO nanowires is expanded to soft polymer substrates to create a stretchable piezotronic strain sensor. Chapter 4 is motivated by challenges associated with chemical vapor deposition (CVD), a common technique for piezoelectric nanomaterial synthesis. The design and verification of a new apparatus for CVD synthesis is presented, which can allow for the use of low-temperature substrates in a high-temperature CVD furnace. Finally, chapter 5 provides conclusions and outlook on the future of piezoelectric nanomaterials for sensing and energy harvesting applications.

Chapter 2. Modeling and fabrication of a flexible piezoelectric nanogenerator with diphenylalanine peptide

Mechanical energy can be found in the environment in many forms including wind, water, mechanical vibration, and human movement. By harvesting this energy with nanogenerators, self-powered systems can be realized such as sensors for structural monitoring, environmental measurement, and chemical and biosensing (62, 73, 88-93). Due to their inherent electromechanical coupling, piezoelectric nanomaterials are well-suited for harvesting mechanical energy. Piezoelectric nanogenerators have been successfully developed based on materials such as zinc oxide (ZnO), Poly(vinylidene fluoride-trifluoroethylene) (P(VDF-TrFE)) and monolayer molybdenum disulfide (MoS_2) (3, 16, 59, 60, 94-99).

Due to its biological origins, strong piezoelectricity, and demonstrated ability to self-assemble, diphenylalanine (FF) peptide has received much recent interest. Diphenylalanine peptide is being explored for potential applications for drug delivery, and is also significant for its role as the core recognition motif for Alzheimer's beta amyloid (5, 43). Diphenylalanine-based dipeptides can self-assemble into nanotubes, microrods, hydrogels, and other structures (39-42). Self-assembled FF peptide nanotubes have a hexagonal structure with promising mechanical and piezoelectric properties. Reported elastic modulus values range from 19-27 GPa, which is relatively high among biomaterials (46, 47). The origins of this high stiffness have been explored through first principles (48). Poling can improve the piezoelectric properties of FF peptide, with reported values for the piezoelectric coefficient d_{33} up to 18 pm/V (49, 50). The first use of FF peptide with

controlled polarization for power generation was recently demonstrated on a rigid substrate (44). Due to its promising electromechanical properties, biocompatibility, and low-temperature synthesis method, there is growing interest in FF peptide as a piezoelectric nanomaterial for applications such as energy harvesting.

Despite the potential of FF peptide as a piezoelectric, bio-inspired material, there are still significant barriers to its adoption for device applications. The first barrier is the need for comprehensive finite element models of piezoelectricity in FF peptide structures. First principles and finite element models have provided insight into the mechanical properties of FF peptide microstructures and bulk material (46, 48). However, more work is needed to study the piezoelectric performance of FF peptide compared to conventional piezoelectric materials. Additionally, there is a need to study the complex interactions and piezoelectric response of FF peptide structures as part of a completed device. Design, fabrication, and testing of new devices is complex, costly, and time consuming. Without finite element models, it is difficult to fully predict the piezoelectric response of FF peptide devices, posing a challenge for device design. Finite element modeling has been used to predict the behavior of piezoelectric nanogenerators based on ZnO material (100-102). The development of finite element models for FF peptide nanogenerators can provide insight into the design and optimization of FF peptide devices.

The second barrier to wider use of FF peptide is the need to realize its promising piezoelectric properties in a flexible device. Transitioning from rigid to flexible substrates presents challenges for material synthesis, device fabrication, and characterization. These challenges were overcome to develop a flexible FF peptide nanogenerator. The device was

characterized, and power generation from bending deformation was demonstrated. Characterization of the fabricated nanogenerator successfully validated the predictions of the finite element model. The realization of a flexible FF peptide nanogenerator can help to expand the use of FF peptide to new applications that are inaccessible to rigid substrates, such as wearable devices, flexible electronics, and soft robotics.

2.1 Finite element model of a single nanowire

A 3D model of a single nanowire was created using COMSOL Multiphysics to compare the piezoelectric behavior of FF peptide to conventional piezoelectric materials. The nanowire model was validated against results and geometry from a previous study of piezoelectricity in a ZnO nanowire (16, 103). After validation, the nanowire model dimensions were set to a diameter of 50 nm, and a length of 500 nm. Dimensions were constant for all materials. Electrical and mechanical properties for FF peptide were sourced from computational and experimental literature, and are provided in Table 3. The electrical and mechanical properties for all other materials were taken from the COMSOL Multiphysics standard materials library (104).

Table 3. Electrical and mechanical properties of FF peptide.

Property	Value	Reference
Compliance matrix	$S = \begin{pmatrix} 0.1143 & -0.0627 & -0.0236 & 0 & 0 & 0 \\ & 0.1143 & -0.0236 & 0 & 0 & 0 \\ & & 0.0631 & 0 & 0 & 0 \\ & & & 0.354 & 0 & 0 \\ & sym & & & 0.354 & 0 \\ & & & & & 0.354 \end{pmatrix} \times 10^{-9} \left[\frac{1}{Pa}\right]$	(48)
Piezoelectric coupling matrix	$d = \begin{pmatrix} 0 & 0 & 0 & -10 & 80 & 0 \\ 0 & 0 & 0 & 80 & 10 & 0 \\ 4 & 4 & 18 & 0 & 0 & 0 \end{pmatrix}$ [pm/V]	(49)
Relative permittivity	ε_r = 4.0	(105)

Figure 16 shows the piezoelectric potentials developed in a single FF peptide nanowire compared to the potentials in a single ZnO nanowire. Figure 16a shows the potentials under a compressive load of 10 nN. Figure 16b shows the potentials under a transverse load of 10 nN. In each case, the bottom face of the nanowire was fixed and set to ground potential. The load was applied uniformly to the top surface. The piezoelectric potential developed in the peptide nanowire was about five times higher than for zinc oxide. Under compression, the peptide nanowire developed -1.3 V, compared with -0.26 V for ZnO. Under a transverse force the voltages were ± 0.24 V and ± 0.039 V for FF peptide and ZnO, respectively. The ± indicator is due to the electric potential developing across

the diameter of the nanowire, with opposite signs on the tension and compression sides. For both the FF and ZnO nanowires, the characteristic potential reversal can be seen at the base of the nanowire (16).

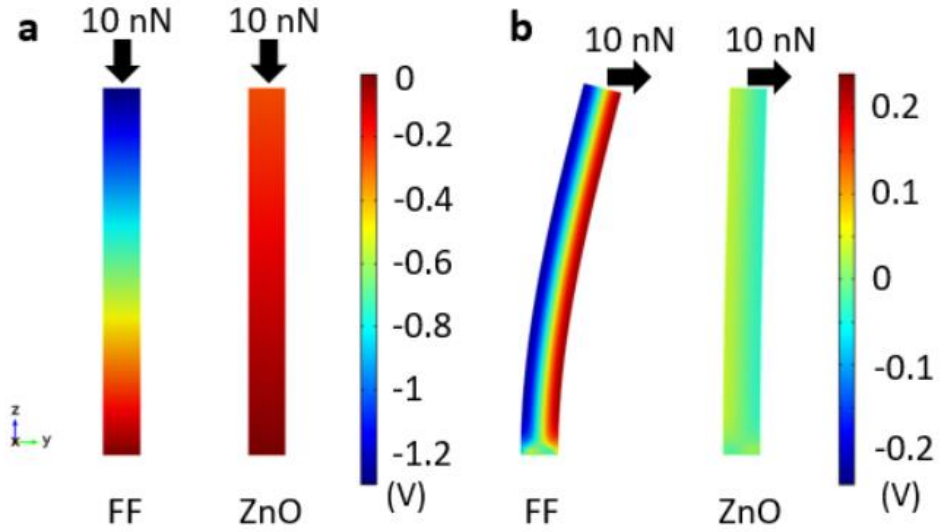

Figure 16. Model of piezoelectric potential in single nanowire. The bottom surface of the nanowire was fixed and electrically grounded. The loads were applied evenly across the top surface of the nanowire. (a) Piezoelectric potential in a y-z plane slice for FF (left) and ZnO (right) nanowires under 10 nN compressive force. (b) Piezoelectric potential in a y-z plane slice for FF (left) and ZnO (right) nanowires under 10 nN transverse force. Nanowire dimensions are 500 nm long by 50 nm diameter. Deformations are to scale.

The single nanowire model was also used to investigate the potential in conventional piezoelectric ceramics, such as lead zirconate titanate (PZT), barium titanate ($BaTiO_3$), and lithium niobate ($LiNbO_3$). The results were compared to the piezoelectric potential created in FF and ZnO nanowires. For a given force and nanowire size, the finite element model showed that FF peptide generated significantly higher potential than any

other materials, under both compressive and transverse loads. A summary of the piezoelectric potentials generated in all materials is presented in table 4.

Table 4. Comparison of simulated piezoelectric potentials in a single nanowire under axial or transverse loading for various materials.

Material	**Voltage (volts)** (10 nN axial force)	**Voltage (volts)** (10 nN transverse force)
FF peptide	-1.3	+ 0.24, - 0.24
ZnO	-0.26	+ 0.039, - 0.039
PZT-2	-0.097	+ 0.012, - 0.013
Barium Titanate	-0.15	+ 0.011, - 0.011
Lithium Niobate	-0.057	+ 0.018, - 0.011

2.2 Finite element model of a 2D flexible nanogenerator

The finite element modeling work was expanded to explore the piezoelectric behavior of FF peptide microrods in a nanogenerator device. COMSOL Multiphysics was used to create a 2D model of a complete FF peptide-based flexible nanogenerator. A schematic of the FF peptide nanogenerator is shown in Figure 17, along with a detailed view of the geometry domains in the model. The device was modeled as a simply-supported beam, with uniform supports and loading across the width of the device (out of the page direction). Therefore the strain and piezoelectricity in the FF microrod array was also assumed to be uniform across the width of the device. Furthermore, the hexagonal FF peptide microrods are transversely isotropic. These assumptions allowed for the use of a 2D model, which greatly reduced the required computational time and simulation complexity. A 3D model of the nanogenerator substrate confirmed that the strain distribution was in fact uniform across the width of the device.

The model geometry was constructed from a series of rectangular domains. The PI peptide growth substrate was represented by a 12 mm long and 0.25 mm tall rectangle. Based on measurements of the SEM image in figure 20b, the peptide microrods were modeled as 50 μm long by 7 μm wide rectangles. The microrods were placed directly on top of the PI growth substrate in a row with a spacing of 40 μm. A rectangle layer with a size of 12 mm long by 75 μm tall was placed on top of the growth substrate, overlapping the microrods. This rectangle represented the PDMS layer in which the microrods were embedded. The gold electrode layers were omitted from the simulation due to their negligible thickness (100 nm). The nanogenerator model was placed on top of a 30 mm long by 0.25 mm tall PET rectangle. The PET surface represented an example of a typical flexible application. Mechanical properties for PDMS, PET, and PI were taken from the COMSOL material library. For this simulation, PDMS, PET, and PI were modeled as linear elastic materials, and linear elasticity was assumed for the model physics. The d_{33} direction for the piezoelectric material was aligned with the +y direction in the simulation. A distributed load was applied to a portion of the top surface of the nanogenerator, resulting in a 3.5 mm displacement at the center.

The nanogenerator model and corresponding geometry domains are shown in figure 17a. The mechanical and electrical boundary conditions used for the model are shown in figure 17b. The nanogenerator on a flexible PET surface was modeled as a simply-supported beam, with a pin at x = 6 mm, and a roller at x = 24 mm. The pin was modeled as a fixed displacement in both the x and y directions, while the roller was modeled as a fixed displacement in the y direction only. A uniform distributed load of 32 kPa was

applied to a 3 mm section at the center of the nanogenerator. The 3 mm length was selected because it is the approximate contact length of the push rod used to apply displacements. The applied load was chosen to create a displacement of 3.5 mm at the center of the device. The distributed load was found to create more realistic deformations in the contact area of the model compared to using a prescribed displacement. Figure 17b shows the electrical boundary conditions for the microrods, which were set to ground potential on the bottom surface. Figure 17c shows an example of the mesh near the FF microrods.

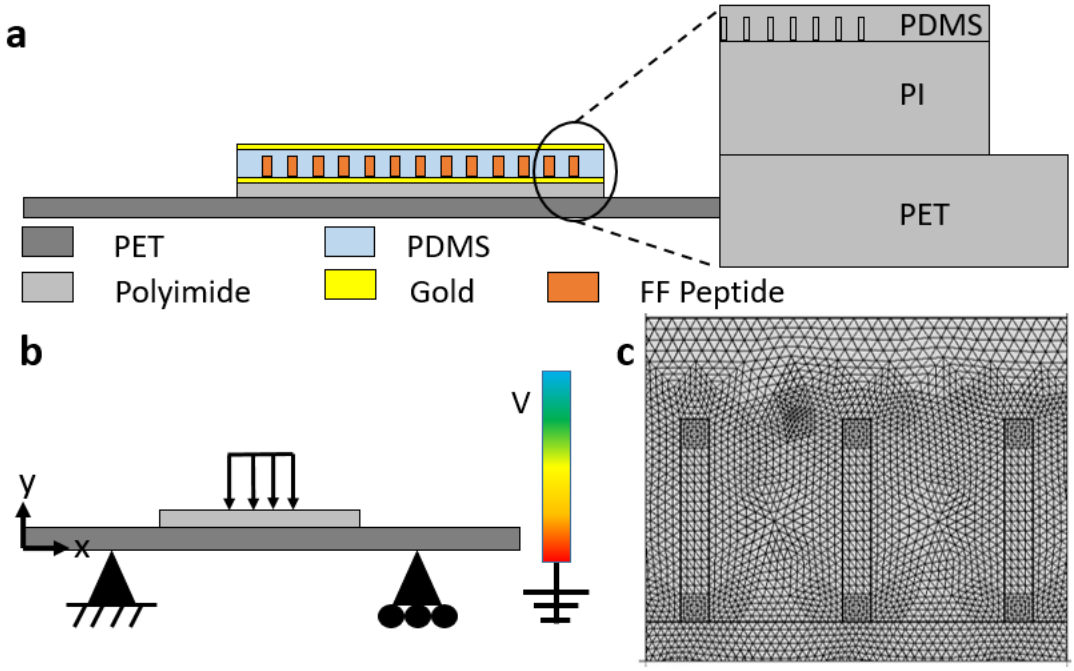

Figure 17. COMSOL Multiphysics model of 2D FF peptide nanogenerator. (a) Illustration of FF nanogenerator and corresponding geometry domains in the finite element model. (b) Mechanical and electrical boundary conditions for the nanogenerator and piezoelectric FF peptide microrods. (c) Sample of mesh in the region of the FF peptide microrods.

Figure 18a shows the initial state of the nanogenerator, and the bending stresses in the deformed state. Discontinuities in the stress distribution can be seen due to the different elastic moduli in the PET, PI, and PDMS layers as shown in figure 18b. The maximum and minimum stresses in the beam were 27.3 MPa and -92.2 MPa, respectively. The strain, shown in figure 18c, was continuous between the layers, as expected. With the exception of localized stress concentrators, the strains were generally within ~2 %, confirming that the device could be modeled using linear elasticity.

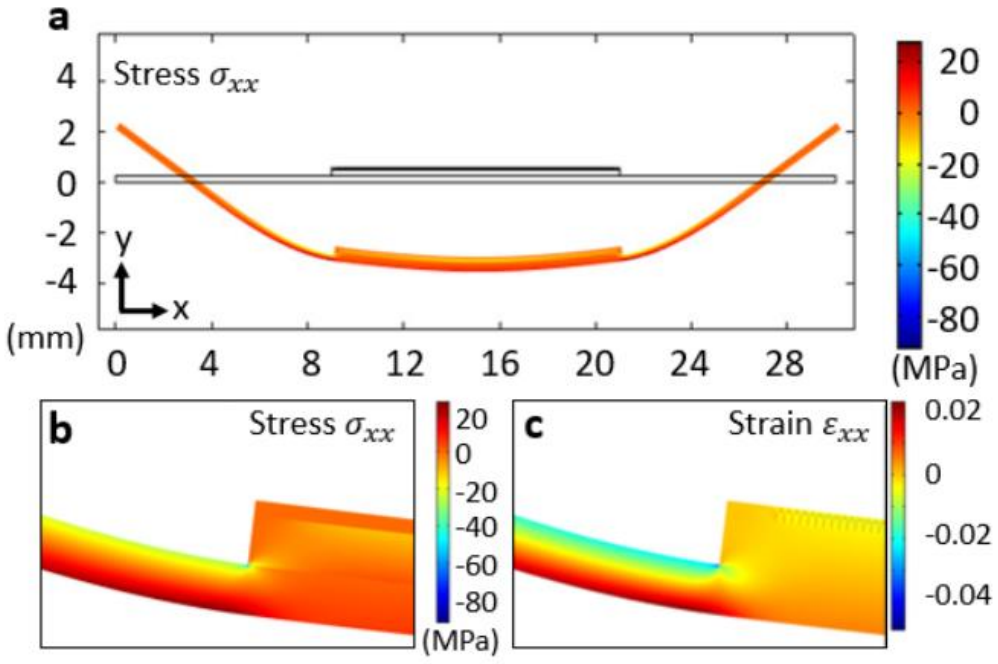

Figure 18. Stress and strain in 2D model of FF peptide nanogenerator. A 32 kPa distributed load was applied in the middle of the nanogenerator, producing a maximum deflection of 3.5 mm. (a) Stress tensor xx component in the nanogenerator showing the initial and deformed state. (b) Detailed view of the xx component of the stress tensor across the material boundaries. (c) Detailed view of the strain tensor xx component across the material boundaries.

Figure 19 shows the piezoelectric potential in the FF microrods under a 3.5 mm deflection, as a function of their position on the nanogenerator. The bottom surfaces of the microrods were grounded. The electric potential was measured at the top of each microrod and plotted in figure 19a. The electric potential in the microrod is shown on the vertical axis, and the horizontal axis is the location of the microrod on the nanogenerator. The electric potential was measured at a point in the center of the top surface of each microrod. In reality, the potential across the top surface of each microrod was slightly non-uniform in the simulation, due to the complex strain state. For an individual microrod, the variation in potential across the top surface was approximately 0.1 V or less.

Figure 19a shows that the microrods in the nanogenerator can be divided into three regions based on electric potential. Region II is in the middle of the nanogenerator, under the distributed load. Region I and III are towards the outside edges of the nanogenerator where no distributed load was applied. Due to device symmetry, Region I and Region III have similar electric potentials. In Region I and Region III, the piezoelectric potential in the microrods decreases slowly towards the center of the nanogenerator, from about -0.2 V to about -0.3 V. At the boundaries with Region II, the piezoelectric potential rapidly drops to -1.6 V. Figure 19b shows the piezoelectric potential distribution in a group of microrods in Region I, at x = 11 mm. Figure 19c shows the potential in a group of microrods in Region II, at x = 15 mm. Overall, the displacement of the nanogenerator creates an electric potential distribution along the length of the microrods in figure 19b and figure 19c. However, a complex potential distribution exists near the root of the microrods. The complex strain and potential near the root area is likely caused by the interface between

three different materials, the PI substrate, the FF microrods, and the PDMS encapsulation layer. A more detailed view of the stress, strain, and potential at this interface location is provided in the appendix, in figure A1 and figure A2.

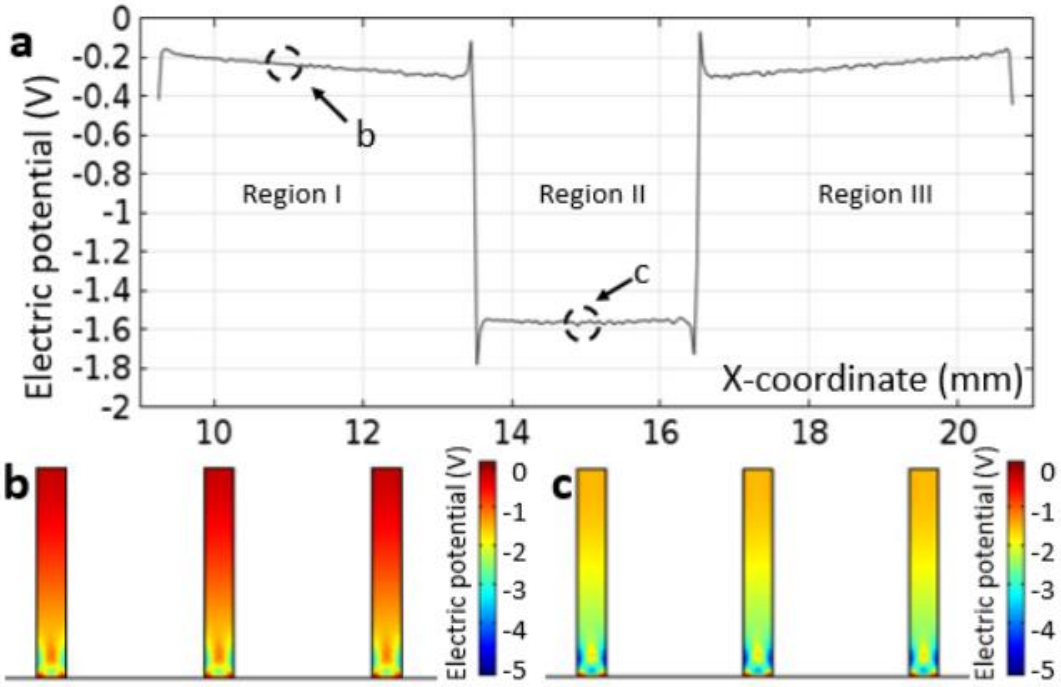

Figure 19. Microrod electric potential in 2D model of FF peptide nanogenerator. (a) Electric potential at the top surface of each FF microrod as a function of position on the deformed nanogenerator. Electric potential in several microrods from (b) Region I and (c) Region II.

2.3 Fabrication and testing of a flexible nanogenerator[1]

To validate the finite element models of the FF peptide and nanogenerator, a flexible FF peptide nanogenerator was fabricated. The measured electrical output was compared with the finite element model predictions. Figure 20a shows a schematic of the

[1] Portions of the device fabrication and testing were performed by Steve Kelly.

fabricated nanogenerator. The fabricated device has the same structure and dimensions as the finite element model in figure 17. Arrays of vertical FF peptide microrods with controlled polarization were grown on flexible, gold-coated PI substrates using a low temperature synthesis method (44, 50). Polyimide film squares (DuPont Kapton) were laser cut with dimensions of 12 mm long x 12 mm wide x 0.25 mm thick to serve as flexible growth substrates for the FF peptide microrods. Sputtering was used to deposit a 5 nm thick chromium (Cr) adhesion layer followed by a 100 nm thick gold (Au) electrode layer. The synthesis method for the growth of FF peptide microrods is discussed in detail in (50), and the growth of vertical FF microrod arrays on the flexible PI substrates is briefly summarized here. A solution of FF peptide powder (Bachem) was dissolved in Hexafluoroisopropanol (HFP) and dropped onto the PI substrates in a vacuum chamber. The chamber was then evacuated and purged with dry air, which resulted in the formation of amorphous FF peptide seed layers. Next, the substrates were placed between two parallel aluminum plates in a chamber with controlled humidity. The substrates were subjected to a uniform electric field by applying 5 kV to the parallel plates. Meanwhile, 100 % relative humidity (RH) air was circulated across the substrates for 60 seconds. This process crystallized the amorphous seed layers. During this process, the PI substrates were affixed between the two parallel aluminum plates with a non-conductive tape. Previously, a conductive carbon tape was used to mount rigid silicon substrates between the poling plates (44, 50). Replacing the conductive tape with the non-conductive tape resulted in a more uniform seed layer on the insulating PI substrates. Further investigation is needed to determine the reason for this improvement. Finally, the substrates with crystallized seed

layers were floated face-down in a 5 ml solution of FF peptide dissolved in water. The substrates were left in the solution for 6 hours at 55 °C. During this time, the substrates were again poled under a uniform electric field between two parallel aluminum plates with a voltage of 8.5 kV.

The substrates with FF peptide microrod arrays were spin-coated with PDMS (Slygaard 184) at 4,000 RPM for 2 minutes, and cured. Next, a top electrode layer was sputtered on the PDMS consisting of a 5 nm thick Cr adhesion layer and a 100 nm thick Au layer. The completed FF peptide nanogenerator was attached to a 30 mm long x 12 mm wide x 0.25 mm thick layer of PET for testing.

SEM imaging of the peptide growth showed an array of peptide microstructures that can be seen in the inset of figure 20b. The microrods in the SEM image were approximately 50 μm long by 7 μm in diameter. Figure 20b shows a picture of the completed FF nanogenerator device. The nanogenerator was attached to a long, thin piece of PET which represents a flexible surface that the nanogenerator could be attached to.

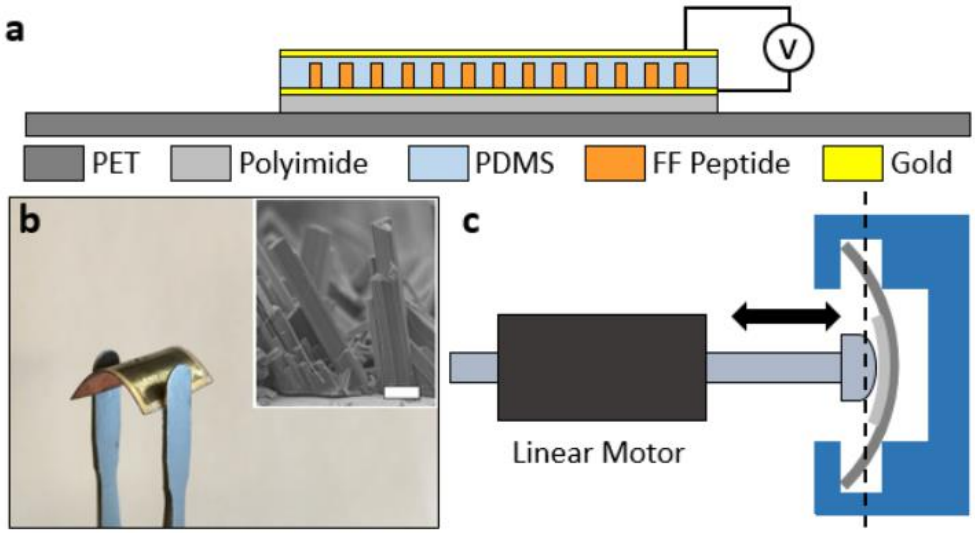

Figure 20. Design, fabrication, and testing of FF peptide flexible nanogenerator. (a) Illustration of FF peptide nanogenerator attached to a PET beam. (b) Image of FF peptide nanogenerator showing the flexible polyimide substrate. Inset shows SEM image of peptide microrods. Scale bar is 10 μm. (c) Test fixture schematic shows nanogenerator and PET beam with periodic displacement applied by a linear motor.

The electrical response and power generation of the flexible FF peptide nanogenerator were characterized during periodic bending deformation. The PET beam with attached nanogenerator was placed in a fixture that approximated the simply-supported boundary conditions as seen in Figure 20c. A periodic displacement of 3.5 mm was applied to the center of the nanogenerator using a linear motor. The displacement was applied and released periodically, at 1 second intervals, and was applied evenly across the width of the device. A schematic of the experimental setup is shown in figure 20c.

Electrical characterization of the nanogenerator under periodic displacement measured an open-circuit voltage up to -0.6 V and a short-circuit current up to 7 nA. The

open-circuit voltage of a nanogenerator remained constant as shown in figure 21a, which is attributed to the good dielectric property and negligible leakage current of FF peptide. The short-circuit current of the nanogenerator is shown in figure 21b. Testing was repeated with reversed connections and the outputs were reversed accordingly. This result confirms that the measured signal was in fact from the piezoelectric FF peptide instead of variations in contact resistance or parasitic capacitance. The power output was calculated as a function of external load resistance, and the result is shown in figure 21c. The maximum power output was calculated to be 0.375 nW based on a peak current of 2.5 nA, and a load resistance of 60 MΩ. The good performance of the flexible peptide nanogenerator can be attributed to the high piezoelectric coefficients and low relative permittivity of FF peptide. The open-circuit voltage of the FF peptide nanogenerator exceeded that of other flexible piezoelectric nanogenerators based on ZnO (106), monolayer MoS_2 (3, 107), PVDF (108), and other biological materials such as bacteriophages (109).

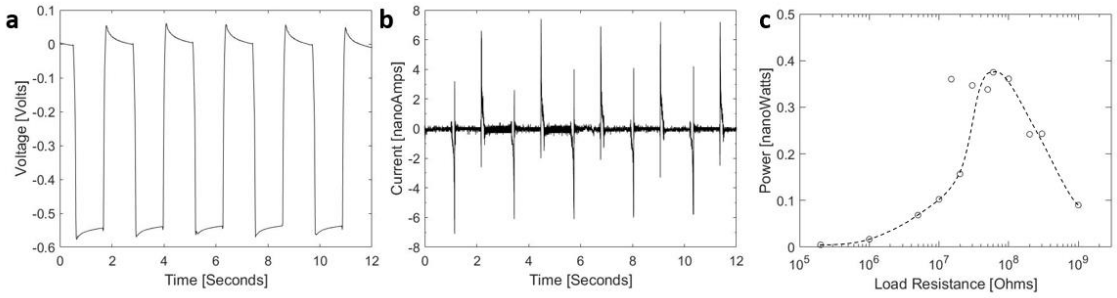

Figure 21. Characterization of FF peptide flexible nanogenerator. (a) Open-circuit voltage (V_{oc}) and (b) short-circuit current (I_{sc}) for the peptide nanogenerator under 3.5 mm periodic displacement. (c) Power output calculated for external load resistances ranging from 200 kΩ to 1,000 MΩ.

The flexible nanogenerator consisting of FF microrods and the adjacent polymer matrix can be modeled as a capacitor-type device. The capacitance of the device is the sum of the capacitance for the microrods and the capacitance for the PDMS matrix. The total charges, on the other hand, are contributed solely by the piezoelectric microrods. Based on SEM images, the volume fraction of vertical FF microrods can be estimated to be 25-33 %. For calculation purposes, the volume fraction was assumed to be 30 %. The main contribution was assumed to be from the microrods in Region II, and the piezoelectric potential of the microrods was taken to be -1.6 V from the finite element analysis. Based on these values, it was estimated that the nanogenerator would produce a V_{oc} of approximately -0.61 V, which was consistent with the experimental measurement of -0.6 V. The close agreement between the simulation and measured device output confirms the validity of the model. This result demonstrates the importance and significance of developing finite element models for the design and optimization of FF peptide devices.

2.4 Chapter summary

Finite element models were used to study the piezoelectric potential in FF peptide. For a given force, the piezoelectric potential in a single nanowire model was found to be higher for FF peptide than for conventional piezoelectric materials such as ZnO, PZT, $BaTiO_3$, and $LiNbO_3$. The finite element analysis was expanded to create a 2D model of a flexible nanogenerator based on FF peptide microrods. To validate the model predictions, the first flexible FF peptide nanogenerator with vertical microrods was fabricated. The nanogenerator was tested, and successfully harvested mechanical energy from bending deformation. The electrical output of the fabricated device was characterized and the

results successfully validated the finite element model of the nanogenerator. The expansion of FF peptide growth to flexible substrates opens the way for new applications including wearable devices and flexible electronics. Finite element models can provide insight into the design and optimization of a new generation of flexible FF peptide devices.

Chapter 3. Modeling and fabrication of piezotronic force and strain sensors

3.1 Tactile sensing for haptics and prosthetic limbs

There were 1.6 million amputees in the United States alone as of 2005, with the number projected to double by 2050 (110). There are many types of upper limb prostheses available. The choices of whether or not to use a prosthesis, and what type of device to use, are highly individual decisions, and there is no correct answer. For some individuals, however, the incorporation of sensory feedback into prosthetic limbs can be beneficial. It has been estimated that 20 % of eligible users decide not to use a prosthetic device, and lack of sensory feedback is cited as a major reason. Recent trials have demonstrated increased prosthesis utility with the incorporation of sensory feedback. However, incorporation of sensory input exists in only a relatively small number of trials, which often rely on invasive peripheral nervous system interfaces (111, 112). There has been significant work to develop sensors for so called electronic skin (e-skin) that can replicate human touch perception (113).

The goal of this work is to purpose-design a tactile sensor for haptics and prosthetics applications. The sensor will be intended for use with a sensory substitution system for upper limb prostheses. While sensory substitution systems already exists, they often rely on off-the-shelf sensors which are not optimized for this application (114, 115).

Current state of the art upper limb prostheses allow users to exhibit voluntary motor control of the device, but there are limited options for providing sensory feedback. Several works show that implementation of sensory feedback greatly improves closed-loop control

of prosthetic devices, which currently is limited to visual feedback (111, 112). At present, several research trials have demonstrated success in connecting off-the-shelf sensors to the peripheral nerves in the arm (112). These trials rely on invasive surgical interface technologies such as cuff electrodes and are limited to pressure or force sensing (112). Results of these trials have been promising, showing increased prosthesis functionality and addressing problems such as phantom limb pain. Furthermore, these trials have been conducted for extended periods of up to 24 months (111).

Current state of the art sensors can exceed the spatial density of the human mechanoreceptor system and provide sensing within physiological force ranges. However, the large amounts of data generated by such sensors are difficult to incorporate into the peripheral nervous system (84, 112). Machine learning classifiers have found use in robotics to transform complex inputs from high-resolution sensors into discrete outputs (116). These concepts are applicable to the development of vibrotactile (VT) interfaces, which belong to a growing body of noninvasive haptic stimulation literature including mechanotactile and surface electrical stimulation (114, 117).

While current developments are very promising and show a strong interest in this field, there are many opportunities to develop purpose-designed sensors. Just as the choice of prosthesis type varies by user needs, the preferred type of sensory input may also be user dependent. Piezotronic force and strain sensors are well-suited for replicating human tactile perception, due to their high sensitivity and high spatial resolution.

The ability to reliably grasp objects is an important feature for many upper limb prosthesis designs. Controlling the grasp force on an object is important not only to avoid

damaging the object, but also for preventing object slip. Grasp force control in prosthetic hands is a complex problem involving sensor design, feedback control, and machine learning (118). Although shear force sensors can detect object slip, most work has been focused on the development of controllers and algorithms for slip detection. A wide variety of slip detection approaches and sensor architectures have been studied, but no clear metric exists for sensor performance in grasping applications. There is a need to continue developing sensors and methods to improve grasping with prosthetic hands for preventing object slip.

This chapter begins with the design of a piezotronic sensor architecture that can detect physiological force ranges for both normal and shear contact forces. The requirements for the tactile sensor are informed by the tactile sensing capabilities of human touch physiology. These aspects include force, form, texture, and curvature (shape) (119). The human somatosensory system contains 4 distinct neuronal structures called mechanoreceptors. The mechanoreceptors are classified based on their response as rapidly adapting (RA) or slowly adapting (SA). RA receptors respond transiently to forces on the skin while SA receptors respond for the entire duration of the applied force. The RA receptor types are the Meissner (RA type I) and Pacinian corpuscles (RA type II). The SA receptor types are the Merkel disks (SA type I) and Ruffini endings (SA type II) (120). The Pacinian corpuscles are sensitive to vibration and pressure while the Meissner corpuscles sense light touch. The Merkel disks also detect vibration and pressure, and the Ruffini endings are sensitive to skin stretch. Additionally, each type of structure has a differently sized receptive field and varying spatial density, which is generally highest in

the hand (121). Using single unit recordings and the von Frey hair test method, the median force sensing thresholds for human mechanoreceptors were found to be 0.58 mN and 0.54 mN for RA I and RA II types and 1.3 mN and 7.5 mN for SA I and SA II types, respectively (122). For texture sensitivity, it has been reported that the human hand can detect textures at the nanoscale (123).

The literature presents two general approaches to tactile sensor design. The first group consists of conventional MEMS, and includes piezoresistive, capacitive, and optoelectric sensors. The second group involves hybrid biological devices (124). Within the two groups, the biggest differentiators are fabrication cost, resolution, and number of sensing modes (e.g. shear and normal force).

The majority of devices reviewed here are conventional, and within this group most are capacitive. A micro-machined capacitive device with floating electrodes is presented by Cheng, et al. The device is simple and economical with resolution as low as 38 mN (125). Using microfluidics and capacitive sensing, a flexible, normal force sensor with 5 mm spatial resolution is demonstrated (126). Other capacitive sensor designs exhibit multimodal sensing to detect shear and normal forces, however the range is limited to 10 mN (127). Sub-mN detection of surface textures is demonstrated by a silicon based capacitive device (125).

Another fundamental principle of sensing is the piezoresistive effect. Such devices include a biomimetic sensor with a silicon beam and membrane to detect shear and normal forces for surgical applications (128). A novel method to increase the sensitivity of

piezoresistive devices is demonstrated in a sensor that can measure forces and detect simple shapes (129).

The last sensor category is hybrid biological sensors. The sensors described here merge electronics with tissue engineering to create novel sensors. One such sensor consists of a sub-mN resolution silicon MEMS device successfully embedded into tissue-engineered skin (130). In cases where tissue innervation is lost, for example due to burn injuries, this device could be useful for restoring touch sensation. Lastly, a biomimetic, tissue-engineered tactile sensor which can detect normal and shear forces is presented. The device is multimodal, being also sensitive to temperature changes, thereby replicating physiological thermoreceptors (131). While interesting for their high biocompatibility, hybrid biological devices face significant challenges in regards to practical incorporation with human tissue.

Amputations are performed for many different reasons, including complications from diabetes, dysvascular disease, cancer, and trauma (110). The surgery and outcome is highly specific to the individual. It is important to understand the underlying physiological changes that occur following an amputation. Based on current understanding, the evidence supports attempts to restore sensory feedback as both feasible and beneficial.

There are many complications and changes to the central and peripheral nervous system following amputation, including changes in stump nerves (132). Cortical remapping, a reorganization of the central nervous system (CNS) resulting in increased sensory and motor representation of adjacent skin and muscles in the motor cortex, is also

thought to occur (133, 134). Phantom limb pain is a common occurance, which can be mitigated with the restoration of sensory feedback (135).

While these CNS changes can cause problems, they are also the basis for restablishing sensory input to the brain. Some activity related to missing limb movement remains. Incomplete reorganization of the cortex leads to phantom limb pain (136). However, this residual limb activity is the basis for reestablishing control of a prosthetic hand (137).

Several trials in the literature have explored the effects of attaching tactile sensors directly to the peripheral nervous system. These trials demonstrate the feasibility and illustrate some of the practical challenges with this area of research. A study by Tan et al. demonstrated a long term invasive peripheral nerve interface in two human subjects. The interface used a cuff electrode and was shown to be stable for 16 and 24 months, respectively, in the two subjects (111). In this study, patients were delivered stimuli that were perceived as “natural”, without a sense of parasthesia, an uncomfortable tingling sensation. Various stimulation parameters were explored, with intensity being shown to affect the size of the area of perception. Stimulation frequency was also shown to be directly proportional to the perceived intensity. Task specfic trials such as de-stemming a cherry showed improved control over a myoelectric prosthesis, and a reduction in phantom limb pain was noted.

In a trial by Raspopovic et al., a sensory feedback system was connected to the median and ulnar nerves of an upper limb amputee and linked with two sensors on a

prosthetic hand. This bidirectional interface used muscle signals to drive the grasping motion of the hand. When blindfolded, the subject was able to differentiate the stiffness of objects such as cotton balls and oranges (112).

3.2 Design and modeling of a piezotronic contact force sensor

A contact force sensor was designed to independently detect shear and normal force components at thresholds meeting or exceeding that of human mechanoreceptors. The sensor was designed to detect shear and normal forces, because they can play an important role in prosthetics and haptics applications such as grasping. The contact force sensor design is based on beam theory. The device design consists of two pillars of nanowires as shown in figure 22, each forming a separate channel. The nanowires are embedded in a polymer, such as PDMS. For the piezotronic device to function, the nanowires need to develop electric potential along their lengths, between the top and bottom electrodes. Under a lateral force, a single nanowire will develop electric potential across the diameter, and not along the length, as shown in figure 22a. By arranging the nanowires in a beam configuration, the nanowires and PDMS act as a beam, as illustrated in figure 22b. The beam is symmetric, and the neutral axis is located in the center, between the two pillars of nanowires. When a lateral force or deflection is applied, the beam bends. The strain at the neutral axis is zero. On one side of the neutral axis, the beam experiences tensile strain along the length of the beam. On the other side of the neutral axis, the beam experiences compressive strain. This causes the nanowires to experience either tension or compression along their lengths. Consequently, electric potential develops along the length

of the nanowires even though the beam structure is experiencing a lateral deflection as seen in figure 22c.

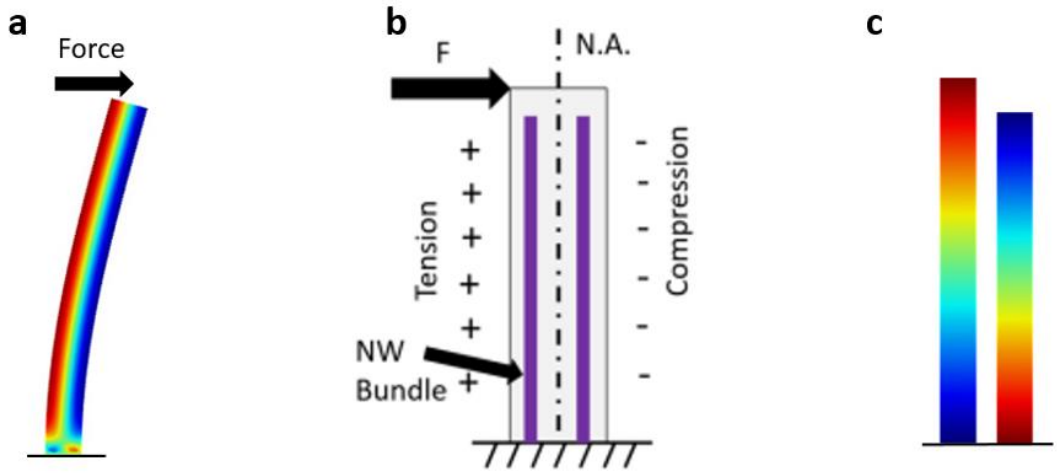

Figure 22. Working principle of piezotronic shear and normal force sensor. (a) Shear force on a single nanowire creates a complex potential across the diameter. (b) Proposed beam configuration of ZnO nanowires on either side of the neutral axis. (c) Shear force creates tension or compression in nanowires arranged in a beam configuration, resulting in potential along the length of the nanowires.

The proposed sensor can also detect normal forces in addition to shear forces. An applied normal force causes the nanowires to stretch or compress along the c-axis, and naturally results in electric potential along the length of the nanowires. The magnitude of the electric potential depends on the amount of force applied. This is the mechanism by which the sensor can detect normal force.

Figure 23 shows a finite element model of the contact force sensor under different loading conditions. Figure 23a shows the electric potential under a 100 nN compressive force, and figure 23b shows the electric potential under a 100 nN transverse force. Figure 23c shows the electric potential under an oblique force which consists of a 100 nN normal

component, and a 100 nN transverse component. In all cases the bottom face of the nanowire was set to ground potential, and the force was applied evenly to the top surface of the sensor. In each loading case, a unique potential distribution is created in the nanowires. The different potential distributions will result in different changes in conductivity for each channel. The result suggests that the sensor will be able to distinguish between the three different loading conditions. Furthermore, the signals from the normal and transverse force components can be separated and extracted from the sensor. The normal force component corresponds to the average of the two channels, and the shear force component corresponds to the difference between the two channels.

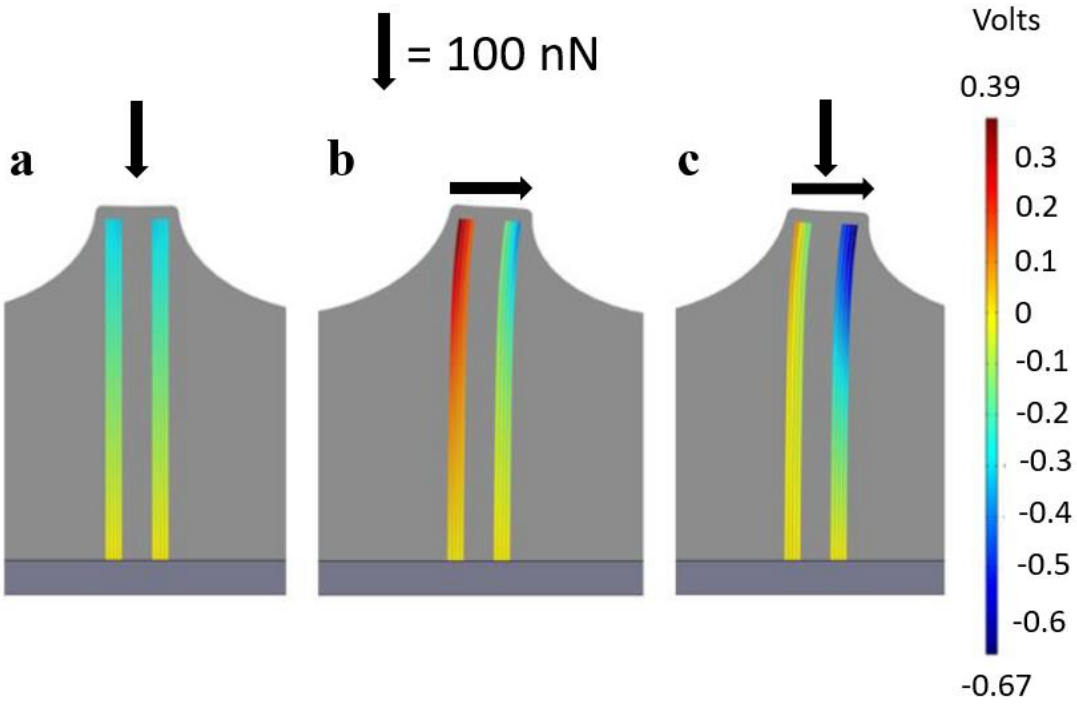

Figure 23. Simulation of piezopotential in ZnO contact force sensor. (a) Piezoelectric potential under 100 nN compressive force, (b) 100 nN transverse force, and (c) oblique force with 100 nN components in normal and transverse directions.

The sensor can be expanded to measure shear force in two dimensions by creating a 2 x 2 array of nanowire pillars (4 channels). Multiple 2 x 2 arrays can be created across the surface of the sensor to provide sensing at a high spatial resolution. The electric potentials created in the sensor under a 100 nN load are sufficient to generate measureable signals, suggesting that the force detection threshold can be lower than that of a human mechanoreceptor. Preliminary fabrication and testing results for the contact force sensor are shown in the appendix in figure A3 and figure A4.

The application of the sensor for object slip prevention is envisioned in figure 24a. The sensor is affixed to the finger of a prosthetic hand. The hand grasps a cup which is being filled with water. The sensor detects the grasping force, which is the normal force component, and the shear force, which corresponds to the weight of the cup. As the cup is filled with water, the weight increases, along with the shear force measured by the sensor. The grasping force of the hand is maintained by a closed-loop feedback controller. PD controllers have been used for grasp force control, and reflect natural human force sensing, which can detect magnitude and rate of force change (138, 139). The set-point for the controller is the ratio of shear to normal force. A small margin may be added to this ratio for safety. As the weight of the cup increases, the shear force increases, and the controller will increase the normal (grasping) force to maintain the ratio. Using the ratio of shear to normal force also has the benefit of reducing the system to a single input. The increasing weight of the cup can be generalized to any external disturbance of the object, which normal force sensing alone cannot account for during object slip control. The finite element model indicates that the proposed sensor can detect shear and normal forces on the

order of 100 nN, which is lower than the 0.01 N threshold for sensors previously demonstrated in slip detection applications (140).

Figure 24b illustrates another potential advantage of the shear force sensing capability. A prosthetic hand with the sensor attached to the finger moves across a curved surface. With normal force sensing only (top), there is only one component of the force vector to provide information about the curvature of the surface. With normal and shear force sensing (bottom), the measured force can be resolved into two components, potentially providing more information about the surface. It is hypothesized that the addition of the shear force information would result in lower detection and discrimination thresholds for curvature changes, compared to normal-only force sensing.

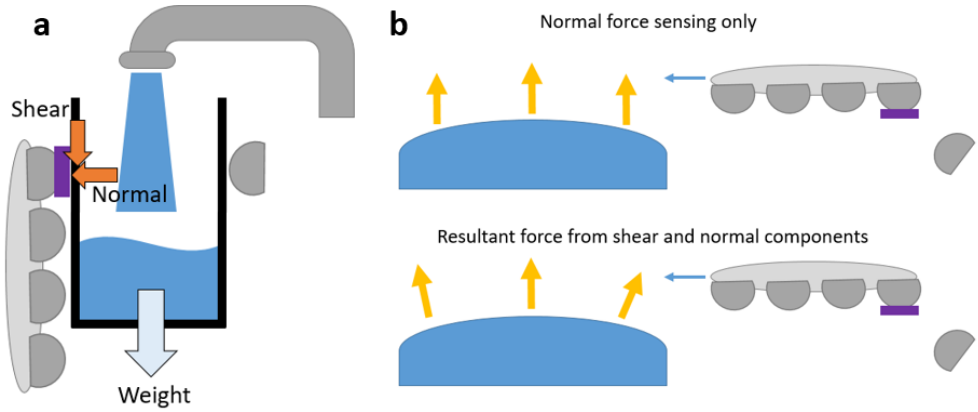

Figure 24. Applications for piezotronic contact force sensor. (a) Object slip prevention with a shear and normal force sensor. The figure depicts a proposed realization of the shear and normal force sensor for slip prevention. The sensor is attached to a prosthetic hand which grasps a cup as it is filled with water. The increasing weight causes an increase in measured shear force, which signals a feedback controller to increase the normal grasping force. (b) Extracting force components during curvature exploration from normal force sensor (top) and combined shear and normal force sensor (bottom).

3.3 Design and fabrication of a stretchable piezotronic strain sensor

Strain gauges are an essential tool for modern engineering, with uses including structural monitoring and mechanical testing. Conventional strain gauges are made from metal film and are resistive devices. For conventional strain gauges, the operating principle is the change in resistance due to applied strain.

The substrate for a typical strain gauge is PET, a flexible polymer with an elastic modulus of about 3 GPa. Human skin, by comparison, has a modulus of less than 1 MPa, (141, 142). The modulus of PDMS is on the order of 1-3 MPa, much closer to that of human skin. A stretchable strain sensor with mechanical properties similar to human skin could replicate the function of the *Ruffini ending* mechanoreceptors, which can detect skin stretch. A stretchable strain sensor could also see applications in flexible electronics, wearable devices, and soft robotics.

A new class of strain gauges is emerging based on nanomaterials such as ZnO nanowires, which operate based on the piezotronic effect. The advantages of piezotronic, nanomaterial-based sensors include high sensitivity and fast response times (65, 66, 68, 69, 72-74). The basis of piezotronic strain sensors is a metal-semiconductor interface. The semiconductor material is also piezoelectric, and develops an electric potential under applied strain. A bias voltage drives current across the device. The metal-semiconductor interface creates a Schottky barrier. The piezopotential due to the strain modifies the barrier height, thereby controlling conductivity at the metal-semiconductor interface. This is known as the piezotronic effect (56).

ZnO nanowires are commonly used for piezotronic devices, and can be synthesized using hydrothermal methods, or by chemical vapor deposition (77, 143). The advantages of hydrothermal synthesis include scalability, and low process temperature (< 100 ºC) which is compatible with polymer substrates and photolithography patterning. On the other hand, CVD can produce longer, higher quality nanowires, but silicon substrates are typically used as the high temperatures are not compatible with polymer substrates.

A method for mechanically transferring CVD grown ZnO nanowires was designed to create a stretchable, conformal piezotronic strain sensor (144). The purpose of the mechanical transfer process was to remove the ZnO nanowires from the rigid CVD growth substrate, while simultaneously creating a new stretchable substrate. One common method for mechanically removing nanowires from a substrate is to infiltrate the nanowires with a polymer such as PDMS. The cured PDMS is then peeled away from the substrate along with the nanowires (145). The transfer process can be optimized by changing the viscosity of the PDMS, and the process works for different materials, such as silicon and gallium phosphide (146). Mechanical transfer is possible by other processes, such as roll-transfer printing, and has been used to fabricate ZnO nanowire FETs and silicon nanowire electronic devices (147, 148). Many nanowire devices already use polymer infiltration to protect the nanowire arrays, so mechanical transfer is a logical extension of the device fabrication process (67, 82).

PET is a commonly used substrate for flexible electronics, however the relatively high elastic modulus makes it difficult to conform to complex surfaces. By comparison, PDMS has a relatively low elastic modulus of only a few megapascals. The mechanical

transfer process allows for the use of high quality, CVD grown ZnO nanowires in a stretchable, conformal device.

Figure 25 shows the device fabrication steps for the strain sensor. Vertical, well-aligned ZnO nanowires were grown on a silicon substrate as seen in Figure 25a. First, a 5 nm thick Cr adhesion layer was sputtered on a silicon wafer followed by a 100 nm thick ZnO seed layer. The wafer was diced into 5 mm x 20 mm substrates. To improve the alignment of the ZnO nanowires grown by CVD, a second seed layer was grown using a hydrothermal recipe developed by Zhu, et al. (77). This second seed layer consists of a so called textured film, which is a semi-merged layer of short ZnO nanowires a few microns in length. The textured film layer was grown in a solution containing 175 mM Zinc Nitrate and 175 mM HMTA. Substrates were floated on top of the solution with the sputtered seed layer face down, in a convection oven for 6 hours at 95 ^{o}C. Next, ZnO nanowires were grown on the textured film seed layer using CVD. A ceramic crucible was prepared with 600 mg of source material powder, which contained a 1:1 ratio of ZnO powder and carbon powder by mass. The powder was spread evenly across the base of the crucible. Two substrates with the textured film seed layer were placed face down on top of the crucible. The crucible and substrates were placed in the tube furnace and dried for 30 minutes at 160 ºC under vacuum (~ 50 mT). Next, argon gas was introduced at a flow rate of 30 SCCM, and the furnace was ramped to 960 ºC, the growth temperature. Once the growth temperature was reached, oxygen was introduced at 10 SCCM, and the growth proceeded for 10 minutes at 50 Torr pressure. After the growth time, the furnace was allowed to cool

and the samples were removed. The growth resulted in vertical, aligned ZnO nanowires approximately 100 µm in length.

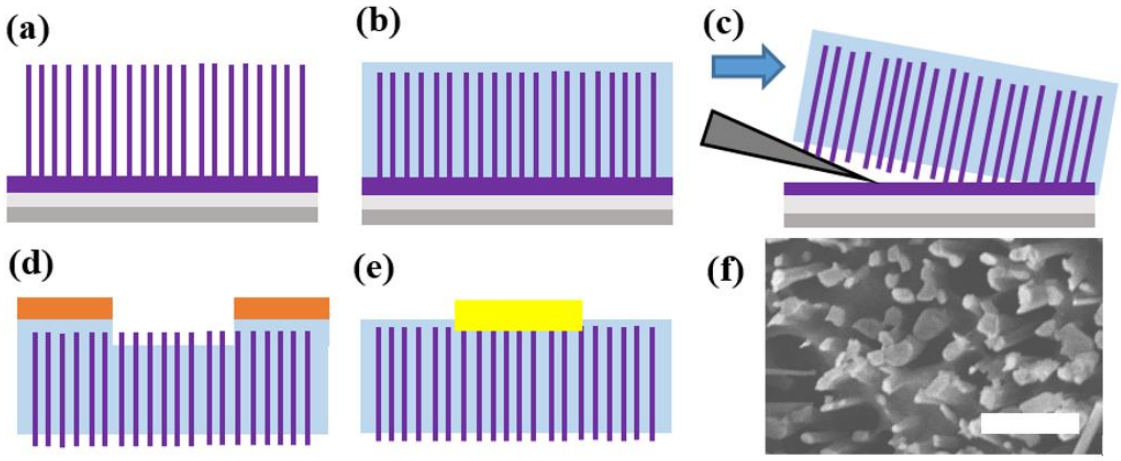

Figure 25. Piezotronic strain sensor fabrication steps. (a) ZnO Nanowires grown by CVD on silicon wafer with hydrothermal textured seed layer. (b) PDMS infiltrated into nanowire array with vacuum chamber and spin coating. (c) Mechanical transfer of ZnO nanowires and new stretchable PDMS substrate. (d) PET mask and plasma etching to expose nanowire tips in PDMS. (e) Deposition of gold top electrode and mask removal. (f) SEM image shows exposed nanowires on bottom of PDMS substrate following mechanical transfer. Scale bar is 5 µm.

A layer of PDMS was drop-coated onto the CVD-grown nanowires to protect the nanowires and act as a stretchable device substrate. Next, the samples were degassed under vacuum. This served to remove air trapped in the nanowires, and improve infiltration of the PDMS polymer. Excess PDMS was then spun off using a spin coater at 4,000 rpm for 2 minutes. The PDMS was cured on a hot plate at 150 ºC for 1 hour. Figure 25b shows the ZnO nanowires embedded in PDMS. After curing, the PDMS layer and embedded nanowires were mechanically removed from the silicon substrate with a razor as shown in

figure 25c. The removed PDMS became the new, stretchable substrate for the embedded ZnO nanowires.

After removal from the Si wafer, the PDMS samples were flattened on a glass slide and covered with a polymer mask made from PET. The mask had rectangular windows approximately 2 mm x 10 mm in size which exposed a part of each sample as seen in figure 25d. Reactive Ion Etching (RIE) was used to remove PDMS from the mask windows and expose the tips of the nanowires. The PDMS was etched for 25 minutes using 45 SCCM SF_6:15 SCCM O_2. A second etch was performed for 30 seconds using oxygen plasma, which has been shown to improve the adhesion of the top electrode and improve the quality of the Schottky contact (14, 149, 150). After oxygen cleaning, a 5 thick nm Cr adhesion layer and 100 nm thick Au top electrode were deposited using electron beam evaporation (figure 25e). The etching mask and excess gold were removed, and the strain sensor was attached to the stepped shaft with silver paint. The mechanical transfer process was characterized with SEM imaging. The SEM image in figure 25f shows ZnO nanowires protruding from the bottom surface of the PDMS after removal from the silicon wafer. The silver paint formed an Ohmic contact with the exposed nanowires on the bottom of the device, and served as the bottom electrode.

The performance of the strain sensor was tested in a structural monitoring application, using a stepped shaft with a shoulder fillet. The shaft was 4.5 inches long, with major and minor diameters of 0.75 and 0.5 inches, respectively. The radius of the shoulder fillet was 0.25 inches. For the given geometry the shaft was calculated to have a

stress concentration factor of K_T = 1.1. Figure 26a shows an image of the sensor attached to the shaft with silver paint.

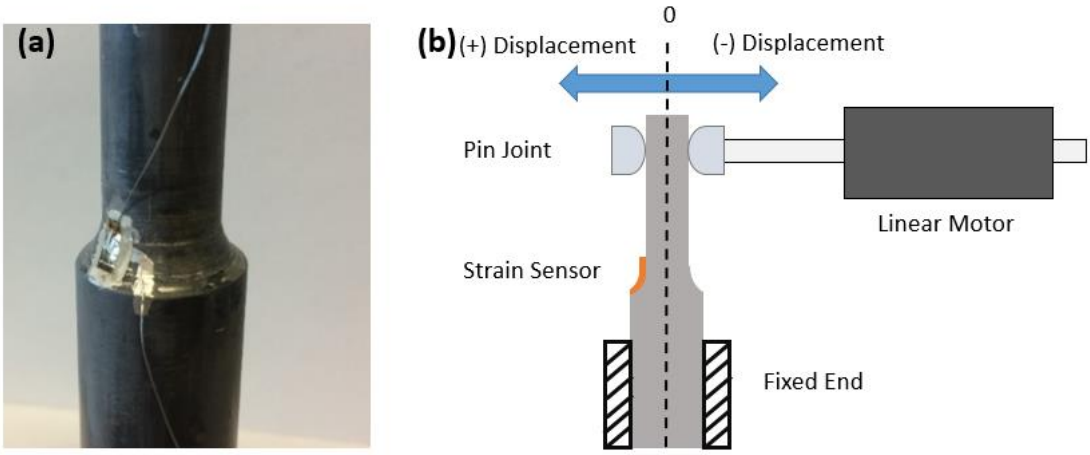

Figure 26. Stretchable and conformal piezotronic strain sensor testing. (a) Image of stretchable and conformal strain sensor attached to shaft fillet with silver paint and wire leads. (b) Schematic of device testing setup showing periodic displacements applied by linear motor.

Electrical testing of the strain sensor was performed to measure the current-voltage (I-V) and current-time (I-t) characteristics. I-V behavior was measured for a 200 mHz sinusoidal voltage sweep, from -1.5 V to + 1.5 V, using LabVIEW. I-t behavior was measured for a periodic bending load applied to the shaft. The base of the shaft was fixed, and a periodic lateral displacement was applied to the top of the shaft with a linear motor (LinMot) as seen in figure 26b. The shaft was oriented such that the strain sensor would experience compressive strain under positive displacements, and tensile strain under negative displacements. A bias voltage was applied to the gold top electrode and the silver

bottom electrode was set to ground. The lateral displacement was applied periodically and the change in conductivity was recorded as a function of time.

The mechanical transfer process successfully created a new, stretchable PDMS substrate for the ZnO nanowires. The stretchable behavior of the new substrate is demonstrated in figure 27a and figure 27b which show the sensor stretching to approximately 150 % of its original length without breaking. Figure 27c shows the small radius of curvature that can be achieved by the sensor. The stretchable and conformal nature of the PDMS substrate could allow for the measurement of large strains and small features.

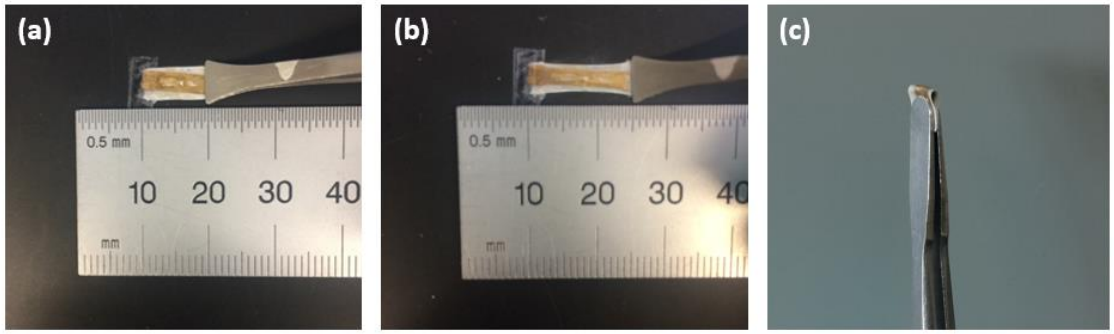

Figure 27. Mechanical characterization of stretchable strain sensor. (a) Image of sensor in un-stretched state and (b) stretched to approximately 150 % of original length. (c) Image of sensor folded to achieve small radius of curvature.

The electrical response of the strain sensor was characterized using bench testing equipment including a waveform generator and current amplifier. The nonlinear, rectifying I-V behavior in figure 28a confirmed the existence of a Schottky contact between the gold top electrode and the ZnO nanowires. The conductance of the device changed under

applied strain as explained by the piezotronic effect. A + 200 mV bias voltage was applied to the top electrode, and a periodic bending displacement was applied to the end of the stepped shaft. Figure 28b shows the current as a function of time in response to a periodic displacement of + 2.5 mm. Figure 28c shows the response under a displacement of – 2.7 mm. The current increased under compressive strain (positive displacement of the shaft) and decreased under tensile strain (negative displacement of the shaft). Several devices were fabricated and showed similar trends for I-V and I-t behavior, verifying the repeatability of the device.

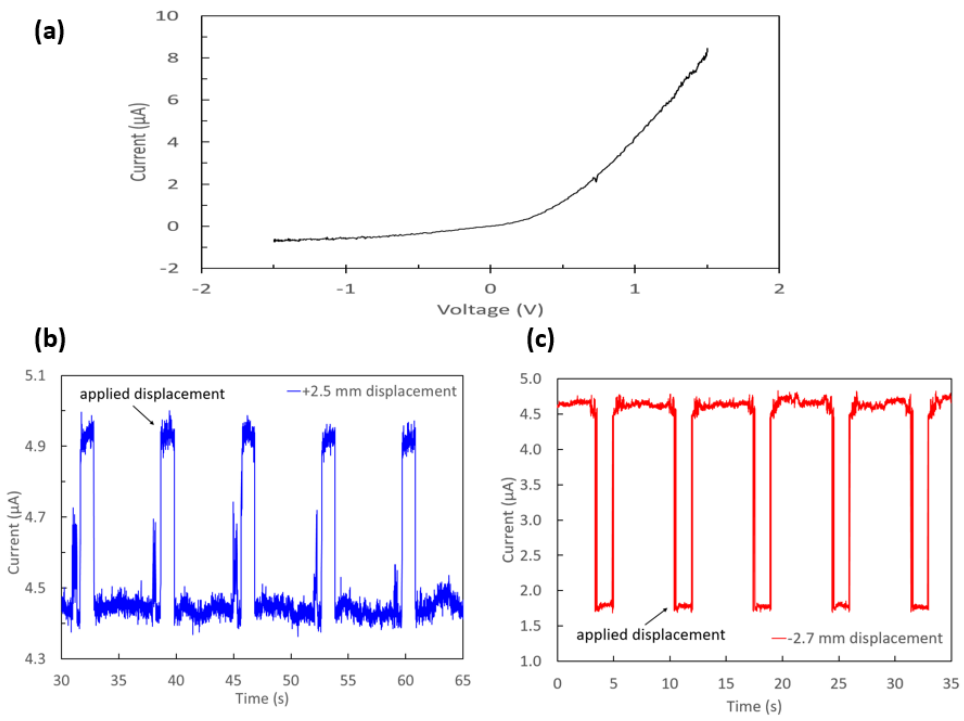

Figure 28. Electrical characterization of stretchable piezotronic strain sensor. (a) I-V response for a stretchable strain sensor showing a Schottky contact. (b) Conductance change under periodic displacement of + 2.5 mm and (c) -2.7 mm, for a bias voltage of + 200 mV.

Noise spikes were observed at the initial application of the applied displacement, and could be due to vibration of the test fixture, imperfect adhesion of the sensor to the shaft, or the motion profile of the linear motor.

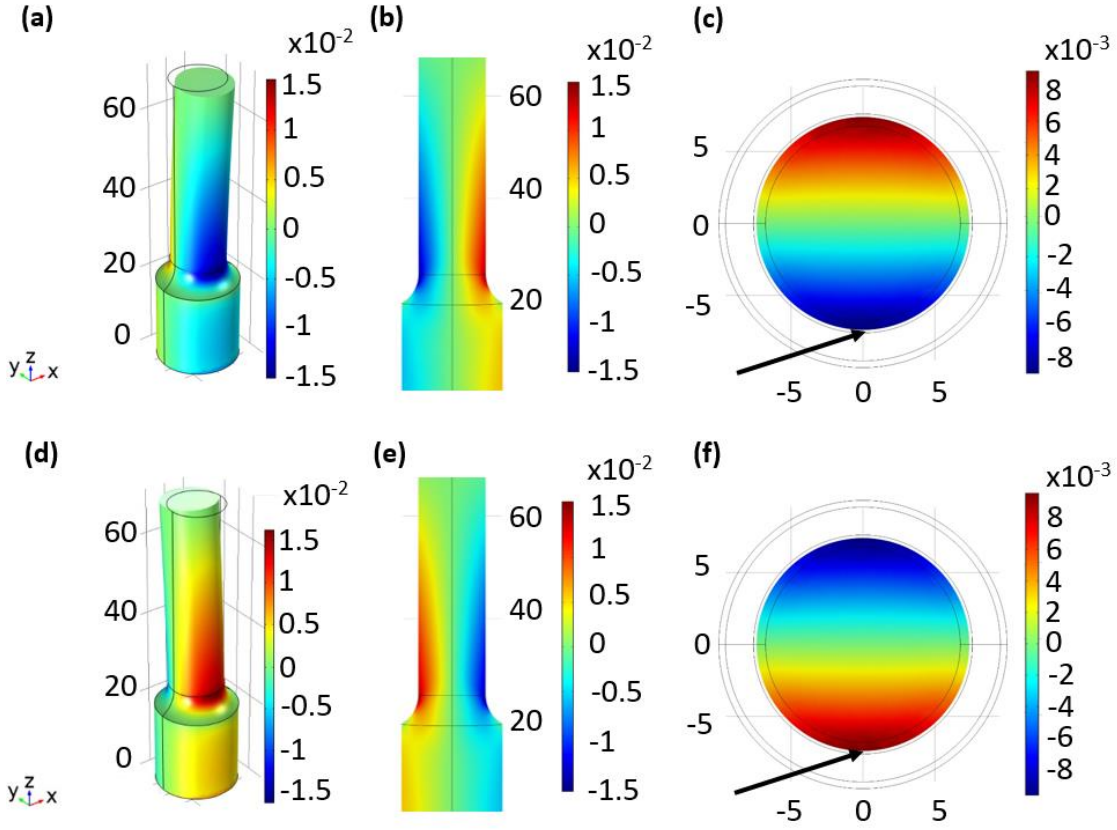

Figure 29. ZZ component of strain tensor for a stepped shaft under applied displacements. (a-c) Strain from +2.5 mm displacement. (a) Isometric view, (b) YZ plane slice and (c) XY plane slice at z = 22.75 mm. (d-f) Strain from a -2.7 mm displacement (d) Isometric view, (e) YZ plane slice and (f) XY plane slice at z = 22.75 mm. Arrows indicate location of estimated strain values. Grid values are shaft dimensions in mm, all deformations to scale.

An FEA model of the stepped shaft was created in COMSOL Multiphysics as seen in figure 29. The model was used to estimate the strain experienced by the sensor. The

length of the shaft was modified to account for the location of the applied displacement and fixed boundary constraint. The bottom surface of the shaft was fixed, and the displacements were applied to the top surface of the shaft in the ± y direction. The zz component of the strain tensor in the stepped shaft is shown in figure 29. Isometric views of the strain in the deformed shaft are presented in figure 29a and figure 29d for the +2.5 mm and -2.7 mm displacements, respectively. Figure 29b and figure 29e show the respective side views of the YZ plane slice for positive and negative displacements. As figure 29 shows, the strain distribution is not uniform in the stepped shaft as it would be for a shaft of uniform cross section. This presents a challenge, in that the size and location of the sensor may affect the strain measurement. It is likely that the ZnO nanowires experienced varying strain across the surface of the shoulder fillet. For this study, the strain was calculated at an area near the middle of the shoulder fillet, at a height of z = 22.75 mm in the model. Figure 29c and figure 29f show the cross-section of the strain distribution at a height of z = 22.75 mm for positive and negative displacements, respectively. Arrows indicate the locations where strain was measured in the simulation, and these values were taken to be the average maximum strain experienced by the sensor. The strain was estimated to be ε = -8.9E-3 for the positive displacement, and ε = 9.6E-3 for the negative displacement. The figure of merit for strain gauges is called the gauge factor (GF) and is given by

$$GF = \left| \frac{\Delta I / I_0}{\varepsilon} \right|$$

where I_0 is the initial current without strain, ΔI is the change in current due to strain, and ε is the applied strain. For the -2.7 mm displacement, the gauge factor was calculated to be 64. This value is comparable to a similarly conformal ZnO/carbon fiber fabric piezotronic strain sensor with a gauge factor of 81 (72). A conventional metal strain gauge, for comparison, has a GF of only about 2 (80). The gauge factor of the stretchable strain sensor can likely be increased by improving the adhesion, and therefore the load transfer, between the sensor and measured structure. The properties of the stretchable polymer used for the substrate may also affect the sensitivity. While the low modulus PDMS substrate might reduce the strain sensitivity on rigid structures, this tradeoff allows for measurements on complex surfaces such as stress concentrators. Strain gauges operating under the piezotronic effect have the potential for even higher sensitivity, as evidenced by Zhang et al., who achieved a gauge factor of 1813 for a similar flexible, but not stretchable, ZnO strain sensor (67).

Future work includes challenges such as improving strain transfer between the structure and strain gauge. Strain transfer performance is affected by adhesive properties (151). The silver paint used as the bottom electrode also acted as an adhesive, but was susceptible to voids and delamination. The PDMS substrates also tended to curl up after being removed from the silicon wafer, contributing to delamination. Despite these challenges, there are advantages of working with stretchable polymer substrates. Soft, stretchable strain sensors can conform to complex shapes, are mechanically compatible with biological tissue, and have little impact on the rigidity and strain in the measured part.

The high sensitivity enabled by the piezotronic effect allows for strain measurement on rigid surfaces, despite the relatively low modulus of the PDMS substrate.

3.4 Chapter summary

Due to the high sensitivity and high spatial resolution, piezotronic force sensors are ideal for replicating human tactile perception in applications such as prosthetics and haptics. Finite element modeling validated the design of a contact force sensor capable of detecting shear and normal forces, at thresholds exceeding human force perception. The proposed piezotronic shear and normal force sensor could have applications in prosthetics and haptics for object grasping and shape perception.

Mechanical transfer of CVD grown ZnO nanowires allowed for the creation of a stretchable and conformal strain sensor on a PDMS substrate. The ZnO/Au electrode interface formed a Schottky contact, which is responsible for the nonlinear I-V response and high sensitivity of piezotronic devices. Applied strains generated piezopotentials in the ZnO nanowires, which altered the Schottky barrier height and changed the conductivity in accordance with the piezotronic effect. The piezotronic strain sensor successfully measured the strain on the shoulder fillet of a stepped shaft, and achieved a gauge factor of 64, higher than that of a conventional metal strain sensor. The strain sensor responded to both positive and negative strains, and could be used to monitor strain on a rotating shaft under reversed loading conditions. The sensor can conform to complex surfaces, and the low modulus PDMS substrate is mechanically compatible with other stretchable materials, such as human skin. With further development, the sensor could see use in applications such as smart bandages and biomechanics monitoring.

Chapter 4. Design of a substrate cooling assembly for CVD systems

4.1 Chemical vapor deposition

4.1.1 Chemical vapor deposition method and synthesis of monolayer MoS_2

Chemical vapor deposition can be used to synthesize various nanostructures including ZnO nanowires. For the CVD process, a blend of zinc oxide and carbon powder is vaporized at 960 ºC in a tube furnace under low pressure and allowed to condense onto a zinc oxide sputter-coated substrate. The zinc oxide forms hexagonal Wurtzite crystals which grow preferentially in the c-direction, through a carbothermal reaction (152, 153).

Chemical vapor deposition can also be used to grow monolayer MoS_2, either directly from MoS_2 powder, or by sulfurization of molybdenum trioxide (MoO_3) (32, 33). Si/SiO_2 is typically used as a growth substrate. Piranha solution is often used as substrate cleanliness can affect growth (27). There are many motivations to find alternate CVD growth substrates for nanomaterials. Polymer substrates are very popular due to the great interest in flexible electronics. FeS_2, or iron pyrite is another potential substrate for the growth of molybdenum disulfide, and is desirable due to its low cost. These substrates, however, are incompatible with the high temperatures of the CVD process. There is a need for a CVD process that is compatible with low-temperature substrates, while still producing the high-quality nanomaterials that CVD is known for.

4.1.2 Structure and function of CVD tube furnace

The tube furnace consists of an 1120 mm long alumina tube, with an inner diameter of 39 mm and a wall thickness of 3 mm. The tube is placed inside of an insulated box which contains resistive heating elements as shown in figure 30a. The free ends of the

ceramic tube extend out of the box on each end for a length of approximately 150 mm. The furnace can reach temperatures up to 1200 ºC, and can be programmed to perform ramps and dwells at various temperatures. Two thermocouples measure the temperature at the center of the furnace, and the set-point is maintained by a controller.

Each end of the furnace is closed by a custom fabricated stainless steel endcap. The endcaps circulate chilled water around the exposed ends of the furnace tube for safety, and to protect the rubber gaskets that seal the tube. The upstream endcap is connected to a gas supply line which allows carrier and reaction gases such as argon and oxygen to enter the furnace. Gas flow rates are controlled by mass flow controllers. The downstream endcap is connected to a vacuum pump or vented directly to the fume hood. The endcaps provide a vacuum seal using rubber gaskets. The vacuum pump can achieve approximately 20 mT of pressure. Chilled water is provided to the furnace by an overhead manifold connected to the building chilled water supply. Figure 30b shows an experimental setup for CVD growth of ZnO nanowires, and figure 30c shows an image of the furnace during operation.

The controller maintains the furnace set-point temperature at the center of the tube furnace. Away from the center, the temperature decreases. Different source materials can be heated to different temperatures in the furnace by placing them at the appropriate position in the furnace. In order to determine the positon to place the materials, the temperature as a function of position was measured.

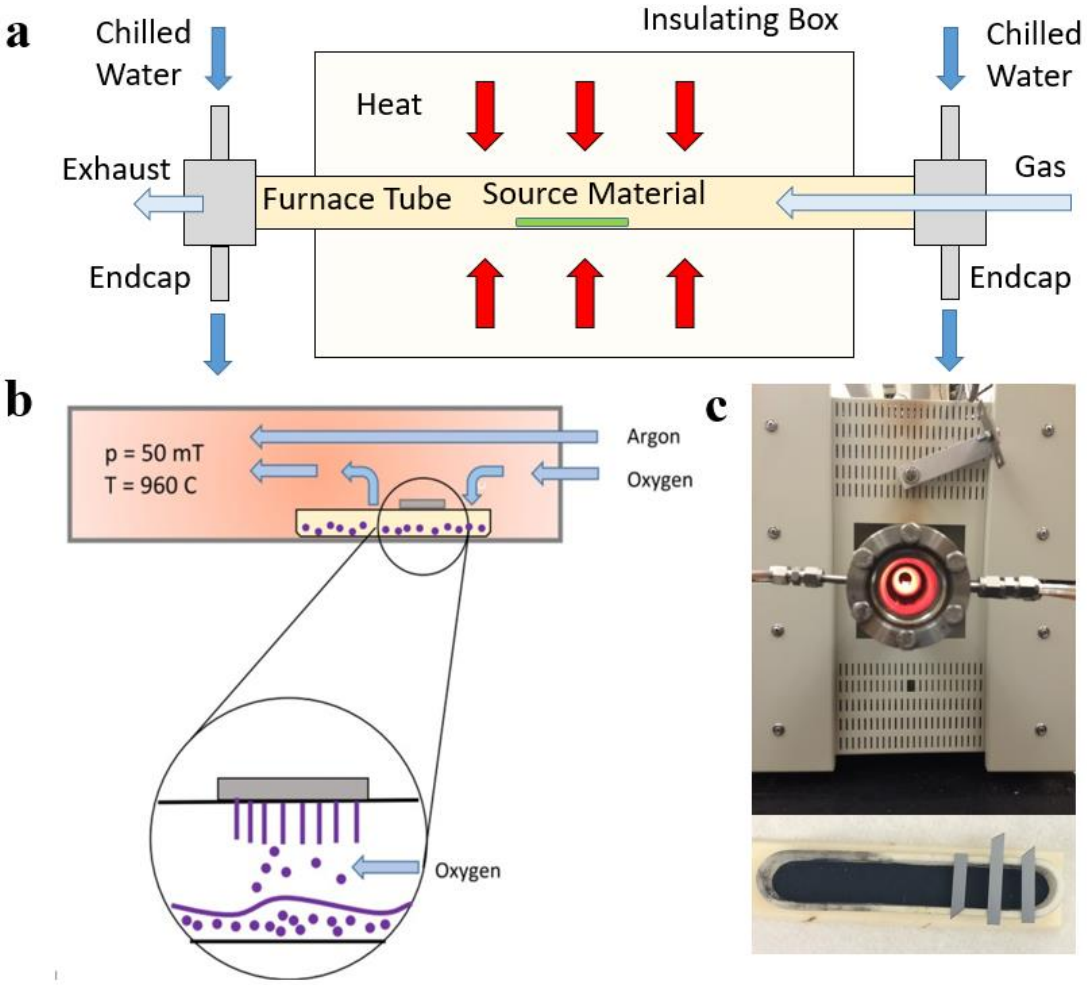

Figure 30. Major components and operation of a CVD tube furnace. (a) Schematic of tube furnace geometry and major components. (b) Experimental setup for CVD growth of ZnO nanowires. ZnO and carbon powder are vaporized and form vertical ZnO nanowires on substrate. (c) Photo of tube furnace heated to 960 ºC, viewed through the endcap (top), and picture of ceramic crucible with source material and Si substrates (bottom).

The temperature profile was measured along the length of the tube with a thermocouple. The furnace was set to the MoS_2 growth temperature of 700 ºC, and allowed to stabilize for 1 hour. The thermocouple was moved from the open end of the furnace to the center. A special fixture was used to hold the thermocouple in the center of the tube

diameter, away from the walls. The temperature was recorded at 10 mm intervals, and the thermocouple was held at each location for a short time until the temperature measurement stabilized. Results for the temperature profile as a function of position in the tube furnace are presented in figure 31.

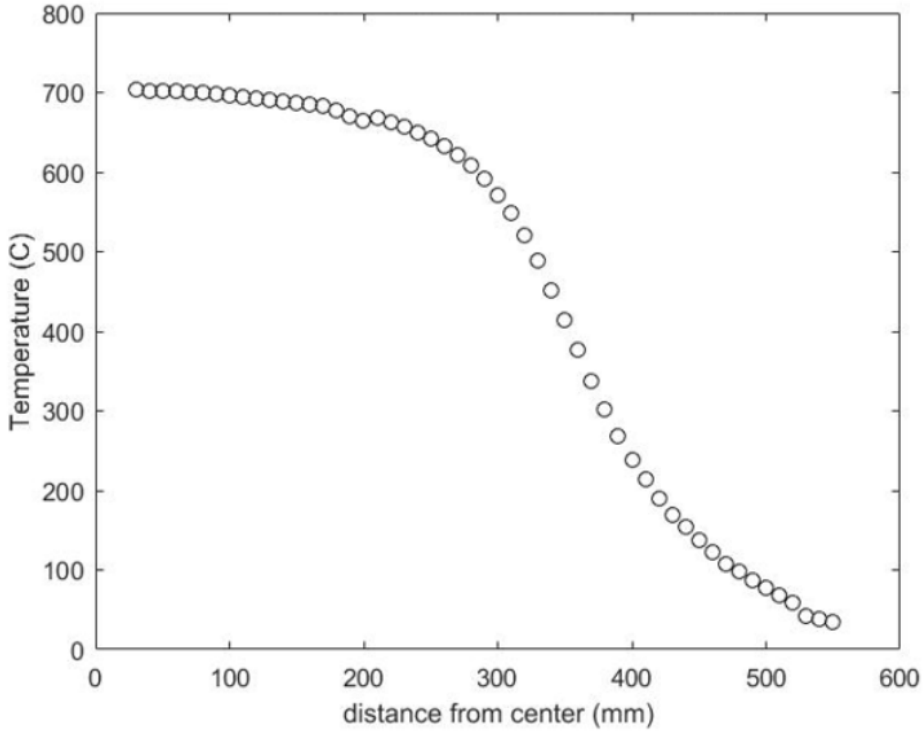

Figure 31. Temperature profile in a CVD tube furnace. The furnace was set to 700 ºC. Temperatures were measured at various distances from the center of the tube, in mm. Temperature profile is for ½ of the tube length.

4.2 CVD substrate cooling assembly design

One of the major limitations of chemical vapor deposition is the high temperatures involved. These high temperatures are necessary for vaporizing the source material for the chemical reaction, but are incompatible with many substrates such as polymers. CVD can produce high quality nanomaterials that cannot currently be achieved by other means.

There is widespread and growing interest in flexible electronics on polymer substrates, and these devices can benefit the high quality nanomaterials grown by CVD. Additionally, patterning of nanomaterials is very important for creating multi-channel devices and other reasons. Such patterning is often achieved by photolithography, a microfabrication techniques which uses UV sensitive polymers. Nanomaterial synthesis commonly relies on so called epitaxial seed layers. In other words, the crystal structure of the seed layer must match the crystal structure of the nanomaterial. Epitaxial seed layer materials can be expensive, however. Alternative seed layers with a near-epitaxial match can be much more affordable, but may not be compatible with high temperatures.

The CVD furnace provides a wide ranging, location-dependent temperature profile. However, at present, a single location cannot provide both the high temperature needed for the reaction, and the low temperature needed for certain substrates. The goal of this project was to develop a cooling assembly which can provide localized cooling to a substrate placed in the high-temperature region of the furnace.

The substrate cooling apparatus must meet multiple design requirements. First, the assembly must provide sufficient localized cooling to the substrate without reducing the high temperature near the source material. There must be sufficient clearance between the inner wall of the tube furnace and the cooling assembly to avoid conductive heat transfer. Finally, the apparatus must survive the high temperature chemical environment inside the tube furnace.

The assembly achieves localized cooling of the substrate by circulating chilled water inside of the furnace. The overriding design constraint was the geometry of the tube

furnace. The tube furnace has an inner dimeter of 39 mm, and must contain the cooling assembly and room for a ceramic crucible to hold the source material. Within this size envelope, the design was optimized to maximize several objectives. First, the diameter of the tubes which deliver and remove the chilled water was maximized to deliver the highest volume of water. Second, the volume of chilled water was maximized in the immediate vicinity of the substrate. Third, the diameter of the sample stage was maximized to accommodate the largest sample possible. Fourth, the assembly was designed to allow for a wide adjustment of sample height. The sample height refers to the vertical distance from the source material to the substrate. A layer of insulation was wrapped around the chilled water tubes, and the thickness of the insulation was maximized. Finally, the assembly was designed to use standard tube stock sizes whenever possible to minimize cost and lead time.

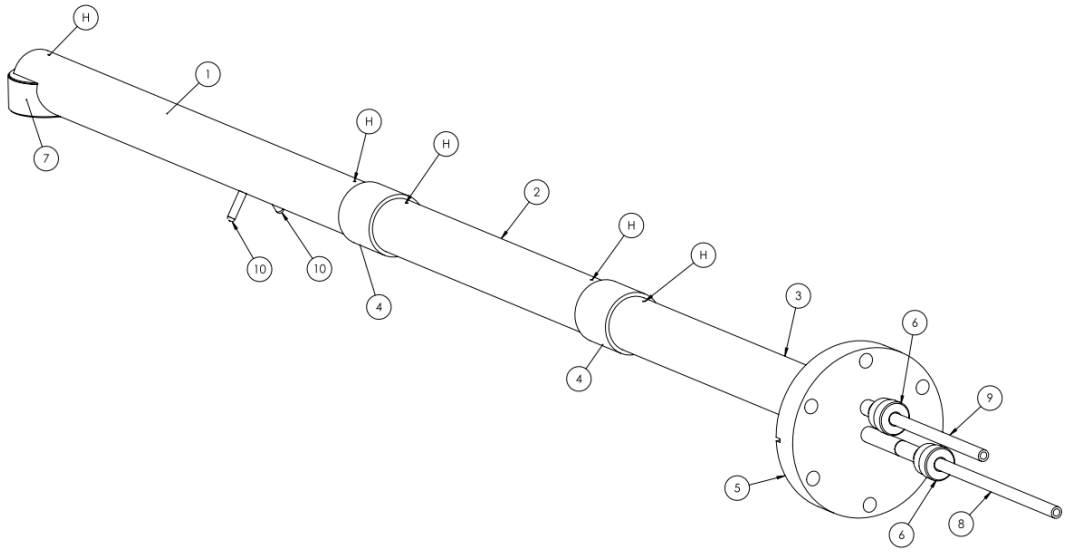

Figure 32. Major components of CVD cooling assembly. Major assembly components are numbered. Item 7 is the *sample cooling chamber*, items 1, 2, and 3 are the *insulating sleeves*, and item 5 is the *endcap*. Items 8 and 9 are the chilled water *inlet and outlet tubes*.

The assembly was designed with type 304 stainless steel for corrosion resistance. Wall thicknesses for the tubes ranged from 0.02 inches to 0.12 inches. The maximum temperature of the steel is 1500 ºF, or 815 ºC, which is above the synthesis temperature for MoS_2. The furnace consists of three main components, which are shown in figure 32. The *sample cooling chamber* is a cylindrical chamber in which the substrate is placed. Cooling water circulates around the outside of the chamber, and a layer of insulating silica fabric surrounds the cooling water. The silica fabric was 0.054 inches thick, and has a maximum temperature of 980 ºC. The entire sample stage is enclosed in 304 stainless steel. The sample sits on a stainless steel, grated platform. The inside of the chamber is threaded, and the sample platform can be adjusted up and down to change the distance from the substrate to the source material. Chilled water is delivered to the substrate chamber by a long tube leading into the furnace, and a second tube removes the circulated, heated water. Figure 33 details the design of the sample cooling chamber. An assembly view of the chamber is shown in figure 33a, while figure 33b and figure 33c show cutaway drawings. Figure 33d shows the adjustable height substrate stage.

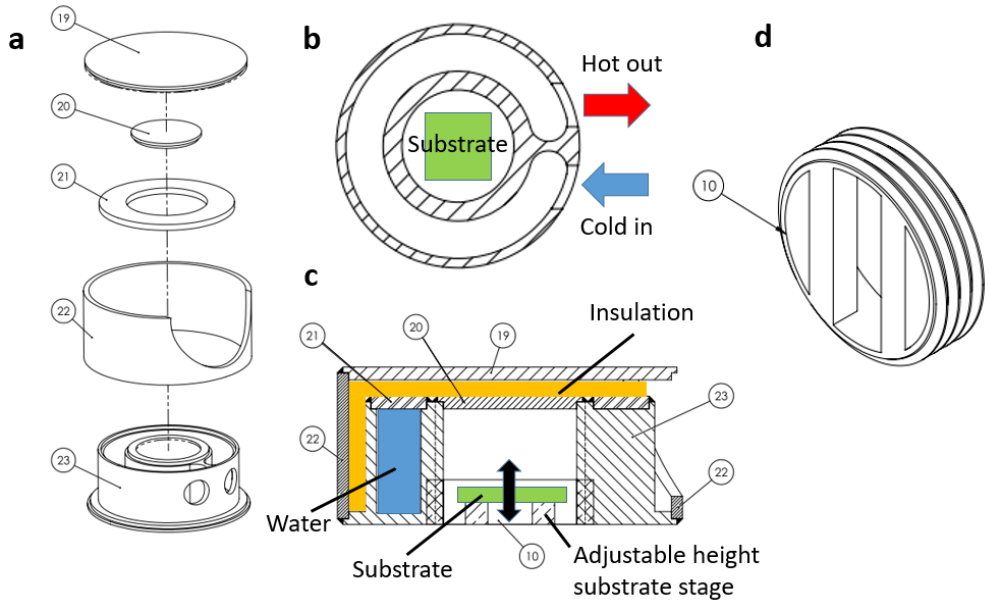

Figure 33. Detailed view of sample cooling chamber. Individual drawing items are numbered. (a) Assembly diagram of sample cooling chamber components. (b) Top view of drawing item 23, showing separated cold water inlet and hot water outlet. Chilled water circulates around substrate. (c) Side cutaway view of *sample cooling chamber*. Substrate sits on height-adjustable sample stage (item 10). Silica insulation fabric and water compartment are shown. (d) View of sample stage with external threads for height adjustment.

The second component is a series of insulating sleeves which surround the inlet and outlet cooling water tubes. The sleeves consist of an outer cylinder made of stainless steel, and two inner cylinders which slide over the cooling water tubes. The sleeves are packed with silica insulating fabric, and welded closed. There are three sleeves total, each approximately 185 mm in length. The first sleeve is permanently attached to the sample cooling chamber. The additional two sleeves may be slid on to the assembly to adjust the length. One, two, or three sleeves may be used. The number of sleeves determines the length of the cooling assembly, and the horizontal position of the substrate in the tube

furnace. This allows the cooled substrate to be placed in different temperature zones. The permanent sleeve has two support legs which keep the assembly from bending. Slide-on alignment collars keep the sleeves concentric. Figure 34 illustrates the insulating sleeve assembly (top) and cutaway view (bottom).

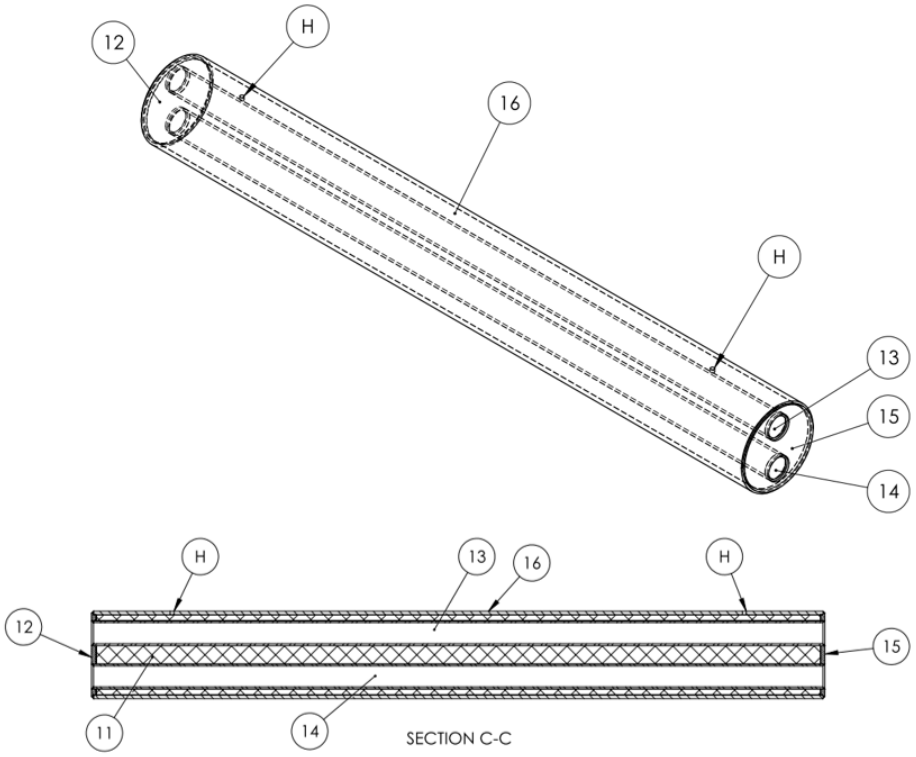

Figure 34. Detailed view of insulating sleeve assembly. Isometric view (top) and side view (bottom). Cross-hatching shows location of insulation.

The third component is an endcap plate, designed to connect to the existing endcaps on the furnace. The endcap plate has two Swagelok fittings that the inlet and outlet water tubes pass through as illustrated in figure 35. The inlet and outlet tubes slide through the fittings to adjust the length, and the fittings can be tightened and sealed.

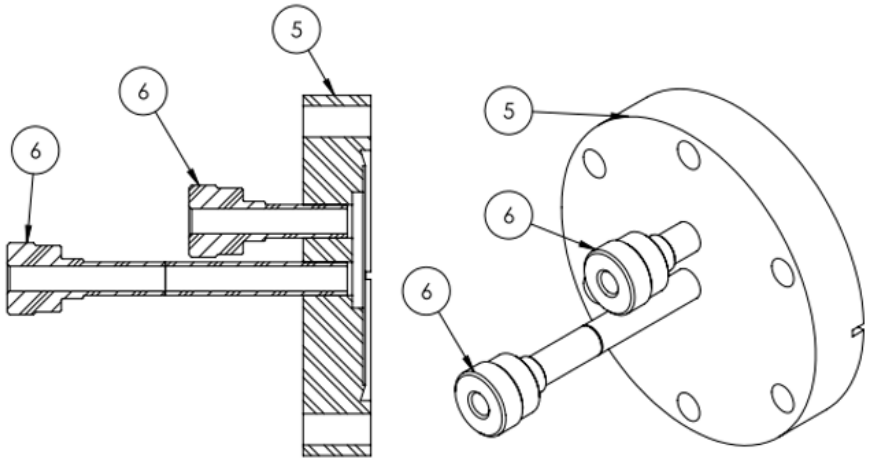

Figure 35. Detailed view of cooling assembly endcap. Drawings show fittings for inlet and outlet cooling water tubes (item 6).

A detailed drawing package was completed for the assembly, and the assembly was fabricated by the College of Science and Engineering machine shop. Photographs of the fabricated assembly can be seen in figure 36a and figure 36b. The inset of figure 36b shows a close-up image of the sample stage. Cutaways drawings of the sample cooling stage and insulating tube are presented in figure 37a. Figure 37b shows a cutaway drawing of the completed cooling assembly installed in the tube furnace. Figure 38 shows a cross-section view of the furnace tube with cooling assembly and source material crucible.

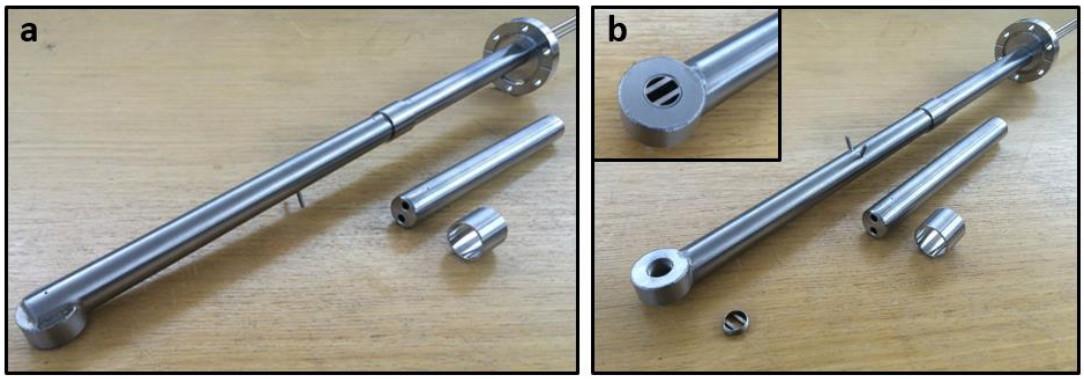

Figure 36. Fabricated cooling assembly[2]. (a) Picture of cooling assembly from the top view with extra insulating sleeve and alignment collar. (b) Picture of cooling assembly from the bottom view showing the sample chamber and sample stage. Inset shows sample stage installed. Assembly fabricated by CSE machine shop, University of Minnesota.

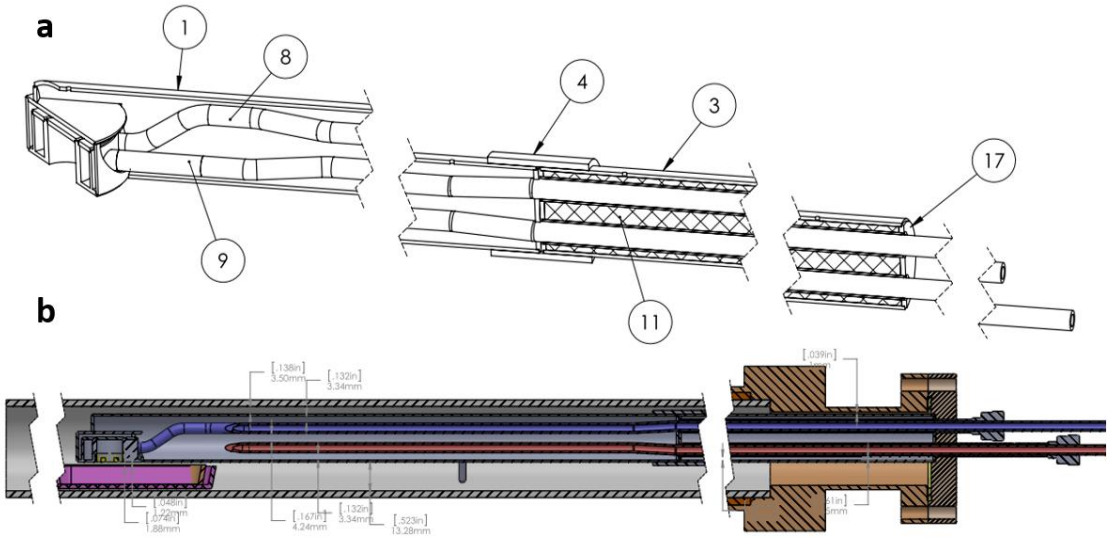

Figure 37. Cutaway views of cooling assembly. (a) Isometric view of cooling chamber and insulating sleeve. (b) Side view of cooling assembly and tube furnace with crucibles for source material.

[2] Cooling assembly was fabricated by staff at the College of Science and Engineering Machine Shop at the University of Minnesota.

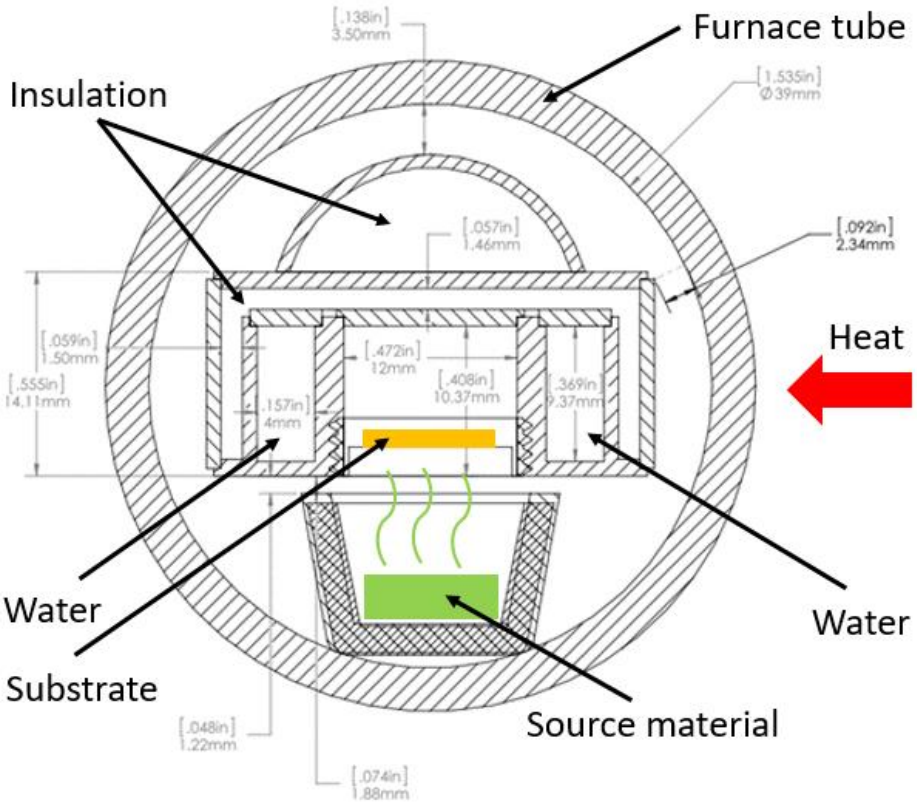

Figure 38. Cross-section view of cooling assembly in tube furnace. Cross-section view of cooling assembly installed in tube furnace with source material crucible. Heat vaporizes source material, while cooling assembly maintains substrate at cooler temperature.

4.3 CVD cooling assembly testing and synthesis of MoS_2 on FeS_2 substrate[3]

To better understand the effectiveness of the cooling assembly, the input and output cooling water temperatures were measured with the furnace at a temperature of 700 ºC. The input temperature of the cooling water was 11.7 ºC, while the output temperature was measured to be 13.8 ºC. Next, the assembly was tested by attempting to synthesize MoS_2 on a low-temperature FeS_2 substrate. FeS_2 is a potential low-cost alternative to

[3] Growth and characterization of MoS_2 was performed by Dr. Huimin Hao.

conventional growth substrates, but will decompose at typical MoS_2 synthesis temperatures. A schematic of the synthesis process is shown in figure 39. A small piece of FeS_2 was broken from a larger sample shown in figure 40. The FeS_2 substrate was placed in the cooling assembly. Ceramic plates with source materials (MoO_3 and Sulfur powder) were placed in the 700 ºC and 200 ºC regions of the furnace, respectively. After the growth recipe was completed, the FeS_2 substrate was removed. SEM investigation showed MoS_2 nanostructures on the FeS_2 substrate as shown in figure 41. The FeS_2 substrate was not visibly damaged by the high temperature, suggesting that the cooling assembly is effective for protecting low-temperature substrates.

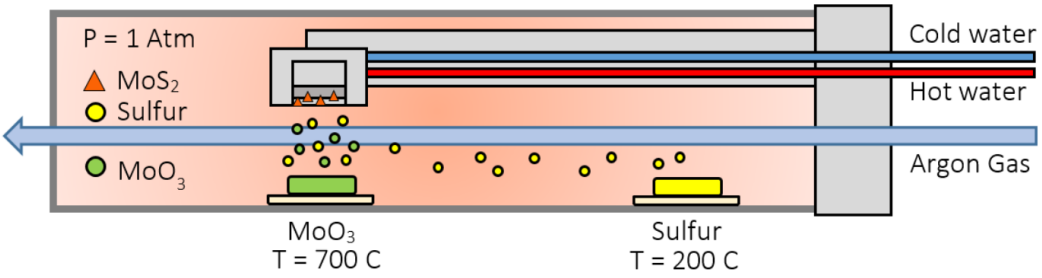

Figure 39. Schematic of MoS_2 growth in tube furnace with CVD cooling assembly.

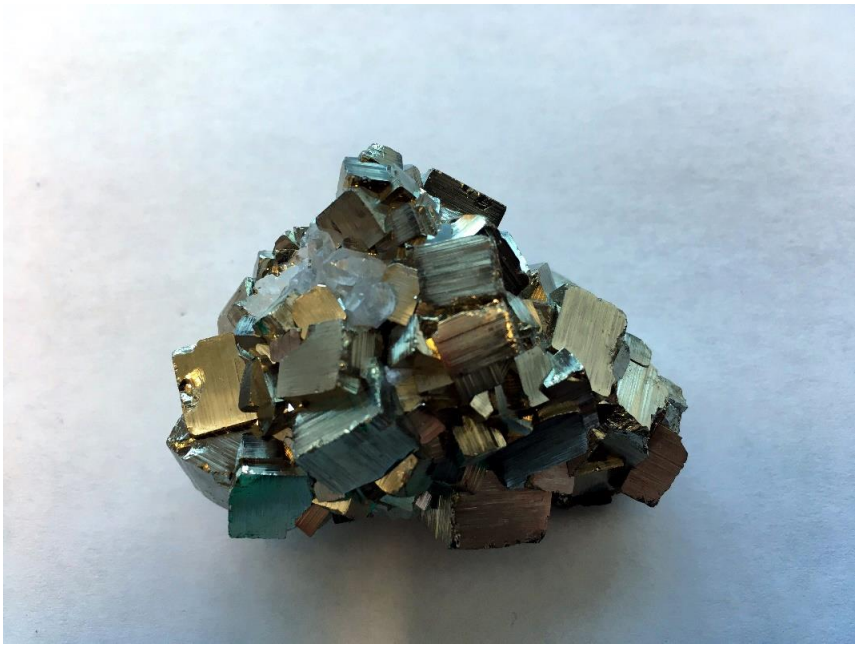

Figure 40. Sample of iron pyrite (FeS_2) substrate material.

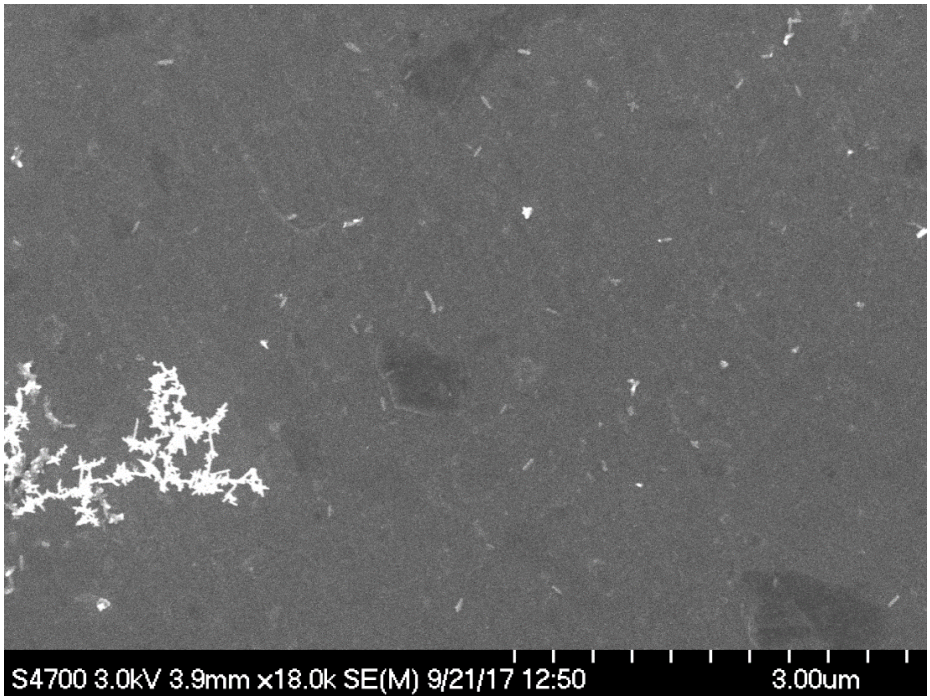

Figure 41. SEM image of MoS_2 structures grown on FeS_2 substrate with CVD cooling assembly.

4.4 Chapter summary

Chapter 4 detailed the design and testing of a CVD furnace cooling assembly. The assembly was designed to allow for the use of low-temperature substrates in the high temperature CVD material synthesis process. To investigate the design performance, the cooling water inlet and outlet temperatures were characterized. The device functionality was further verified by demonstrating growth of MoS_2 nanostructures on a FeS_2 substrate without damaging the substrate. Future work will focus on optimization of the growth parameters to be used with the cooling assembly. The device has the potential to enable the use of additional low-temperature substrates, such as polymers, for CVD synthesis of other nanomaterials including ZnO. The cooling assembly can expand the CVD process to new, low-temperature substrates, potentially enabling new device architectures based on piezoelectric nanomaterials.

Chapter 5. Conclusions

The inherent electromechanical coupling and unique properties found in piezoelectric nanomaterials make them well suited for many applications such as mechanical energy harvesting, and force or strain sensing. Despite great progress, there are barriers to the continued development of new piezoelectric nanomaterial devices. First, there is a limited understanding of piezoelectric behavior in emerging nanomaterials, and second, there are limitations of current fabrication techniques. This thesis explored these challenges through finite element modeling and the expansion of current fabrication techniques in order to realize new piezoelectric nanomaterial devices.

First, chapter 2 explored piezoelectric behavior in diphenylalanine (FF) peptide, a new bio-inspired piezoelectric material, interesting for its promising electromechanical properties and sustainable synthesis. Using emerging material properties, a finite element model of a single nanowire was created to compare the piezoelectric behavior of FF peptide and conventional piezoelectric materials. The nanowire model predicted that FF peptide could generate significantly higher voltages than conventional piezoelectric nanomaterials under the same applied force. Next, a 2D model of a flexible FF peptide nanogenerator was created to predict the device performance. Synthesis of FF peptide microrods was achieved on a polymer substrate, and the first flexible piezoelectric FF peptide nanogenerator was realized. The device was fabricated and characterized, and the measured output validated the finite element model. Finite element modeling can successfully predict the piezoelectric behavior of FF peptide, and the development of FF

peptide devices on flexible substrates can enable new applications such as wearable devices and flexible electronics.

Next, chapter 3 explored a special class of piezoelectric nanomaterials, those with semiconducting properties, or so called piezotronic nanomaterials. The semiconducting properties of ZnO nanowires make them well-suited for highly sensitive force and strain sensors enabled by the piezotronic effect. Finite element modeling was used to explore a new design for a piezotronic force sensor for haptics and prosthetics applications. Based on beam theory, the design was predicted to detect shear and normal contact forces, and was predicted to exceed the sensitivity of human mechanoreceptors. Ultralong ZnO nanowires, such as those needed for the previous contact force sensor, are produced by chemical vapor deposition. However, the high-temperature process is incompatible with flexible polymers and other low-temperature substrates, which limits device design. A mechanical transfer technique was expanded to CVD grown ZnO nanowires in order to create a new stretchable piezotronic strain sensor on a soft polymer substrate. The gauge factor, or sensitivity of the strain sensor exceeded that of conventional metal strain gauges. Finite element modeling is an important tool for predicting the performance of piezotronic nanomaterial devices, and new device architectures can be realized by expanding current fabrication techniques to new materials and substrates.

Lastly, chapter 4 investigated the design of new process equipment to enable synthesis of piezoelectric nanomaterials on new substrates. MoS_2 is an emerging 2D piezoelectric nanomaterial that, like ZnO, is synthesized by chemical vapor deposition. FeS_2 substrates are a potential low-cost alternative to conventional substrates, but are

incompatible with the high temperatures needed to produce MoS_2 by CVD. An apparatus was designed to allow for the use of low-temperature substrates inside a high-temperature CVD furnace. The assembly delivered chilled water inside of the furnace to provide localized cooling for the growth substrates. The cooling system was successfully used to synthesize MoS_2 on low-temperature FeS_2 substrates in a CVD furnace. The cooling assembly can potentially be used for the synthesis of other piezoelectric nanomaterials and soft polymer substrates, further expanding the use of CVD and allowing new device architectures to be realized.

Piezoelectric nanomaterials are the basis for many types of devices including sensors and energy harvesters. Continued development of these devices will require further exploration of piezoelectric behavior in emerging nanomaterials. The expansion of current fabrication techniques is needed to enable broader synthesis of these materials and to realize new device architectures. New devices enabled by piezoelectric nanomaterials can help to address challenges in sustainable energy, human health, and beyond.

References

1. Zhu R, Jenkins K, Yang R. Degradation and nano-patterning of ferroelectric P (VDF-TrFE) thin films with electron irradiation. RSC Advances. 2015;5(129):106700-5.
2. Kholkin A, Amdursky N, Bdikin I, Gazit E, Rosenman G. Strong piezoelectricity in bioinspired peptide nanotubes. Acs Nano. 2010;4(2):610-4.
3. Wu W, Wang L, Li Y, Zhang F, Lin L, Niu S, et al. Piezoelectricity of single-atomic-layer MoS2 for energy conversion and piezotronics. Nature. 2014;514(7523):470-4.
4. Madou MJ. Fundamentals of microfabrication: the science of miniaturization: CRC press; 2002.
5. Görbitz CH. The structure of nanotubes formed by diphenylalanine, the core recognition motif of Alzheimer's β-amyloid polypeptide. Chemical communications. 2006(22):2332-4.
6. Vayssieres L. Growth of arrayed nanorods and nanowires of ZnO from aqueous solutions. Advanced Materials. 2003;15(5):464-6.
7. Mak KF, Lee C, Hone J, Shan J, Heinz TF. Atomically thin MoS(2): a new direct-gap semiconductor. Phys Rev Lett. 2010;105(13):136805.
8. Wang ZL. ZnO nanowire and nanobelt platform for nanotechnology. Materials Science and Engineering: R: Reports. 2009;64(3-4):33-71.
9. Agrawal R, Peng B, Gdoutos EE, Espinosa HD. Elasticity size effects in ZnO nanowires− a combined experimental-computational approach. Nano Letters. 2008;8(11):3668-74.
10. Morkoç H, Özgür Ü. Zinc oxide : fundamentals, materials and device technology. Weinheim: Wiley-VCH; 2009. xi, 477 p. p.
11. Wang X, Song J, Liu J, Wang ZL. Direct-current nanogenerator driven by ultrasonic waves. Science. 2007;316(5821):102-5.
12. Xu S, Wei Y, Liu J, Yang R, Wang ZL. Integrated multilayer nanogenerator fabricated using paired nanotip-to-nanowire brushes. Nano letters. 2008;8(11):4027-32.
13. Özgür U, Alivov YI, Liu C, Teke A, Reshchikov MA, Doğan S, et al. A comprehensive review of ZnO materials and devices. Journal of Applied Physics. 2005;98(4):041301.
14. Brillson LJ, Lu Y. ZnO Schottky barriers and Ohmic contacts. Journal of Applied Physics. 2011;109(12):121301.
15. Gao Z, Zhou J, Gu Y, Fei P, Hao Y, Bao G, et al. Effects of piezoelectric potential on the transport characteristics of metal-ZnO nanowire-metal field effect transistor. J Appl Phys. 2009;105(11):113707.
16. Gao Y, Wang ZL. Electrostatic potential in a bent piezoelectric nanowire. The fundamental theory of nanogenerator and nanopiezotronics. Nano letters. 2007;7(8):2499-505.
17. Xu S, Wang ZL. One-dimensional ZnO nanostructures: Solution growth and functional properties. Nano Research. 2011;4(11):1013-98.
18. McPeak KM, Le TP, Britton NG, Nickolov ZS, Elabd YA, Baxter JB. Chemical bath deposition of ZnO nanowires at near-neutral pH conditions without hexamethylenetetramine (HMTA): understanding the role of HMTA in ZnO nanowire growth. Langmuir. 2011;27(7):3672-7.
19. Xu S, Wang ZL. Oxide nanowire arrays for light-emitting diodes and piezoelectric energy harvesters. Pure and Applied Chemistry. 2011;83(12).

20. Xu S, Adiga N, Ba S, Dasgupta T, Wu CF, Wang ZL. Optimizing and Improving the Growth Quality of ZnO Nanowire Arrays Guided by Statistical Design of Experiments. Acs Nano. 2009;3(7):1803-12.
21. Ohyama M, Kouzuka H, Yoko T. Sol-gel preparation of ZnO films with extremely preferred orientation along (002) plane from zinc acetate solution. Thin solid films. 1997;306(1):78-85.
22. Tian JH, Hu J, Li SS, Zhang F, Liu J, Shi J, et al. Improved seedless hydrothermal synthesis of dense and ultralong ZnO nanowires. Nanotechnology. 2011;22(24):245601.
23. Yeo J, Hong S, Wanit M, Kang HW, Lee D, Grigoropoulos CP, et al. Rapid, One-Step, Digital Selective Growth of ZnO Nanowires on 3D Structures Using Laser Induced Hydrothermal Growth. Advanced Functional Materials. 2013;23(26):3316-23.
24. Li X, Cai W, An J, Kim S, Nah J, Yang D, et al. Large-area synthesis of high-quality and uniform graphene films on copper foils. Science. 2009;324(5932):1312-4.
25. Brivio J, Alexander DT, Kis A. Ripples and layers in ultrathin MoS2 membranes. Nano letters. 2011;11(12):5148-53.
26. Young P. Lattice parameter measurements on molybdenum disulphide. Journal of Physics D: Applied Physics. 1968;1(7):936.
27. Liu KK, Zhang W, Lee YH, Lin YC, Chang MT, Su CY, et al. Growth of large-area and highly crystalline MoS2 thin layers on insulating substrates. Nano Lett. 2012;12(3):1538-44.
28. Kam K, Parkinson B. Detailed photocurrent spectroscopy of the semiconducting group VIB transition metal dichalcogenides. The Journal of Physical Chemistry. 1982;86(4):463-7.
29. Lebegue S, Eriksson O. Electronic structure of two-dimensional crystals from ab initio theory. Physical Review B. 2009;79(11):115409.
30. Manzeli S, Allain A, Ghadimi A, Kis A. Piezoresistivity and Strain-induced Band Gap Tuning in Atomically Thin MoS2. Nano Lett. 2015;15(8):5330-5.
31. Scalise E, Houssa M, Pourtois G, Afanas'ev V, Stesmans A. Strain-induced semiconductor to metal transition in the two-dimensional honeycomb structure of MoS2. Nano Research. 2011;5(1):43-8.
32. Najmaei S, Liu Z, Zhou W, Zou X, Shi G, Lei S, et al. Vapour phase growth and grain boundary structure of molybdenum disulphide atomic layers. Nat Mater. 2013;12(8):754-9.
33. Wu S, Huang C, Aivazian G, Ross JS, Cobden DH, Xu X. Vapor–solid growth of high optical quality MoS2 monolayers with near-unity valley polarization. Acs Nano. 2013;7(3):2768-72.
34. Utama MI, Zhang Q, Zhang J, Yuan Y, Belarre FJ, Arbiol J, et al. Recent developments and future directions in the growth of nanostructures by van der Waals epitaxy. Nanoscale. 2013;5(9):3570-88.
35. Shi Y, Zhou W, Lu AY, Fang W, Lee YH, Hsu AL, et al. van der Waals epitaxy of MoS(2) layers using graphene as growth templates. Nano Lett. 2012;12(6):2784-91.
36. Ago H, Endo H, Solis-Fernandez P, Takizawa R, Ohta Y, Fujita Y, et al. Controlled van der Waals epitaxy of monolayer MoS2 triangular domains on graphene. ACS Appl Mater Interfaces. 2015;7(9):5265-73.
37. Li Y, Rao Y, Mak KF, You Y, Wang S, Dean CR, et al. Probing symmetry properties of few-layer MoS2 and h-BN by optical second-harmonic generation. Nano Lett. 2013;13(7):3329-33.
38. Zhu H, Wang Y, Xiao J, Liu M, Xiong S, Wong ZJ, et al. Observation of Piezoelectricity in Monolayer Molybdenum Disulfide. arXiv preprint arXiv:14087074. 2014.

39. Reches M, Gazit E. Casting metal nanowires within discrete self-assembled peptide nanotubes. Science. 2003;300(5619):625-7.
40. Smith AM, Williams RJ, Tang C, Coppo P, Collins RF, Turner ML, et al. Fmoc-Diphenylalanine Self Assembles to a Hydrogel via a Novel Architecture Based on π–π Interlocked β-Sheets. Advanced Materials. 2008;20(1):37-41.
41. Yan X, Zhu P, Li J. Self-assembly and application of diphenylalanine-based nanostructures. Chem Soc Rev. 2010;39(6):1877-90.
42. Adler-Abramovich L, Gazit E. The physical properties of supramolecular peptide assemblies: from building block association to technological applications. Chem Soc Rev. 2014;43(20):6881-93.
43. Silva RF, Araújo DR, Silva ER, Ando RmA, Alves WA. L-diphenylalanine microtubes as a potential drug-delivery system: characterization, release kinetics, and cytotoxicity. Langmuir. 2013;29(32):10205-12.
44. Nguyen V, Zhu R, Jenkins K, Yang R. Self-assembly of diphenylalanine peptide with controlled polarization for power generation. Nat Commun. 2016;7:13566.
45. Ahn AC, Grodzinsky AJ. Relevance of collagen piezoelectricity to "Wolff's Law": a critical review. Med Eng Phys. 2009;31(7):733-41.
46. Kol N, Adler-Abramovich L, Barlam D, Shneck RZ, Gazit E, Rousso I. Self-assembled peptide nanotubes are uniquely rigid bioinspired supramolecular structures. Nano letters. 2005;5(7):1343-6.
47. Niu L, Chen X, Allen S, Tendler SJB. Using the Bending Beam Model to Estimate the Elasticity of Diphenylalanine Nanotubes. Langmuir. 2007;23(14):7443-6.
48. Azuri I, Adler-Abramovich L, Gazit E, Hod O, Kronik L. Why are diphenylalanine-based peptide nanostructures so rigid? Insights from first principles calculations. J Am Chem Soc. 2014;136(3):963-9.
49. Vasilev S, Zelenovskiy P, Vasileva D, Nuraeva A, Shur VY, Kholkin AL. Piezoelectric properties of diphenylalanine microtubes prepared from the solution. Journal of Physics and Chemistry of Solids. 2016;93:68-72.
50. Nguyen V, Jenkins K, Yang R. Epitaxial growth of vertically aligned piezoelectric diphenylalanine peptide microrods with uniform polarization. Nano Energy. 2015;17:323-9.
51. Heredia A, Bdikin I, Kopyl S, Mishina E, Semin S, Sigov A, et al. Temperature-driven phase transformation in self-assembled diphenylalanine peptide nanotubes. Journal of Physics D: Applied Physics. 2010;43(46):462001.
52. Zhang J, Wu X, Gan Z, Zhu X, Jin Y. Unidirectionally aligned diphenylalanine nanotube/microtube arrays with excellent supercapacitive performance. Nano Research. 2014;7(6):929-37.
53. Sakurai M, Koley P, Aono M. A new approach to molecular self-assembly through formation of dipeptide-based unique architectures by artificial supersaturation. Chemical Communications. 2014;50(83):12556-9.
54. Scanlon S, Aggeli A. Self-assembling peptide nanotubes. Nano Today. 2008;3(3):22-30.
55. Reches M, Gazit E. Controlled patterning of aligned self-assembled peptide nanotubes. Nature nanotechnology. 2006;1(3):195-200.
56. Zhang Y, Liu Y, Wang ZL. Fundamental theory of piezotronics. Adv Mater. 2011;23(27):3004-13.

57. Jenkins K, Nguyen V, Zhu R, Yang R. Piezotronic Effect: An Emerging Mechanism for Sensing Applications. Sensors (Basel). 2015;15(9):22914-40.
58. Jenkins K, Yang R. Piezoelectric Nanomaterials for Energy Harvesting. Nanomaterials for Sustainable Energy: Springer; 2016. p. 193-213.
59. Wang ZL, Song J. Piezoelectric nanogenerators based on zinc oxide nanowire arrays. Science. 2006;312(5771):242-6.
60. Yang R, Qin Y, Li C, Zhu G, Wang ZL. Converting biomechanical energy into electricity by a muscle-movement-driven nanogenerator. Nano Letters. 2009;9(3):1201-5.
61. Yang R, Qin Y, Dai L, Wang ZL. Power generation with laterally packaged piezoelectric fine wires. Nat Nanotechnol. 2009;4(1):34-9.
62. Xu S, Qin Y, Xu C, Wei Y, Yang R, Wang ZL. Self-powered nanowire devices. Nat Nanotechnol. 2010;5(5):366-73.
63. van der Zande AM, Huang PY, Chenet DA, Berkelbach TC, You Y, Lee G-H, et al. Grains and grain boundaries in highly crystalline monolayer molybdenum disulphide. Nature materials. 2013;12(6):554-61.
64. Zhou Y, Liu W, Huang X, Zhang A, Zhang Y, Wang ZL. Theoretical study on two-dimensional MoS2 piezoelectric nanogenerators. Nano Research.1-8.
65. Zhou J, Gu Y, Fei P, Mai W, Gao Y, Yang R, et al. Flexible Piezotronic Strain Sensor. Nano Letters. 2008;8(9):3035-40.
66. Yu R, Dong L, Pan C, Niu S, Liu H, Liu W, et al. Piezotronic effect on the transport properties of GaN nanobelts for active flexible electronics. Adv Mater. 2012;24(26):3532-7.
67. Zhang W, Zhu R, Nguyen V, Yang R. Highly sensitive and flexible strain sensors based on vertical zinc oxide nanowire arrays. Sensors and Actuators A: Physical. 2014;205:164-9.
68. Yang Y, Qi JJ, Gu YS, Wang XQ, Zhang Y. Piezotronic strain sensor based on single bridged ZnO wires. physica status solidi (RRL) - Rapid Research Letters. 2009;3(7-8):269-71.
69. Zhang Z, Liao Q, Zhang X, Zhang G, Li P, Lu S, et al. Highly efficient piezotronic strain sensors with symmetrical Schottky contacts on the monopolar surface of ZnO nanobelts. Nanoscale. 2015;7(5):1796-801.
70. Wei A, Pan L, Huang W. Recent progress in the ZnO nanostructure-based sensors. Materials Science and Engineering: B. 2011;176(18):1409-21.
71. Liang T, Zha J-W, Wang D-r, Dang Z-M. Remarkable piezoresistance effect on the flexible strain sensor based on a single ultralong tellurium micrometre wire. Journal of Physics D: Applied Physics. 2014;47(50):505103.
72. Liao Q, Mohr M, Zhang X, Zhang Z, Zhang Y, Fecht HJ. Carbon fiber-ZnO nanowire hybrid structures for flexible and adaptable strain sensors. Nanoscale. 2013;5(24):12350-5.
73. Wu JM, Chen K-H, Zhang Y, Wang ZL. A self-powered piezotronic strain sensor based on single ZnSnO3 microbelts. RSC Advances. 2013;3(47):25184.
74. Wu JM, Chen CY, Zhang Y, Chen KH, Yang Y, Hu YF, et al. Ultrahigh Sensitive Piezotronic Strain Sensors Based on a ZnSnO3 Nanowire/Microwire. Acs Nano. 2012;6(5):4369-74.
75. Dal Corso A, Posternak M, Resta R, Baldereschi A. Ab initio study of piezoelectricity and spontaneous polarization in ZnO. Phys Rev B Condens Matter. 1994;50(15):10715-21.
76. Bernardini F, Fiorentini V, Vanderbilt D. Spontaneous polarization and piezoelectric constants of III-V nitrides. Physical Review B. 1997;56(16):R10024.
77. Zhu R, Zhang WG, Li C, Yang RS. Uniform Zinc Oxide Nanowire Arrays Grown on Nonepitaxial Surface with General Orientation Control. Nano Letters. 2013;13(11):5171-6.

78. Wen X, Wu W, Ding Y, Wang ZL. Piezotronic effect in flexible thin-film based devices. Adv Mater. 2013;25(24):3371-9.
79. Zhao J, Zhang GY, Shi DX. Review of graphene-based strain sensors. Chinese Phys B. 2013;22(5).
80. Window AL. Strain Gauge Technology: Springer Netherlands; 1992.
81. Grow RJ, Wang Q, Cao J, Wang DW, Dai HJ. Piezoresistance of carbon nanotubes on deformable thin-film membranes. Appl Phys Lett. 2005;86(9).
82. Wu WZ, Wen XN, Wang ZL. Taxel-Addressable Matrix of Vertical-Nanowire Piezotronic Transistors for Active and Adaptive Tactile Imaging. Science. 2013;340(6135):952-7.
83. Zhou YS, Hinchet R, Yang Y, Ardila G, Songmuang R, Zhang F, et al. Nano-Newton transverse force sensor using a vertical GaN nanowire based on the piezotronic effect. Adv Mater. 2013;25(6):883-8.
84. Pan C, Dong L, Zhu G, Niu S, Yu R, Yang Q, et al. High-resolution electroluminescent imaging of pressure distribution using a piezoelectric nanowire LED array. Nature Photonics. 2013;7(9):752-8.
85. Zhou J, Fei P, Gao YF, Gu YD, Liu J, Bao G, et al. Mechanical-electrical triggers and sensors using piezoelectric micowires/nanowires. Nano Letters. 2008;8(9):2725-30.
86. Johansson RS, Vallbo AB. Detection of tactile stimuli. Thresholds of afferent units related to psychophysical thresholds in the human hand. J Physiol. 1979;297(0):405-22.
87. Mascaro S, Asada HH. Photoplethysmograph fingernail sensors for measuring finger forces without haptic obstruction. Robotics and Automation, IEEE Transactions on. 2001;17(5):698-708.
88. Zhao Y, Deng P, Nie Y, Wang P, Zhang Y, Xing L, et al. Biomolecule-adsorption-dependent piezoelectric output of ZnO nanowire nanogenerator and its application as self-powered active biosensor. Biosens Bioelectron. 2014;57:269-75.
89. Razeghi M, Lee KY, Sudharsanan R, Choi D, Choi J-Y, Brown GJ, et al. Flexible nanogenerators for self-powered touch and light sensor applications. 2011;7945:794526.
90. Salomon S, Eymery J, Pauliac-Vaujour E. GaN wire-based Langmuir-Blodgett films for self-powered flexible strain sensors. Nanotechnology. 2014;25(37):375502.
91. Wang ZL. Piezotronics for smart CMOS and nanogenerators for self-powered sensors. Procedia Engineering. 2011;25:4-7.
92. Wang ZL. Self-powered nanosensors and nanosystems. Adv Mater. 2012;24(2):280-5.
93. Xue XY, Nie YX, He B, Xing LL, Zhang Y, Wang ZL. Surface free-carrier screening effect on the output of a ZnO nanowire nanogenerator and its potential as a self-powered active gas sensor. Nanotechnology. 2013;24(22).
94. Zhu G, Yang R, Wang S, Wang ZL. Flexible high-output nanogenerator based on lateral ZnO nanowire array. Nano Lett. 2010;10(8):3151-5.
95. Wang PL, Fu YM, Yu BW, Zhao YY, Xing LL, Xue XY. Realizing room-temperature self-powered ethanol sensing of ZnO nanowire arrays by combining their piezoelectric, photoelectric and gas sensing characteristics. J Mater Chem A. 2015;3(7):3529-35.
96. Pradel KC, Wu W, Ding Y, Wang ZL. Solution-derived ZnO homojunction nanowire films on wearable substrates for energy conversion and self-powered gesture recognition. Nano Lett. 2014;14(12):6897-905.

97. Romano G, Mantini G, Di Carlo A, D'Amico A, Falconi C, Wang ZL. Piezoelectric potential in vertically aligned nanowires for high output nanogenerators. Nanotechnology. 2011;22(46):465401.
98. Lee E, Park J, Yim M, Kim Y, Yoon G. Characteristics of piezoelectric ZnO/AlN−stacked flexible nanogenerators for energy harvesting applications. Appl Phys Lett. 2015;106(2):023901.
99. Pi Z, Zhang J, Wen C, Zhang Z-b, Wu D. Flexible piezoelectric nanogenerator made of poly (vinylidenefluoride-co-trifluoroethylene)(PVDF-TrFE) thin film. Nano Energy. 2014;7:33-41.
100. Huang X, Li L, Zhang Y. Modeling the open circuit output voltage of piezoelectric nanogenerator. Science China Technological Sciences. 2013;56(11):2622-9.
101. Schubert MA, Senz S, Alexe M, Hesse D, Gösele U. Finite element method calculations of ZnO nanowires for nanogenerators. Appl Phys Lett. 2008;92(12):122904.
102. Tao R, Hinchet R, Ardila G, Montès L, Mouis M, editors. FEM modeling of vertically integrated nanogenerators in compression and flexion modes. Ph D Research in Microelectronics and Electronics (PRIME), 2014 10th Conference on; 2014: IEEE.
103. Wang ZL. Piezotronics and Piezo-Phototronics: Wiley Online Library; 2012.
104. Comsol Multiphysics, Version 5.0.
105. Bdikin I, Bystrov V, Kopyl S, Lopes RPG, Delgadillo I, Gracio J, et al. Evidence of ferroelectricity and phase transition in pressed diphenylalanine peptide nanotubes. Appl Phys Lett. 2012;100(4):043702.
106. Qiu Y, Zhang H, Hu L, Yang D, Wang L, Wang B, et al. Flexible piezoelectric nanogenerators based on ZnO nanorods grown on common paper substrates. Nanoscale. 2012;4(20):6568-73.
107. Kim SK, Bhatia R, Kim T-H, Seol D, Kim JH, Kim H, et al. Directional dependent piezoelectric effect in CVD grown monolayer MoS2 for flexible piezoelectric nanogenerators. Nano Energy. 2016;22:483-9.
108. Chang C, Tran VH, Wang J, Fuh Y-K, Lin L. Direct-write piezoelectric polymeric nanogenerator with high energy conversion efficiency. Nano letters. 2010;10(2):726-31.
109. Lee BY, Zhang J, Zueger C, Chung WJ, Yoo SY, Wang E, et al. Virus-based piezoelectric energy generation. Nat Nanotechnol. 2012;7(6):351-6.
110. Ziegler-Graham K, MacKenzie EJ, Ephraim PL, Travison TG, Brookmeyer R. Estimating the prevalence of limb loss in the United States: 2005 to 2050. Arch Phys Med Rehabil. 2008;89(3):422-9.
111. Tan DW, Schiefer MA, Keith MW, Anderson JR, Tyler J, Tyler DJ. A neural interface provides long-term stable natural touch perception. Sci Transl Med. 2014;6(257):257ra138.
112. Raspopovic S, Capogrosso M, Petrini FM, Bonizzato M, Rigosa J, Di Pino G, et al. Restoring natural sensory feedback in real-time bidirectional hand prostheses. Sci Transl Med. 2014;6(222):222ra19.
113. Hammock ML, Chortos A, Tee BC, Tok JB, Bao Z. 25th anniversary article: The evolution of electronic skin (e-skin): a brief history, design considerations, and recent progress. Adv Mater. 2013;25(42):5997-6038.
114. Antfolk C, D'Alonzo M, Controzzi M, Lundborg G, Rosen B, Sebelius F, et al. Artificial redirection of sensation from prosthetic fingers to the phantom hand map on transradial amputees: vibrotactile versus mechanotactile sensory feedback. IEEE Trans Neural Syst Rehabil Eng. 2013;21(1):112-20.

115. Cipriani C, D'Alonzo M, Carrozza MC. A miniature vibrotactile sensory substitution device for multifingered hand prosthetics. IEEE Trans Biomed Eng. 2012;59(2):400-8.
116. Shill JJ, Collins EG, Jr., Coyle E, Clark J. Tactile surface classification for limbed robots using a pressure sensitive robot skin. Bioinspir Biomim. 2015;10(1):016012.
117. D'Alonzo M, Dosen S, Cipriani C, Farina D. HyVE: hybrid vibro-electrotactile stimulation for sensory feedback and substitution in rehabilitation. IEEE Trans Neural Syst Rehabil Eng. 2014;22(2):290-301.
118. Francomano MT, Accoto D, Guglielmelli E. Artificial sense of slip—A review. IEEE Sensors Journal. 2013;13(7):2489-98.
119. Dahiya RS, Metta G, Valle M, Sandini G. Tactile Sensing—From Humans to Humanoids. IEEE Transactions on Robotics. 2010;26(1):1-20.
120. McGlone F, Reilly D. The cutaneous sensory system. Neuroscience & Biobehavioral Reviews. 2010;34(2):148-59.
121. Bear MF, Connors BW, Paradiso MA. Neuroscience: Lippincott Williams & Wilkins; 2007.
122. Johansson R, Vallbo Å, Westling G. Thresholds of mechanosensitive afferents in the human hand as measured with von Frey hairs. Brain research. 1980;184(2):343-51.
123. Skedung L, Arvidsson M, Chung JY, Stafford CM, Berglund B, Rutland MW. Feeling small: exploring the tactile perception limits. Scientific reports. 2013;3:2617.
124. Lucarotti C, Oddo CM, Vitiello N, Carrozza MC. Synthetic and bio-artificial tactile sensing: a review. Sensors (Basel). 2013;13(2):1435-66.
125. Cheng MY, Huang XH, Ma CW, Yang YJ. A flexible capacitive tactile sensing array with floating electrodes. Journal of Micromechanics and Microengineering. 2009;19(11):115001.
126. Ponce Wong RD, Posner JD, Santos VJ. Flexible microfluidic normal force sensor skin for tactile feedback. Sensors and Actuators A: Physical. 2012;179:62-9.
127. Hyung-Kew L, Jaehoon C, Sun-Il C, Euisik Y. Normal and Shear Force Measurement Using a Flexible Polymer Tactile Sensor With Embedded Multiple Capacitors. Journal of Microelectromechanical Systems. 2008;17(4):934-42.
128. Hu Y, Katragadda RB, Tu H, Zheng Q, Li Y, Xu Y. Bioinspired 3-D Tactile Sensor for Minimally Invasive Surgery. Journal of Microelectromechanical Systems. 2010;19(6):1400-8.
129. Chuang C-H, Dong W-B, Lo W-B, editors. Flexible piezoelectric tactile sensor with structural electrodes array for shape recognition system. Sensing Technology, 2008 ICST 2008 3rd International Conference on; 2008: IEEE.
130. Muhammad H, Hunt N, Shelton R, Grover L, Ward M, Oddo C, et al., editors. Incorporation of novel MEMS tactile sensors into tissue engineered skin. Bioinformatics and Biomedical Engineering (iCBBE), 2010 4th International Conference on; 2010: IEEE.
131. Cheneler D, Ward MCL, Anthony CJ. Bio-hybrid tactile sensor for the study of the role of mechanoreceptors in human tactile perception. Microelectronic Engineering. 2012;97:297-300.
132. Merzenich MM, Nelson RJ, Stryker MP, Cynader MS, Schoppmann A, Zook JM. Somatosensory cortical map changes following digit amputation in adult monkeys. Journal of comparative Neurology. 1984;224(4):591-605.
133. Mercier C, Reilly KT, Vargas CD, Aballea A, Sirigu A. Mapping phantom movement representations in the motor cortex of amputees. Brain. 2006;129(8):2202-10.
134. Reilly KT, Mercier C, Schieber MH, Sirigu A. Persistent hand motor commands in the amputees' brain. Brain. 2006;129(8):2211-23.

135. Rossini PM, Micera S, Benvenuto A, Carpaneto J, Cavallo G, Citi L, et al. Double nerve intraneural interface implant on a human amputee for robotic hand control. Clin Neurophysiol. 2010;121(5):777-83.
136. Hunter JP, Katz J, Davis KD. The effect of tactile and visual sensory inputs on phantom limb awareness. Brain. 2003;126(3):579-89.
137. Di Pino G, Guglielmelli E, Rossini PM. Neuroplasticity in amputees: main implications on bidirectional interfacing of cybernetic hand prostheses. Progress in neurobiology. 2009;88(2):114-26.
138. Engeberg ED, Meek SG, editors. Adaptive object slip prevention for prosthetic hands through proportional-derivative shear force feedback. Intelligent Robots and Systems, 2008 IROS 2008 IEEE/RSJ International Conference on; 2008: IEEE.
139. Engeberg ED, Meek SG, editors. Adaptive sliding mode control of grasped object slip for prosthetic hands. Intelligent Robots and Systems (IROS), 2011 IEEE/RSJ International Conference on; 2011: IEEE.
140. Fernandez R, Payo I, Vazquez AS, Becedas J. Micro-vibration-based slip detection in tactile force sensors. Sensors. 2014;14(1):709-30.
141. Liang X, Boppart SA. Biomechanical properties of in vivo human skin from dynamic optical coherence elastography. IEEE Transactions on Biomedical Engineering. 2010;57(4):953-9.
142. Pawlaczyk M, Lelonkiewicz M, Wieczorowski M. Age-dependent biomechanical properties of the skin. Advances in Dermatology and Allergology/Postępy Dermatologii i Alergologii. 2013;30(5):302.
143. Baruah S, Dutta J. Hydrothermal growth of ZnO nanostructures. Sci Technol Adv Mater. 2009;10(1):013001.
144. Jenkins K, Yang R. Mechanical transfer of ZnO nanowires for a flexible and conformal piezotronic strain sensor. Semiconductor Science and Technology. 2017;32(7):074004.
145. Plass KE, Filler MA, Spurgeon JM, Kayes BM, Maldonado S, Brunschwig BS, et al. Flexible Polymer-Embedded Si Wire Arrays. Advanced Materials. 2009;21(3):325-8.
146. Standing AJ, Assali S, Haverkort JE, Bakkers EP. High yield transfer of ordered nanowire arrays into transparent flexible polymer films. Nanotechnology. 2012;23(49):495305.
147. Chang YK, Hong FC. The fabrication of ZnO nanowire field-effect transistors by roll-transfer printing. Nanotechnology. 2009;20(19):195302.
148. Weisse JM, Lee CH, Kim DR, Zheng X. Fabrication of flexible and vertical silicon nanowire electronics. Nano Lett. 2012;12(6):3339-43.
149. Coppa BJ, Davis RF, Nemanich RJ. Gold Schottky contacts on oxygen plasma-treated, n-type ZnO(000$\bar{1}$). Appl Phys Lett. 2003;82(3):400-2.
150. Baek JY, Kwon GH, Kim JY, Cho JH, Lee SH, Sun K, et al. Stable Deposition and Patterning of Metal Layers on the PDMS Substrate and Characterization for the Development of the Flexible and Implantable Micro Electrode. Solid State Phenomena. 2007;124-126:165-8.
151. Moradi M, Sivoththaman S. Strain Transfer Analysis of Surface-Bonded MEMS Strain Sensors. IEEE Sensors Journal. 2013;13(2):637-43.
152. Huang MH, Wu Y, Feick H, Tran N, Weber E, Yang P. Catalytic growth of zinc oxide nanowires by vapor transport. Advanced Materials. 2001;13(2):113-6.
153. Burshtein G, Lumelsky V, Lifshitz Y. The role of reactive gases in ZnO nanowires growth via the carbothermal reaction. The Journal of Physical Chemistry C. 2016;120(28):15424-35.

Appendix

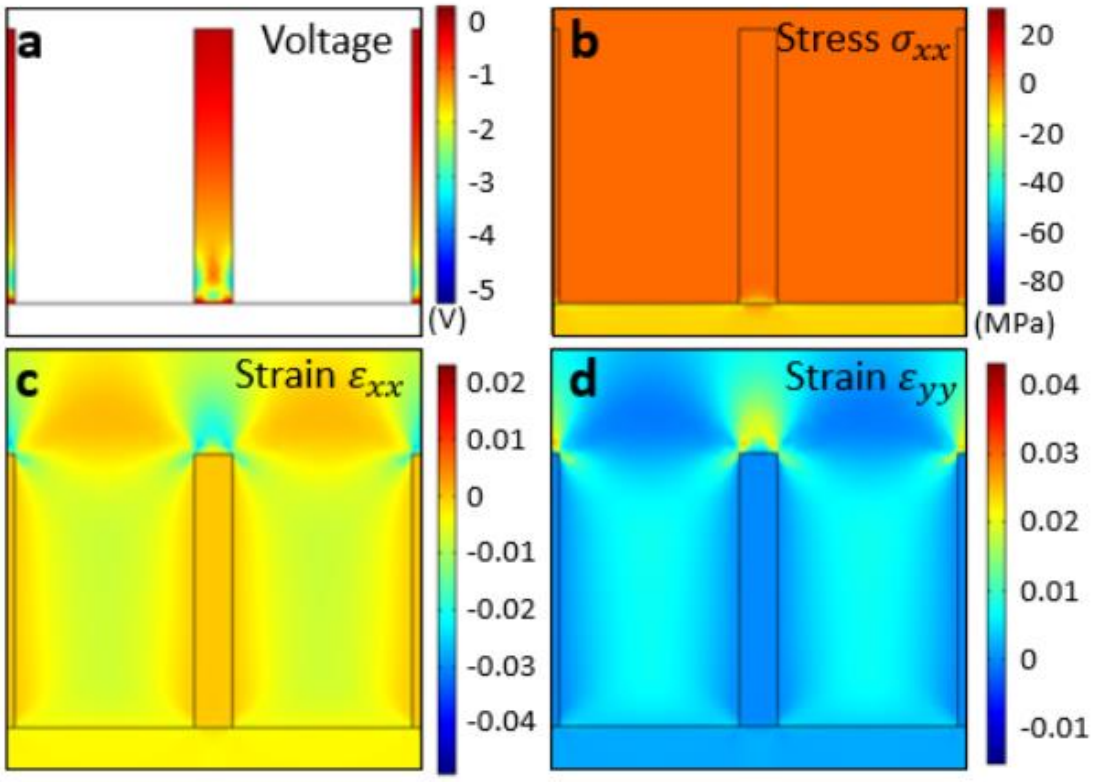

Figure A1. Detailed view of stress, strain, and piezopotential in a single FF peptide microrod at location x = 11 mm (Region I). (a) Piezoelectric potential. (b) Stress tensor, xx component. (c) Strain tensor, xx component. (d) Strain tensor, yy component.

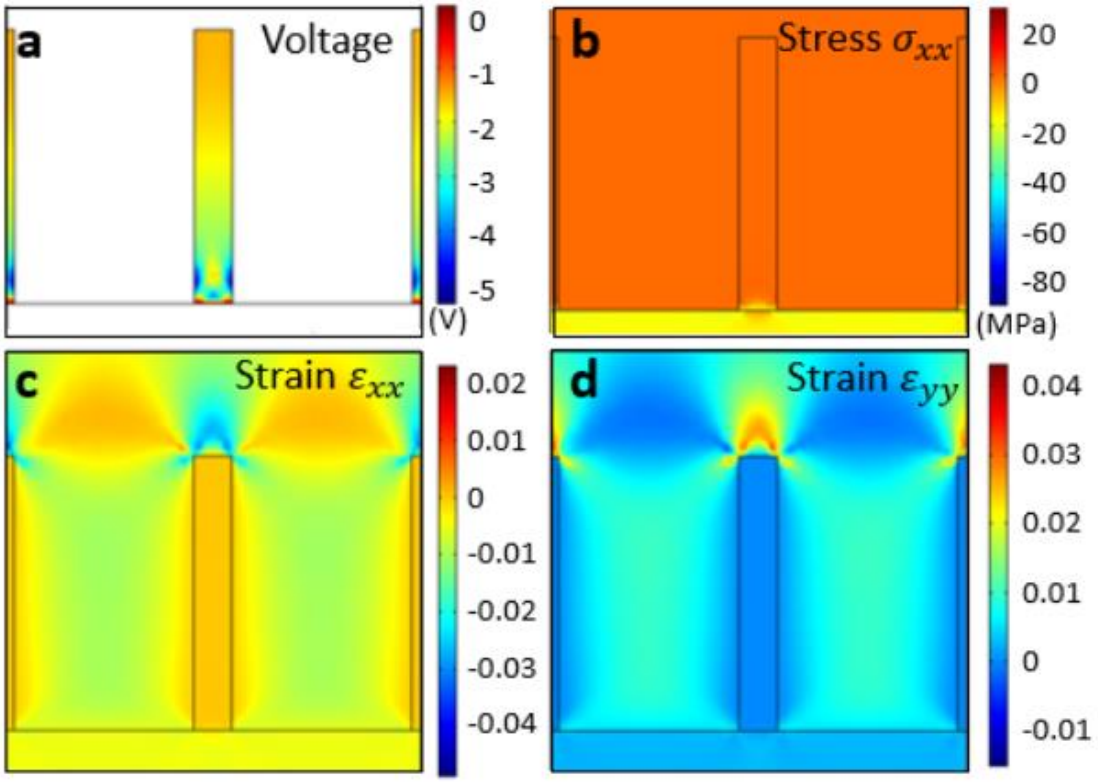

Figure A2. Detailed view of stress, strain, and piezopotential in a single FF peptide microrod at location x = 15 mm (Region II). (a) Piezoelectric potential. (b) Stress tensor, xx component. (c) Strain tensor, xx component. (d) Strain tensor, yy component.

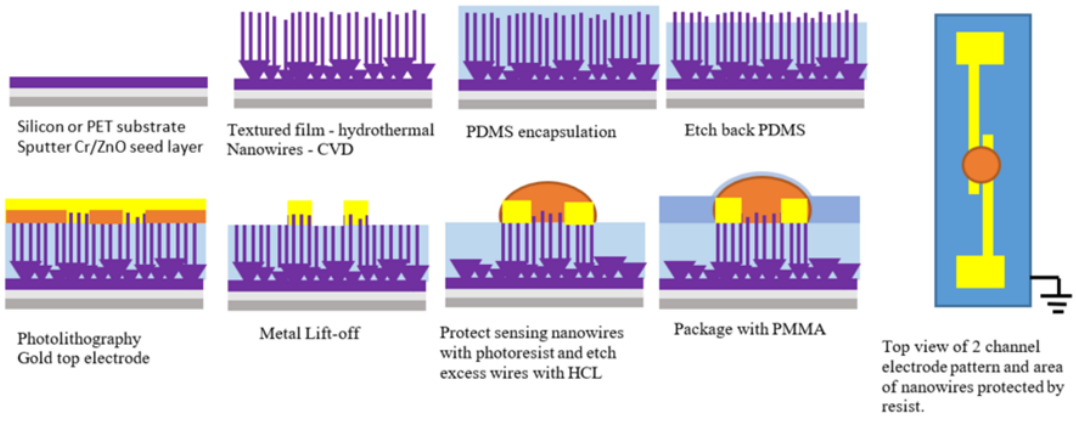

Figure A3. Microfabrication steps for piezotronic contact force sensor.

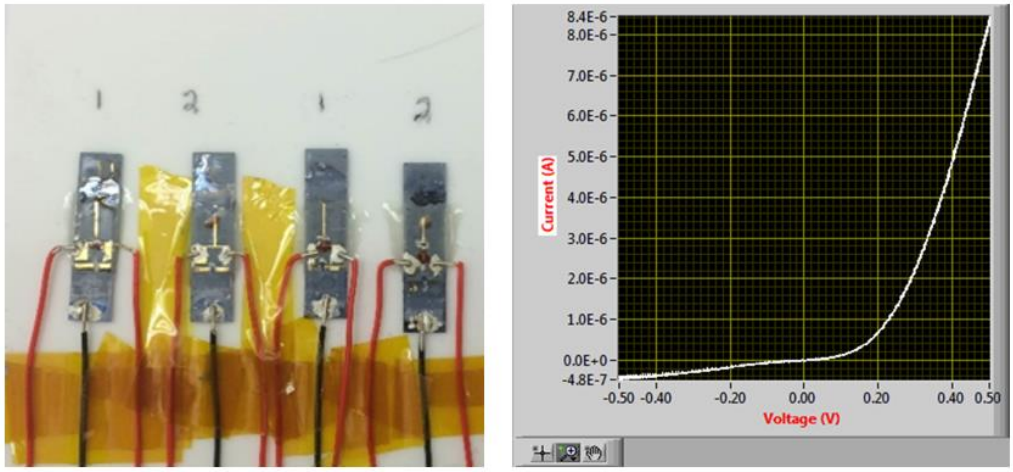

Figure A4. Testing fabricated piezotronic contact force sensor. Completed piezotronic contact force sensors (left), and initial characterization data showing I-V behavior of the Schottky contact (right).